Deformation of steel ingots by punch pressing during their solidification. Numerical modelling and experimental validation of induced hot cracking and macrosegregation phenomena

Takao Koshikawa

THÈSE DE DOCTORAT

de l'Université de recherche Paris Sciences et Lettres
PSL Research University

Préparée à MINES ParisTech

Deformation of steel ingots by punch pressing during their solidification. Numerical modelling and experimental validation of induced hot cracking and macrosegregation phenomena

Ecole doctorale n°364

Spécialité Science et Génie des Matériaux

COMPOSITION DU JURY :

Pr. Steven LE CORRE
Université de Nantes, France
Rapporteur

Pr. Menghuai WU
Université de Leoben, Autriche
Rapporteur

Dr. Toshiyuki KAJITANI
Nippon Steel & Sumitomo Metal Corporation, Japon
Examinateur

Pr. Wilfried KURZ
Ecole Polytechnique Fédérale de Lausanne, Suisse
Examinateur

Dr. Benjamin RIVAUX
ArcelorMittal Maizières, France
Examinateur

Pr. Michel BELLET
MINES ParisTech, France
Directeur de thèse

Dr. Charles-André GANDIN
CNRS, France
Directeur de thèse

Soutenue par Takao KOSHIKAWA
le 20.09.2016

MINES ParisTech | PSL RESEARCH UNIVERSITY PARIS

Acknowledgements

First of all, I would like to thank my directors, Pr. Michel Bellet and Dr. Charles-André Gandin for their acceptance that I came to their labs, great support, kind guidance, many advices and encouragements. My two years stay in CEMEF and three years study through visio meeting from Japan enriched my knowledge but also gave me challenge spirits to something difficulties I have faced. I never forget all.

I am sincerely grateful to the members of the jury, Pr Steven Le Corre, Pr. Menghuai Wu, Pr. Wilfried Kurz, Dr. Toshiyuki Kajitani and Dr. Benjamin Rivaux for their great work on my thesis committee.

I would like to thank Olivier Jaouen and Dr Frédéric Costes from TRANSVALOR (Mougins, France), for their kind help and interesting discussion about thermomechanical modeling using software THERCAST®. Without their help, my thesis would not be completed.

I would like to thank all the CEMEF staff. Special thanks are sent to Patrick Coels, Marie-Françoise Guenegan, Carole Torrin and Suzanne Jacomet for their great help and to the directors Yvan Chastel and Elisabeth Massoni.

I would like to thank all the members of the TMP and SP2 groups and the colleagues: Gildas, Tommy, Alexis, Ala, Ali, Shijia, Thi-Thuy-My and others for their kindness and interesting talks with me. Many thanks to Siham and Ana-Laura for their friendship and having lunch together lots of time. I would like to thank to Abbass for his friendship and cheerful talk at our bureau.

This work is supported by Nippon Steel & Sumitomo Metal Corporation in a collaborative project with ArcelorMittal. I would like to thank the partners of the project and everyone in NSSMC who gave me this great opportunity to go abroad and work on the project.

At last, I would like to thank my family, especially my wife for her great support. Thank you for your coming to France and challenging difficulties with our small daughter.

Contents

List of principal symbols

Latin alphabet

A	rheological coefficient depending on the solid volume fraction	-
B	rheological coefficient depending on the solid volume fraction	-
Cst_i	constant value for element i	J mol^{-1}
Cst1	constant value	J mol^{-1}
Cst2	constant value	J mol^{-1}
c_P	specific heat per unit mass depending on temperature	J kg^{-1} K^{-1}
$D_{l,i}$	diffusion coefficient in the liquid phase for each solute i	m^2 s^{-1}
d	thickness of solidified shell	mm
dev	deviatoric part of a tensor	-
F_{HT}	criterion function	-
$F_{\mathrm{HT}}^{\mathrm{WYSO}}$	strain-based criterion	-
$F_{\mathrm{HT,e}}^{\mathrm{WYSO}}$	maximum value of the quantities $F_{\mathrm{HT,e}}^{\mathrm{WYSO,i}}$	-
$F_{\mathrm{HT,e}}^{\mathrm{WYSO,i}}$	strain-based criterion in each finite element e at a time increment, i	-
$\mathbf{g}$	gravity vector	m s^{-2}
g_l	volume fraction of liquid phase	-
g_s	volume fraction of solid phase	-
g_s^{crit}	coherency solid volume fraction at which the compressibility of the solid phase is extremely high ($B \to \infty$)	-
H	strain hardening coefficient depending on temperature	Pa
h	average specific enthalpy per unit mass depending on temperature	J kg^{-1}

$\langle h \rangle$	average enthalpy of the solid-liquid mixture	J kg^{-1}
I	unit tensor (identity tensor)	-
K	viscoplastic consistency depending on temperature	Pa s^m
k_A	parameter of rheological function A	-
k_B	parameter of rheological function B	-
k_i	partition coefficient for each solute i	-
L	latent heat	J kg^{-1}
l	liquid phase	-
m	strain rate sensitivity depending on temperature	-
m^*	parameter of strain limit	-
m_i	liquidus slope for each solute i	K mass$\%^{-1}$
N_0	constant mole	mol
${}^{(k-1)}N^{p_j}$	initial phase fraction for phase p_j at calculation step k	-
${}^{k}N^{p_j}$	phase fraction for phase p_j at calculation step k	-
n	strain sensitivity depending on temperature	-
n^*	parameter of strain limit	-
n^p	number of phases	-
n^s	number of chemical elements	-
P_0	constant pressure	Pa
p	pressure	Pa
p_j	phases with $p_j = \{s_1, s_2, ..., l\}$ and $j = [1, n^p]$	-
p_l	liquid phase pressure	Pa
$\langle p^l \rangle^l$	intrinsic average liquid phase pressure	Pa
s	solid phase	-
s	deviatoric stress tensor	Pa
$\langle \mathbf{s}^l \rangle$	average deviatoric stress tensor in the liquid phase	Pa
T	temperature	K
${}^{(k-1)}T$	initial temperature at calculation step k	K
${}^{k}T$	temperature defined, ${}^{k}T = {}^{(k-1)}T - \Delta T$	K
T_0	initial temperature	K
T_{END}	arbitrary temperature for calculation stop	K
T_L	Liquidus temperature	K
tr	trace of a tensor	-

T_S	solidus temperature	K
T_{surf}	surface temperature	K
T_{ZD}	zero ductility temperature	K
${}^{k}\overline{u}^{p_j}_{i\neq C}$	average u-fractions of substitutional elements defined by ${}^{k}\overline{u}^{p_j}_{i\neq C} = {}^{k}\overline{x}^{p_j}_{i\neq C} / \left(1 - {}^{k}\overline{x}^{p_j}_{C}\right)$, where C indicates carbon as interstitial element	-
$\mathbf{v}_l$	liquid velocity vector	m s^{-1}
$\left\langle \mathbf{v}^l \right\rangle^l$	intrinsic average liquid phase velocity	m s^{-1}
$\mathbf{v}_s$	solid velocity vector	m s^{-1}
$\left\langle \mathbf{v}^s \right\rangle^s$	intrinsic average solid phase velocity	m s^{-1}
$w_{l,i}$	intrinsic average concentration in the liquid phase for each solute i	mass%
$\langle w_i \rangle$	average solute mass concentration of the solid-liquid mixture for each solute i	mass%
${}^{(k-1)}x_i^{p_j}$	initial composition for phase p_j and element i, i = [1, n^s], at calculation step k	mass%
${}^{k}x_i^{p_j}$	composition for phase p_j and element i, i = [1, n^s], at calculation step k	mass%
x_{i0}	initial composition	mass%
${}^{(k-1)}\overline{x}_i^{p_j}$	initial average composition for phase p_j and element i, i = [1, n^s], at calculation step k	mass%
${}^{k}\overline{x}_i^{p_j}$	average composition for phase p_j and element i, i = [1, n^s], at calculation step k	mass%

Greek alphabet

$\boldsymbol{\gamma}$	acceleration vector	m s^{-2}
ΔT	small temperature	K
ΔT_{BTR}	extent of the brittle temperature range (BTR)	K
ε_{BTR}	local cumulated strain for a REV in the mushy zone during its cooling within a range of solid fraction	-
ε_c	critical strain at which cracks form	-
$\bar{\varepsilon}$	cumulated plastic strain	-
$\hat{\varepsilon}_c$	strain limit	-
$\dot{\varepsilon}$	strain rate	s^{-1}
$\dot{\boldsymbol{\varepsilon}}^{el}$	elastic strain rate tensor	s^{-1}
$\dot{\boldsymbol{\varepsilon}}^{th}$	thermal strain rate tensor	s^{-1}
$\dot{\boldsymbol{\varepsilon}}^{vp}$	viscoplastic part of the strain rate tensor $\dot{\boldsymbol{\varepsilon}} = (\nabla \mathbf{v} + \nabla^T \mathbf{v})/2$	s^{-1}
$\dot{\boldsymbol{\varepsilon}}(\mathbf{v}_l)$	symmetric part of the liquid velocity gradient $\nabla \mathbf{v}_l$	s^{-1}
$\dot{\boldsymbol{\varepsilon}}(\mathbf{v}_s)$	symmetric part of the solid velocity gradient $\nabla \mathbf{v}_s$	s^{-1}
$\dot{\bar{\varepsilon}}$	generalized strain rate	s^{-1}
$\dot{\hat{\varepsilon}}$	strain rate perpendicular to temperature gradient direction	s^{-1}
$\dot{\hat{\varepsilon}}_e^i$	strain rate perpendicular to temperature gradient direction in each finite element e at a time increment i	s^{-1}
$\left\langle \dot{\bar{\varepsilon}} \right\rangle^s$	equivalent strain rate	s^{-1}
η	poor ductility length	mm
κ	Permeability of the porous medium constituted by the solid phase	m^2
λ	thermal conductivity depending on temperature	W m^{-1} K^{-1}
λ_2	secondary dendrite arm spacing	m
$\langle \lambda \rangle$	average thermal conductivity of the solid-liquid mixture	W m^{-1} K^{-1}
${}^k\mu_i^{p_j}\left({}^k x_i^{p_j}\right)$	chemical potential for phase p_j and element i with composition ${}^k x_i^{p_j}$	J mol^{-1}

$\overline{\mu_i^{k}}^{p_j}\left(\overline{x_i^{k}}^{p_j}\right)$	average chemical potential for phase p_j and element i with average composition $\overline{x_i^{k}}^{p_j}$	J mol^{-1}
μ_l	dynamic viscosity of the liquid phase	Pa s
ϕ	parameter of strain limit	-
ρ	average density depending on temperature	kg m^{-3}
ρ_L	density at the liquidus temperature	kg m^{-3}
ρ_S	density at the solidus temperature	kg m^{-3}
$\rho_s(T)$	density of solid phase depending on temperature	kg m^{-3}
$\langle\rho\rangle$	average density of the solid-liquid mixture	kg m^{-3}
σ_{I}	first principal stress	Pa
$\overline{\sigma}$	equivalent von Mises stress	Pa
$\langle\boldsymbol{\sigma}\rangle$	average stress tensor	Pa
$\boldsymbol{\Sigma}^s$	effective macroscopic stress tensor for the solid phase in the mushy state	Pa
$\sum_{j=i\_start}^{i} \dot{\hat{\varepsilon}}_e^{j} \Delta t^{j}$	cumulated strain in each finite element e at a time increment i, i_start is the time increment at which element e enters the BTR, Δt^{j} is the time step at time increment j	-
φ	parameter of strain limit	-
∇	gradient	-
$\lVert\nabla T\rVert_\eta$	local temperature gradient	K mm^{-1}
$\nabla\cdot$	divergence	-
$\times$	vector product	-

Chapter I Introduction

1. Process presentation

In general, the continuous casting (CC) process is widely used in steel industries for solidifying molten steel (95.6 % of world production in 2015 [World Steel Association]). The schematic of the CC machine is shown in Figure 1. The molten steel is charged in the ladle and it is poured into the mould through the tundish. It is first cooled in the mould (primary cooling). Spray cooling is then applied in the roller aprons; in other words, segments. This is called secondary cooling. Thanks to cooling, molten steel is solidified at the exit of the machine. The solidified steel is cut by the torch cutter at required length for later processing. The typical slab size is 0.25 m thick, 2 m width and 10 m long typically for automotive industry. For machine length and machine height around 40 m and 10 m, respectively, this figure corresponding to the radius of bending zone. Looking at the shape of slab in the CC, the bending shape is found first from the mould and the straight shape is seen close to the exit of the CC. It indicates that the bending slab is straightened at the bottom of the bending zone, called unbending.

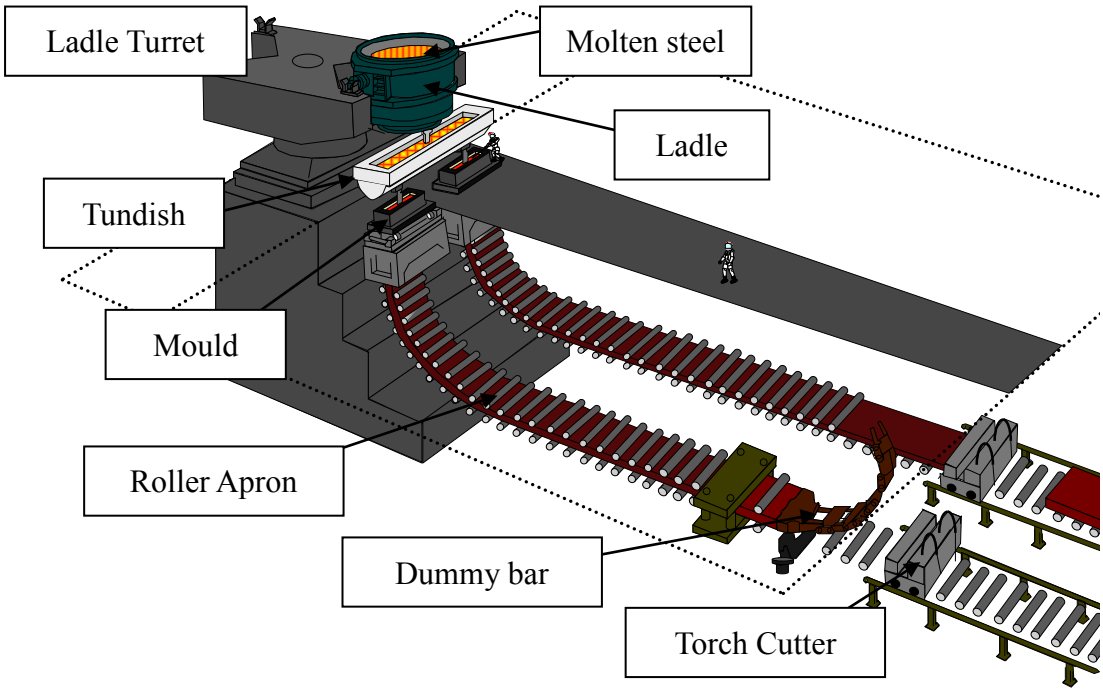

Figure 1 *Schematic of CC process*

An example of recent standards regarding machine specification can be found in the literature [Yamaguchi 2012]. The advantages of the CC process are productivity, yield, energy, labor efficiency and quality assurance [Okumura 1994].

2. Typical defects in CC

In the CC process, two types of defects appear: surface defects and internal defects.

< Surface defects >

- Surface cracks due to the deformation of solidified skin in the mould or the deformation of solidified shell in the bending and unbending zone. These could be removed after the CC process by means of scarfing process up to a certain extent and although this affects the yield and cost.
- Inclusion problems due to slag or mould powder which are entrapped in the solidified skin in the mould. These defects are reduced thanks to optimization of liquid melt flow in the mould with electromagnetic tools. They could be removed as well as surface cracks.

< Internal defects >

- Hot tearing due to the deformation of solidified skin in the mould or the deformation of the solidified shell in the bending and unbending zone. Such cracks cannot be removed since they are located inside the slab.
- Macrosegregation due to the deformation of solidified shell in the segments close to the end of solidification. These heterogeneities in the chemical concentrations of alloy elements cannot be removed as well.

Two critical internal defects are hot tearing (in other words, internal crack) and macro segregation or axial segregation taking place during the secondary cooling process. Hot tearing leads to defect on a steel coil for automotive industry or makes crucial trouble during hot rolling before the coil is obtained due to fissure of the steel sheet. Macrosegregation leads to non uniform mechanical properties of the product and so-called high quality products for line pipe or special tanker components require constant properties, which requires minimum macro segregation.

3. Presentation of hot tearing and macrosegregation defects

3.1 Short presentation of defects in the CC process

The phenomena are understood as follows: during secondary cooling process, molten steel heat is removed from the surface of the solidified shell. Regarding microstructure, dendritic crystals grow toward liquid core from the solidified shell along the temperature gradient. It means the dendritic grains are constrained to the direction perpendicular to the slab surface. Tensile deformation along the casting direction perpendicular to which the dendrites are aligned generates due to bulging, bending, unbending and misalignment between rollers (see Figure 2 and Figure 3). The tensile deformation makes hot tearing [Lankford 1972, Brimacombe 1977] in between dendrites deep in the mushy zone; typically over 0.9 fraction of solid phase. Since hot tearing takes place in the mushy zone, it is easily imagined that the solidification path based on microsegregation phenomena has an important role.

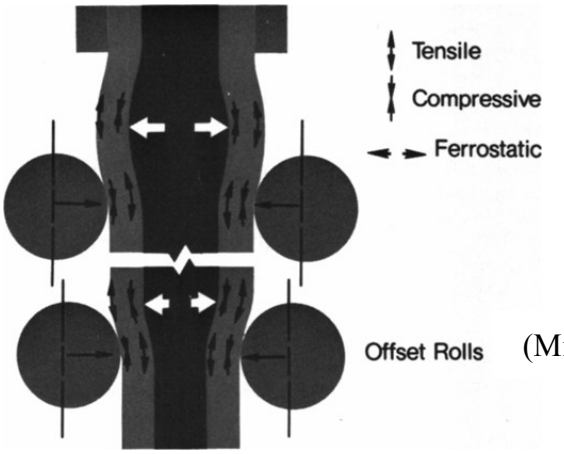

Figure 2 *Schematic of bulging and misalignment [Lankford 1972] and consequences in terms of tensile or compressive stresses.*

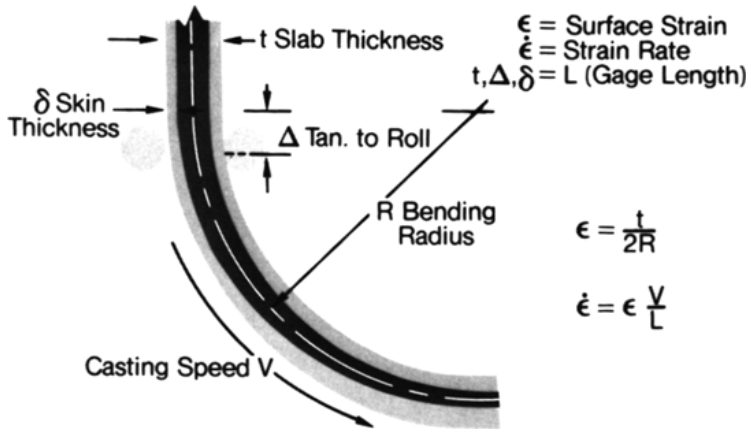

Figure 3 *Schematic of bending process and simple estimation of strain and strain rate [Lankford 1972].*

Close to the solidification end, macrosegregation generates due to enriched melt flow because of the complex combination among solidified shell deformation, shrinkage, induced fluid flow and solute transport [Miyazawa 1981], [Kajitani 2001], [Fachinotti 2006] and [Mayer 2010]. This defect is also connected with solidification path because it occurs in mushy zone, but in the specific context of CC process, solidified shell deformation and shrinkage could have an important role for the formation of macrosegregation. Concerning solidified shell deformation, it could be sure that bulging takes place in between rolls close to the end of solidification because of ferrostatic pressure depending on machine height. It then makes deformation of mushy zone in which the solid phase is deformed and the liquid phase is circulated due to solid phase movement. Because of the flow of the liquid with enriched solutes, composition field becomes varied, leading to macrosegregation. Second, shrinkage makes also liquid flow in mushy zone, resulting in variation of composition, that is to say, macrosegregation. In the CC process, it is quite popular that soft reduction is applied to solidifying slab close to the end of the melting pool. It means that slab thickness is gradually reduced due to decreasing roll gaps on a certain distance. The mechanical thickness reduction of the slab can compensate solidification shrinkage, leading to less liquid circulation close to the end of solidification, and, as a consequence, less marked segregation.

3.2 Hot tearing phenomena

3.2.1 Solidification stages

Solidification is the transformation from liquid phase to solid phase. This transformation occurs continuously and a mixture of solid and liquid phases coexist in what is called the mushy zone. The range between the solidus and the liquidus temperatures is called solidification interval. For a columnar structure, this solidification interval is generally divided into three regions, schematized in Figure 4. In regions 1 and 2, the mushy zone can absorb external tensile stress because of the capacity of the solid and the liquid phases to move. Thus, the sensitivity to cracking is relatively low. In contrast, when the solidification reaches region 3, the sensitivity becomes higher. Indeed, in this region, liquid films are isolated and the permeability in the mush falls dramatically up to the completion of solidification. Cracks that form in these conditions are known as hot tears, they are generally intergranular.

3.2.2 Different modes of hot tearing

Uniaxial tensile tests results, using aluminum alloys in mushy zone carried out by Braccini [Braccini 2000] and Ludwig et al. [Ludwig 2004], show that solid fraction has an important role for the material behavior. The solidification interval is divided into three stages.

- ✓ $g_s < g^{cohe}$: There is no mechanical resistance because of no solid bridges (region 1 in Figure 4(a)).
- ✓ $g_s^{cohe} < g_s < g_s^{coal}$: The mechanical resistance appears and it results in the loss of ductility (region 2 in Figure 4(a)).
- ✓ $g_s^{coal} < g_s$: Both the ductility and the mechanical resistance rapidly increase (region 3 in *Figure 4*(a)).

Figure 5 illustrates schematics of the main phenomena occurring in the mushy zone at characteristic solid fractions, above mentioned, explaining the loss of ductility in a given Brittle Temperature Range of the solidification.

(a)

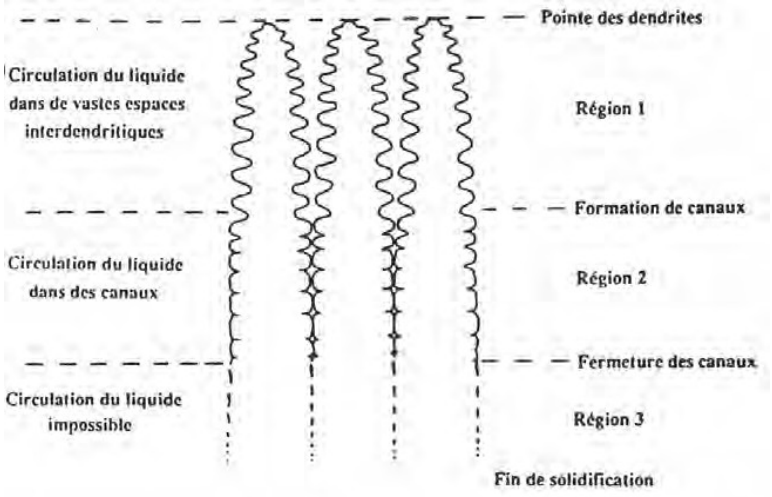

(b)

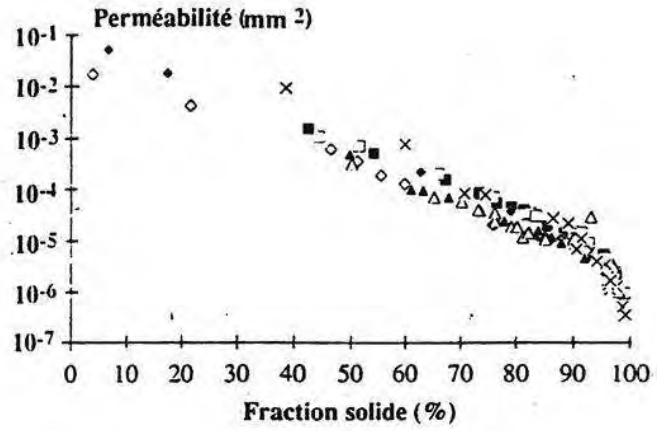

Figure 4 *On the top, schematic of the solidification interval of a columnar structure, on the bottom, relation between the permeability and the solid fraction [Wintz 1994].*

Braccini [Braccini 2000] have brought experimental evidences, in the case of aluminum alloys, of some specific cracking modes, depending on the solid fraction.

- ✓ In the case of low solid fraction: $g_s < g_s^{coal}$, hot tearing is due to propagation of rupture in the liquid films at the interface of the grains (Figure 6(a)). Then the surface tension of the liquid resists the propagation of the rupture. When this region is subject to excess stress, liquid films finally tear and peaks of liquid remain, as shown in Figure 6(c).
- ✓ In the case of the high solid fraction: $g_s^{coal} < g_s$, plastic deformation occurs in between solid bridges and leads to ductility (Figure 6(b)). The plastic deformation coexists with the previous rupture mechanism. However, these two types of rupture in this region can be distinguished (appearance between the dendrites of same grain or grains).

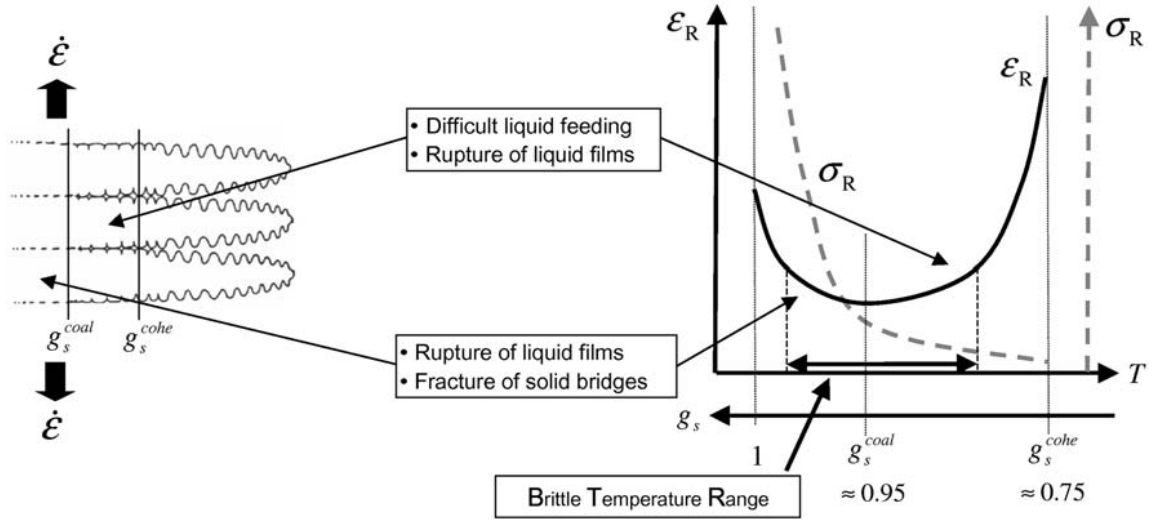

Figure 5 *Schematics of the main phenomena occurring in the mushy zone at characteristic solid fractions, explaining the loss of ductility in a given Brittle Temperature Range [Bellet 2009].*

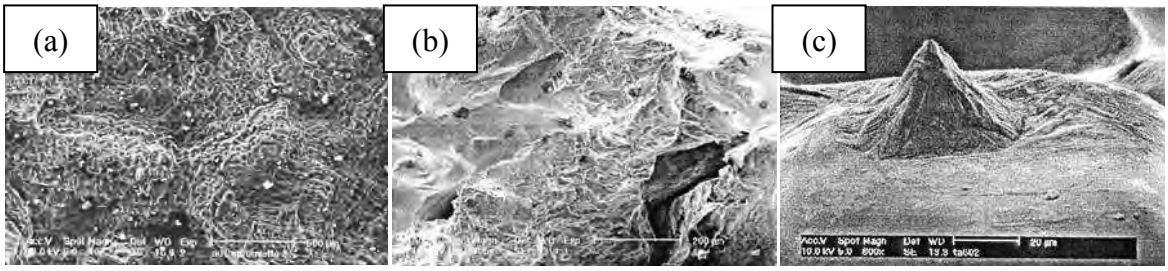

Figure 6 *Illustration of faces of fracture surface [Braccini 2000]: (a) brittle failure in interdendritic region, (b) ductile rupture of solid bridges, (c) observation of a peak of stretched liquid.*

3.2.3 Various parameters effect on hot tearing

(1) Influence of solidification interval

Chemical composition determines solidification interval. The larger the solidification interval is, the higher the hot tearing sensitivity becomes. The fragility strongly depends on the solidification path through the kinetic of liquid disappearance near the end of solidification. Consequently, hot tearing depends on the chemical composition, particularly for elements such as sulfur, phosphorus and boron: these elements make solidus temperature lower and hot tearing sensitivity increases [Wintz 1994]. The effect of sulfur can be prevented by adding manganese. Indeed, manganese favors

precipitation of (Fe,Mn)S intermetallic, with higher solidus temperature. The effect of carbon content is not as clear. While it is believed that carbon makes the solidification interval widen, it was observed that, over 0.3wt% carbon content in Fe-C alloy, the higher the carbon content is, the smaller the hot tearing risk becomes [Pierer 2007].

(2) Influence of microstructure

The microstructure is linked to the solidification path. A fine microstructure decreases the sensitivity for the appearance of the rupture by the adaptation of the deformation: gliding at grain boundary can absorb deformation [Pierer 2007]. Ductility of the equiaxed structure is better than with columnar structure [Eskin 2004]. The microstructure also influences the mechanical behavior in the mushy zone and the permeability.

The metallurgical phases in presence also influence the occurrence of hot tearing during solidification. Several studies illustrate this influence in the case of stainless steels [Katayama 1985] and [Kotecki 1993]. It is explained that it is more difficult to propagate the rupture in a mixed structure. This influence is verified using two elements, that is, sulfur and phosphorus. The result is that these two elements are easily soluble in ferrite but not in austenite; this means that the kinetic of the disappearance of the liquid near the end of solidification depends on the quantity of the austenite phase. In addition, shrinkage corresponding to the transformation from ferrite to austenite generates the deformation in the mush and modifies the hot tearing sensitivity.

Grain boundary misorientation angle has also an effect on the occurrence of hot tearing during solidification [Wang 2004]. Over a certain critical angle between two metallurgical grains, the undercooling required to overcome the repulsive forces before the grains bridge is large. As a consequence, and as illustrated in Figure 7, there is an extended region where interdendritic liquid films remain, creating a low strength zone along the future grain boundary. When a tensile strain is applied perpendicular to the average dendrite growth direction, hot tearing takes place preferably in this brittle region along the grain boundary.

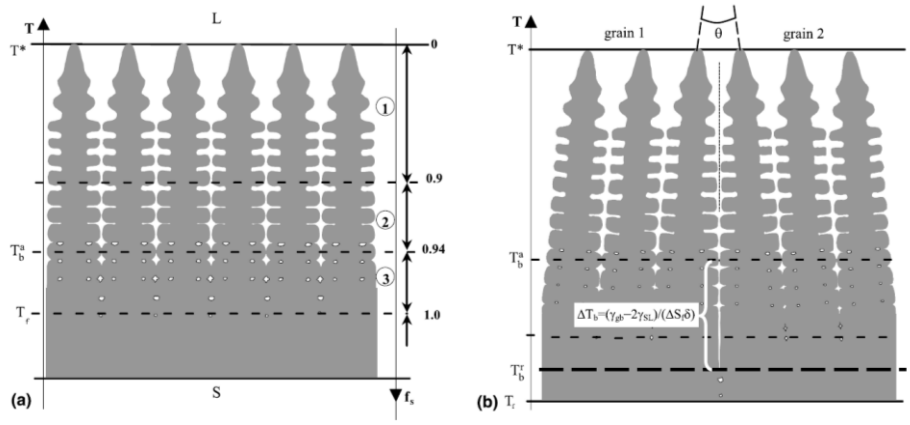

***Figure** 7 Schematic illustration from [Wang 2004] showing the effect of delayed coalescence in case of significant misorientation between grains. This leads to the persistence of liquid pockets along such grain boundaries below the nominal coalescence temperature of the single crystal.*

(3) Influence of solid/liquid wetting angle

The wetting angle at the interface of the solid also influences the sensitivity to hot tearing [Braccini 2000]. The wetting angle results in the capacity of the liquid to spread on the surface of the solid as a function of temperature and the liquid composition. This determines the distribution of the liquid film at the interface of the grains, that is, films are continued, discontinued or become pockets, shown as Figure 8. The angle is defined by $\gamma_{GB} = 2\gamma_{SL}\cos\theta$, where γ_{GB} and γ_{SL} are respectively the surface energy of the grain boundary and the surface energy of the liquid-solid interface. Figure 8 shows typical distribution of liquid as a function as the angle θ. Some tensile tests in a SEM to investigate the relation between the wetting angle and the rupture were carried out by Fredriksson and Lehtinen [Fredriksson 1979]. The authors show that the angle is null for Al-Sn alloys and hot tearing appears in the wetting grains. In the case of Al-Cd alloys, the angle is high and the wetted pockets do not influence the rupture. Finally the authors pointed out the role of the grain boundaries wetted by the liquid and oriented in a direction perpendicular to the traction rupture.

Thickness of the liquid film also influences the sensitivity to hot tearing. The larger the thickness is, the higher the appearance of the hot tearing becomes. However, it is necessary to investigate the characteristics of the liquid film at high temperature [Gerds 1976].

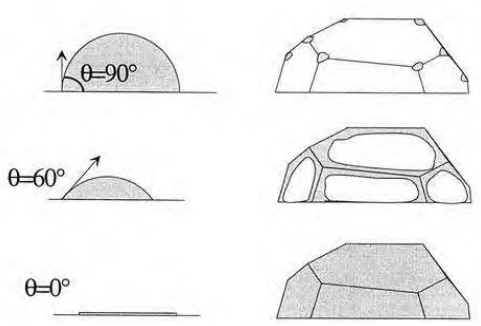

Figure 8 *Distributions of liquid film in a surface of a grain [Braccini 2000].*

(4) Influence of thermomechanics

Thermomechanics has an important role for the occurrence of hot tearing. Physical property of alloy is strongly associated with temperature. Thus, thermal evolution determines the mechanical effect, such as deformation and shrinkage. It results in a driving force for the occurrence of the hot tearing. Geometric effects (for instance, bending and unbending materials during solidification in continuous casting process) also lead to the appearance of hot tear.

3.3 Deformation induced segregation

As explained in the previous sections, macrosegregation results from deformation of the solidified shell in the CC process. In fact, deformation of the mush is the origin of macrosegregation. The mush is composed of solid and liquid phase. The mushy solid is considered as sponge like material which contains enriched liquid. When the sponge is in compression, the enriched liquid is expelled outside, leading to negative macrosegregation in the deformation area. When the sponge is in traction, the enriched liquid is sucked inside of the sponge, leading to positive macrosegregation. This is called deformation induced segregation and the liquid phase is transported with enriched solutes according to the mushy solid deformation. Concerning the intensity of the macrosegregation with respect to solute elements, solute for instance like P and S which have low partition coefficient makes strong segregation.

4. Prediction of hot tearing through numerical modelling

Regarding with modeling of hot tearing, there are several recent studies in this field. They can be divided into two groups; micro and macroscopic scale studies. The last decade has seen a significant development of numerical simulations directly operated at the scale of a Representative Elementary Volume (REV) of the mushy material, in view of encompassing most of the small-scale physical phenomena mentioned above. Phillion et al. [Phillion 2008] showed the influence of microstructual features on tensile deformation of a REV of semi-solid aluminum alloy. Sistaninia et al. [Sistaninia 2011] have developed a numerical simulation using a discrete element method in order to account for the strain inhomogeneity in the mushy zone due to crack initiation and propagation, in other words, direct simulation of hot tearing. Zaragoci et al. [Zaragoci 2012] considered a domain of few cubic millimeters deduced from in-situ X-ray tomography of a tensile test in an Al-Cu sample maintained in the mushy state. A finite element discretization of the 3D domain using the level set method and adaptive mesh refinement was conducted to accurately separate liquid films and grains. The liquid flow and grain deformation were calculated, intrinsic properties of the phases obeying a viscoplastic constitutive equation. However, in those recent works [Phillion 2008], [Sistaninia 2011] and [Zaragoci 2012], only fragments of the different physical phenomena taking part in hot tearing were accounted for. It can be thought that such small-scale models will develop in the future, integrating more and more relevant physical features, and thus will become useful tools for a better fundamental understanding of hot tearing. But upscaling of such models to deduce rules that can be applied at the processing scale, such as in continuous casting, will require time due to their computational cost and actual approximations of the physical phenomena. Therefore, it is necessary to focus on more macroscopic analysis methods to study hot tearing. Those constitute the second group of researches mentioned previously, if one is targeting process scale applications. In the literature, lots of studies have proposed hot tearing criteria based on thermal considerations [Clyne 1977], solid mechanics [Prokhorov 1962], [Rogberg 1987], [Nagata 1990], [Yamanaka 1991], [Won 2000], [Cerri 2007] and [Bellet 2009] or solid and fluid mechanics [Rappaz 1999]. Cerri et al. [Cerri 2007], [Bellet 2009] have evaluated four of those hot tearing criteria for steels [Clyne 1977], [Prokhorov 1962], [Won 2000] and [Rappaz 1999] by means of constrained shrinkage tests and ingot bending tests. Systematic numerical simulation of the tests was conducted with the finite element package THERCAST® equipped with the different macroscopic criteria. The authors concluded that the only criterion able to

show a qualitative agreement with the experimental tests was the strain-based criterion proposed by Won et al. [Won 2000]. They proposed an enriched expression to reach quantitative agreement [Cerri 2007], [Bellet 2009]. In addition, Pierer et al. [Pierer 2007] evaluated, by use of submerged split chill tensile tests, a stress-based criterion [Rogberg 1987], a strain-based criterion [Won 2000], a criterion based on strain rate and including liquid feeding consideration [Rappaz 1999] and a criterion based on the sole BTR value [Clyne 1977]. The authors found that only the stress-based criterion and the strain-based criterion had good capability for predicting hot tearing. As a consequence, in the framework of the present study, we will essentially focus on hot tearing criteria based on critical strain.

5. Prediction of macrosegregation by numerical modeling

Several researchers studied these phenomena in the context of CC process with numerical modeling. Miyazawa and Schwerdtfeger [Miyazawa 1981] modelled solidification and macrosegregation, considering bulging between support rolls and the associated mushy zone deformation. In their model, mass, liquid phase momentum, solute and energy conservation equations are described in a fully Eulerian approach. The solid phase momentum equation is not solved so the velocity fields of the solid shell and of the solid phase in the central mushy region are arbitrarily given. The numerical simulation shows the formation of a center line with positive macrosegregation due to bulging. Kajitani et al. [Kajitani 2001] and Mayer et al. [Mayer 2010] studied the so-called soft reduction process using the same approach and discussed the quantitative impact of the soft reduction technique to reduce the intensity of the central macrosegregation. Fachinotti et al. [Fachinotti 2006] developed a different approach to model the mushy zone in the context of CC, using an arbitrary Lagrangian-Eulerian approach in which solid and liquid velocity fields are concurrently solved for, avoiding then the strong hypothesis over the solid velocity field which was present in previous works. With this model, the authors simulated continuous casting and similarly retrieved the effect of bulging on the formation of central macrosegregation [Bellet 2007]. More recently, Rivaux [Rivaux 2011] developed an alternative approach to model the deformation of the solid phase and its Darcy-type interaction with the liquid phase in the mushy state, through a staggered scheme in which the two fields are separately and successively solved for at each time increment. However, in the end, it should be said that despite lot of efforts in developing those numerical models, none of them has been successfully applied up to the scale of a 3D simulation representative of the complexity of the industrial process. This is certainly due to the considerable amount of computational power required to run the models encompassing a significant part of the secondary cooling section of an industrial caster.

6. Microsegregation modeling for multicomponent steels

Average alloy properties in multiphase temperature intervals are important for thermomechanical process simulations. Numerical tools have been developed to follow the transformation paths based on thermodynamic considerations. Two classical limits are routinely computed: the lever rule (LR) approximation and the Gulliver Scheil (GS) approximation [Gulliver 1913] and [Scheil 1943]. For LR, full equilibrium is assumed, meaning that all chemical elements can diffuse rapidly. In contrast, the GS approximation neglects diffusion in solid phases where elements are completely frozen. In practice, most industrial steels include interstitial and substitutional elements. Interstitial elements, such as carbon, have high diffusivity in the solid phase while substitutional elements have low diffusivity. Thus, the above LR and GS approximations do not fully apply. To overcome this problem, the partial equilibrium (PE) approximation [Chen 2002] and [Zhang 2013] has been developed. PE is intended to take into account perfect diffusion of interstitial elements but no diffusion of substitutional elements. However, the peritectic transformation often encountered in commercial alloys cannot take place if only PE is considered. This limitation could be circumvented by a LR treatment of the δ-BCC (or δ-ferrite)/γ-FCC (or γ-austenite) mixture during the peritectic transformation [Chen 2006], thus permitting the activation of the δ-BCC to γ-FCC phase transformation. This will be later refereed as PE+LR solidification path. It is to be mentioned that, while in agreement with observations, no experimental quantitative data is yet available that could be directly compared with predicted kinetics of the peritectic phase transformation. The LR treatment of the peritectic transformation is also a very crude approximation that does not fix the problem in coherent manner with respect to the PE approximation.

In the present study, a new numerical scheme is presented for the computation of phase transformations in steels. It is coupled with thermodynamic equilibrium calculations based on call to the software Thermo-Calc [Thermo-Calc 2013] through the TQ-interface using the TCFE6 database [Shi 2008]. The so-called para-equilibrium (PA) approximation presented by Hillert [Hillert 1998] has been introduced to deal with the peritectic reaction during a PE solidification path, later refereed as PE+PA approximation. This is implemented in previous developments presented by Zhang et al. [Chen 2002] for the computation of LR, GS and PE+LR solidification paths. Because PA was initially developed for solid state transformations, it is also used to simulate phase transformations during cooling experienced during steel processing after solidification. The PA treatment allows the activation of the δ-BCC to γ-FCC phase

transformation during solidification with the consideration of perfect diffusion of interstitial elements but no diffusion of substitutional elements which is consistent with PE. The numerical scheme is applied to steel alloys experiments also presented in this contribution.

Concerning coupling between microsegregation modeling and macrosegregation modeling for steels, some researchers employed the simplest system; Fe-C binary system [Miyazawa 1981], [Kajitani 2001], [Fachinotti 2006] and [Mayer 2010]. The advantage of this case is to simplify the implementation into the code. In case of binary system, constant liquidus slope and partition coefficient are assumed and LR or GS could be applied. However, commercial steels are generally multicomponent system so that microsegregation modeling for multicomponent steels is required for application to the CC simulation or an experiment for steel. Recently, some researchers [Carozzani 2012, Saad 2016] have developed a model for multicomponent where enthalpy and solute concentration are tabulated a priori. According to the result of global resolution such as enthalpy, momentum and solute conservation equations, the code refers the table and chooses suitable values. With this model, peritectic transformation can be taken into account for and more realistic simulation could be performed.

In this present study, simple binary model is extended to multicomponent system with some assumptions for coupling the macrosegregation and microsegregation although peritectic transformation cannot be considered. This model gives access to analyze the effect of each solute elements and the consequent macrosegregation compared to the experiment with steels. The detail of the model is explained in the following chapter.

7. Numerical modeling

To understand and analyze the above two defects, numerical modeling is one of the powerful tools. Potentially, the advantage of the numerical model is to predict the defects. It is also possible to optimize casting conditions according to numerical simulation results. Therefore, one objective in this thesis is to develop a numerical model which would be able to give a reliable and detailed description of the main phenomena leading to the defects mentioned above. In terms of modeling of CC process, ANSYS-FLUENT [FLUENT] is quite well known to be applied to melt flow modeling in tundish and mould. Regarding with modeling of slab deformation in secondary cooling process, THERCAST [Bellet 2004] and [Bellet 2005] developed by Transvalor strongly supported by CEMEF, MINES Paristech, is one of the solution because it is dedicated to the CC process modeling, especially secondary cooling process with deformation. It can be performed in three dimensional modeling with finite element approach. Regarding macrosegregation modeling in the CC, R2SOL [Fachinotti 2006] already developed at CEMEF is also dedicated to secondary cooling process especially with mushy zone deformation and solute transport modeling with finite element approach. Although the modeling is limited to two dimensions, solving deformation of the mush together with solute transport phenomena is quite interesting to understand what happens in the slab. As mentioned above, microsegregation is key role to hot tearing and macrosegregation phenomena. In addition, average alloy properties in multiphase temperature intervals are important for thermomechanical process simulations. Therefore, microsegregation modeling is interesting. In this study, Thermocalc [Thermo-Calc 2013] with thermodynamic consideration is used. Although boundary condition is limited, like full solute diffusion or not, realistic solidification path and thermo physical properties with multicomponent alloy would be obtained.

7.1 Presentation of THERCAST®

The numerical simulation of the experiments consists of a thermomechanical stress/strain analysis. It is conducted using the 3D finite element code THERCAST®. The essential characteristics of the code can be found in References [Bellet 2004] and [Bellet 2005]. Non-linear average conservation equations for the total mass, momentum and energy are solved at each time increment on all interacting domains. The solution covers the whole domain occupied by the metal, whatever its state: liquid, solid, or mushy and the components of the modeling system. The semi-solid steel (composed of

liquid and solid phases) is simply considered as a homogenized continuum with averaged properties and a unique average velocity field **v**. The thermal problem and the mechanical problem are solved sequentially at each time increment. First, the average energy conservation is solved in all domains taking into account heat exchange between them. This equation can be expressed by:

$$\rho \frac{dh}{dt} = \nabla \cdot (\lambda \nabla T) \tag{1}$$

where ρ is the average density, h is the average specific enthalpy per unit mass, λ is the average thermal conductivity and T is the temperature. Second, the mechanical problem is considered. The following average momentum and mass conservation equations are solved concurrently in the framework of a velocity-pressure formulation.

$$\begin{cases} \nabla \cdot \mathbf{s} - \nabla p + \rho \mathbf{g} - \rho \boldsymbol{\gamma} = 0 \\ \mathrm{tr}\, \dot{\boldsymbol{\varepsilon}}^{\mathrm{vp}} = 0 \end{cases} \tag{2}$$

where **s** is the deviatoric stress tensor, p is the pressure, **g** is the gravity vector, $\boldsymbol{\gamma}$ is the acceleration vector and $\dot{\boldsymbol{\varepsilon}}^{\mathrm{vp}}$ is the viscoplastic part of the strain rate tensor:

$$\dot{\boldsymbol{\varepsilon}} = (\nabla \mathbf{v} + \nabla^{\mathrm{T}} \mathbf{v})/2 \tag{3}$$

The strain rate tensor is expressed as the sum of three different contributions:

$$\dot{\boldsymbol{\varepsilon}} = \dot{\boldsymbol{\varepsilon}}^{el} + \dot{\boldsymbol{\varepsilon}}^{vp} + \dot{\boldsymbol{\varepsilon}}^{th} \tag{4}$$

where $\dot{\boldsymbol{\varepsilon}}^{\mathrm{th}}$ is the thermal strain rate tensor. The alloy is modeled with a hybrid constitutive equation. Details can be found elsewhere [Thomas 2008], only main lines being recalled here. Over the solidus temperature, the alloy is considered as a non-Newtonian fluid obeying a temperature-dependent viscoplastic multiplicative law, as follows:

$$\overline{\sigma} = K\left(\sqrt{3}\right)^{m+1} \dot{\bar{\varepsilon}}^{m} \tag{5}$$

where $\overline{\sigma}$ is the equivalent von Mises stress, K is the viscoplastic consistency, $\dot{\bar{\varepsilon}}$ is the generalized strain rate and m is the strain rate sensitivity. The value of m over the liquidus temperature is equal to 1 (Newtonian fluid). In the frame of the present study, liquid flow in liquid regions is ignored and the liquid viscosity is defined as 10 Pa s for

numerical stability reasons. Below the solidus temperature, the alloy obeys an elastic-viscoplastic constitutive equation, expressed by:

$$\bar{\sigma} = K\left(\sqrt{3}\right)^{m+1} \dot{\bar{\varepsilon}}^{m} + H\bar{\varepsilon}^{n} \tag{6}$$

in which $\bar{\varepsilon}$ is the cumulated plastic strain, H is the strain hardening coefficient and n is the strain sensitivity. Physical properties and constitutive parameters are temperature dependent.

7.2 Presentation of R2SOL

The macrosegregation forms due to concurrent deformation of the solid phase in the mushy zone, and from the liquid flow induced by this deformation. In order to consider separately - but solve concurrently - for the liquid and solid velocity fields in the mushy zone, we apply the so-called "two-phase" model initially developed by Bellet et al. [Fachinotti 2006] and [Bellet 2007] to address macrosegregation in continuous casting. This model allows simulating solute transport phenomena leading to macrosegregation induced by deformation, shrinkage and advection. It is performed with the 2D finite element code R2SOL. The main assumptions and features of the model are reminded hereafter.

- The conservation equations for the solid-liquid mixture are expressed on a representative elementary volume (REV) and are obtained using the spatial averaging method [Ni 1991].
- The mushy material is considered as a saturated two-phase medium only made of solid, s, and liquid, l (i.e. no porosity and $g_s + g_l = 1$ where g_k denotes the volume fraction of phase k).
- At the so-called microscopic scale, within the REV, the liquid phase is considered as an incompressible Newtonian fluid. After spatial averaging, the macroscopic behavior of the liquid phase is Newtonian compressible.
- In the same way, the solid phase is considered intrinsically as an incompressible non-Newtonian fluid, and its macroscopic averaged behavior is the one of a compressible non-Newtonian fluid for which inertia effects are neglected.
- The momentum interaction between solid and liquid phases is formulated with an isotropic Darcy law.

- Solidification shrinkage is taken into account by considering different densities for the solid and liquid phases, respectively ρ_S and ρ_L. Those values are assumed constant within the solidification interval.
- A multi component system under lever rule approximation is assumed, meaning that the partition coefficient k_i and the liquidus slope m_i are constant for each solute element i.
- Local thermal equilibrium holds within the REV, ensuring the uniformity of temperature within the different phases.

The previous assumptions lead to the following set of averaged conservation equations:

$$\nabla \cdot \boldsymbol{\Sigma}^s - g_s \nabla p_l + {g_l}^2 \mu_l \kappa^{-1} (\mathbf{v}_l - \mathbf{v}_s) + g_s \rho_S \mathbf{g} = 0 \tag{7}$$

$$\nabla \cdot \left\langle \mathbf{s}^l \right\rangle - g_l \nabla p_l - {g_l}^2 \mu_l \kappa^{-1} (\mathbf{v}_l - \mathbf{v}_s) + g_l \rho_L \mathbf{g} = \rho_L \frac{\partial (g_l \mathbf{v}_l)}{\partial t} + \rho_L \nabla \cdot (g_l \mathbf{v}_l \times \mathbf{v}_l) \tag{8}$$

$$\nabla \cdot (g_l \mathbf{v}_l) + \frac{\rho_S}{\rho_L} \nabla \cdot (g_s \mathbf{v}_s) = \left(\frac{\rho_L - \rho_S}{\rho_L} \right) \frac{\partial g_s}{\partial t} \tag{9}$$

$$\langle \rho \rangle \frac{\partial \langle h \rangle}{\partial t} + \nabla \langle h \rangle \cdot \langle \rho \mathbf{v} \rangle + L \nabla \cdot (g_l g_s \langle \rho \rangle (\mathbf{v}_l - \mathbf{v}_s)) - \nabla \cdot (\langle \lambda \rangle \nabla T) = 0 \tag{10}$$

$$\frac{\partial \langle w_i \rangle}{\partial t} + \nabla \cdot (\langle w_i \rangle \mathbf{v}_s) + \nabla \cdot (g_l w_{l,i} (\mathbf{v}_l - \mathbf{v}_s)) - \nabla \cdot (g_l D_{l,i} \nabla w_{l,i}) = 0 \tag{11}$$

in which $\mathbf{v}_s$ and $\mathbf{v}_l$ are the solid and liquid velocity vectors (intrinsic average phase velocities: $\mathbf{v}_l \equiv \left\langle \mathbf{v}^l \right\rangle^l$; $\mathbf{v}_s \equiv \left\langle \mathbf{v}^s \right\rangle^s$), p_l is the liquid phase pressure ($p_l \equiv \left\langle p^l \right\rangle^l$), μ_l is the dynamic viscosity of the liquid phase, $\langle \rho \rangle$ and $\langle \lambda \rangle$ are the average density and the average heat conductivity of the solid-liquid mixture, $\langle h \rangle$ is the average enthalpy of the mixture. $\langle w_i \rangle$ and $w_{l,i}$ are respectively the average solute mass concentration and the intrinsic average concentration in the liquid phase for each solute i. In the momentum equations, the Darcy term introduces the permeability κ of the porous medium constituted by the solid phase. It is derived from the liquid volume fraction and the secondary dendrite arm spacing λ_2, through the Carman-Kozeny model.

$$\kappa = \frac{{\lambda_2}^2 {g_l}^3}{180(1-g_l)^2} \tag{12}$$

Constitutive models for the liquid and the solid phases in the mushy zone are presented in detail in references [Fachinotti 2006] and [Bellet 2007]. In summary, the average deviatoric stress tensor in the liquid phase is expressed by:

$$\left\langle \mathbf{s}^l \right\rangle = 2\mu_l \, g_l \, \mathrm{dev}\big(\dot{\boldsymbol{\varepsilon}}(\mathbf{v}_l)\big) = 2\mu_l \, g_l \left(\dot{\boldsymbol{\varepsilon}}(\mathbf{v}_l) - \frac{1}{3}\mathrm{tr}(\dot{\boldsymbol{\varepsilon}}(\mathbf{v}_l)) \right) \tag{13}$$

where $\dot{\boldsymbol{\varepsilon}}(\mathbf{v}_l)$ is the symmetric part of the liquid velocity gradient $\nabla \mathbf{v}_l$. For solid, it is assumed that the behavior of the fully solid material is viscoplastic, of power law type, as will be introduced later. The strain-rate sensitivity coefficient of the fully solid material being denoted *m*, it can be shown that the effective macroscopic stress tensor for the solid phase in the mushy state, $\boldsymbol{\Sigma}^s = \langle \boldsymbol{\sigma} \rangle + p_l \mathbf{I}$, is a degree *m* homogeneous function with respect to the strain rate tensor $\langle \dot{\boldsymbol{\varepsilon}} \rangle^s = \dot{\boldsymbol{\varepsilon}}(\boldsymbol{v}_s)$. Adopting a compressible viscoplastic potential, its expression writes:

$$\begin{aligned} \boldsymbol{\Sigma}^s &= 3K(\sqrt{3}\langle \dot{\bar{\varepsilon}} \rangle^s)^{m-1} \left(\frac{1}{A}\langle \dot{\boldsymbol{\varepsilon}} \rangle^s + \left(\frac{1}{9B} - \frac{1}{3A} \right) \mathrm{tr}\langle \dot{\boldsymbol{\varepsilon}} \rangle^s \mathbf{I} \right) \\ &= 3K(\sqrt{3}\langle \dot{\bar{\varepsilon}} \rangle^s)^{m-1} \left(\frac{1}{A}\mathrm{dev}(\langle \dot{\boldsymbol{\varepsilon}} \rangle^s) + \frac{1}{9B}\mathrm{tr}\langle \dot{\boldsymbol{\varepsilon}} \rangle^s \mathbf{I} \right) \end{aligned} \tag{14}$$

in which *K* is the viscoplastic consistency of the solid material and *m* its strain rate sensitivity, both taken at the solidus temperature. The equivalent strain rate $\langle \dot{\bar{\varepsilon}} \rangle^s$ is expressed by

$$\left\langle \dot{\bar{\varepsilon}} \right\rangle^s = \left(\frac{1}{A} \left\langle \dot{\boldsymbol{\varepsilon}} \right\rangle^s : \left\langle \dot{\boldsymbol{\varepsilon}} \right\rangle^s + \left(\frac{1}{9B} - \frac{1}{3A} \right) (\mathrm{tr} \left\langle \dot{\boldsymbol{\varepsilon}} \right\rangle^s)^2 \right)^{\frac{1}{2}}$$
$$= \left(\frac{1}{A} \mathrm{dev}(\left\langle \dot{\boldsymbol{\varepsilon}} \right\rangle^s) : \mathrm{dev}(\left\langle \dot{\boldsymbol{\varepsilon}} \right\rangle^s) + \frac{1}{9B} (\mathrm{tr} \left\langle \dot{\boldsymbol{\varepsilon}} \right\rangle^s)^2 \right)^{\frac{1}{2}} \tag{15}$$

In the flow rule (Eq. (14)), A and B are two rheological coefficients depending on the solid volume fraction. In the present study, the expressions introduced in reference [Fachinotti 2006] are used:

$$B = k_B \frac{1 - g_s}{g_s - g_s^{crit}} \qquad A = \frac{3}{2}(1 + k_A B) \tag{16}$$

The values of the parameters are taken from the same reference. Taking the trace of Eq. (14), it can be seen that the compressibility of the solid phase is essentially controlled by the value of coefficient B:

$$\mathrm{tr}\, \boldsymbol{\Sigma}^s = K(\sqrt{3} \left\langle \dot{\bar{\varepsilon}} \right\rangle^s)^{m-1} \frac{1}{B} \mathrm{tr} \left\langle \dot{\boldsymbol{\varepsilon}} \right\rangle^s \tag{17}$$

As expressed by Eq. (16a), g_s^{crit} can be seen as the coherency solid volume fraction at which the compressibility of the solid phase is extremely high ($B \to \infty$). Conversely, when the solid fraction tends to one (fully solid material), A and B tend toward 3/2 and 0, respectively: the usual power law relating stress and strain rate for a dense metal at high temperature is retrieved.

In the finite element code, the weak (integral) form of Eqs. (7) to (11) is implemented in 2D triangular finite elements. At each time increment, the sequence of numerical resolutions is as follows:

- The *thermal resolution* is operated on the set of the different domains involved: in the present context, the solidifying ingot, the different components of the mold, and the pressing punch. The (non-linear) heat transfer resolution is carried out on each domain, successively, up to convergence (i.e. stabilization of the temperature field). In the ingot, a finite element (FE) resolution of Eq. (10) is done, while in the other domains a more classical single phase form of heat diffusion is solved. Heat

exchanges at interfaces between domains are expressed by the Fourier law, using heat transfer coefficients.

- The *macrosegregation resolution* is performed in the ingot, through a FE resolution of Eq. (11) for each considered solute *i*. In these resolutions, like in the thermal one, the microsegregation model (here the lever rule) is considered as it links the average concentrations in the liquid phase $w_{l,i}$ with the average mixture concentrations $\langle w_i \rangle$, and the averaged enthalpy $\langle h \rangle$ with the temperature *T*.
- The *mechanical resolution* is performed in the ingot, the other domains being assumed perfectly rigid and fixed. A non-linear Newton-Raphson algorithm is used, providing the nodal values of $\mathbf{v}_s$, $\mathbf{v}_l$ and p_l through a single FE resolution of Eqs. (7) to (9). As the mechanical formulation presented above encompasses the central mushy zone and the fully solidified regions, a specific treatment applies. In the finite element assembly procedure, elements are considered either mushy or fully solid, according to the temperature at their center. In mushy elements, the contribution to the residue directly results from the weak form of Eqs. (7) to (9). In fully solid elements, it can be noted that, by applying these equations, the liquid velocity is still present but has no real physical meaning: it is then kept close to the solid velocity field by means of the sole Darcy term in the liquid momentum equation, acting as a penalty term. The deviatoric stress tensor **s** is expressed as a function of the velocity field by the viscoplastic Norton-Hoff power law including strain hardening:

$$\mathbf{s} = 2K\bar{\varepsilon}^n(\sqrt{3}\dot{\bar{\varepsilon}})^{m-1}\mathrm{dev}(\dot{\boldsymbol{\varepsilon}}) \tag{18}$$

where $\mathrm{dev}(\dot{\boldsymbol{\varepsilon}})$ denotes the deviatoric part of the strain rate tensor, *K* the viscoplastic consistency, *m* the strain rate sensitivity coefficient, $\dot{\bar{\varepsilon}}$ the generalized strain rate and $\bar{\varepsilon}$ the generalized strain. Strain-hardening is assumed null at solidus temperature and over. This is why only *K* (and not $K\bar{\varepsilon}^n$) appears in Eq.(14) to express the behavior model of the solid phase in the mush. The tensor equation (18) yields the one dimensional relation between the von Mises stress $\bar{\sigma}$ and the generalized strain-rate $\dot{\bar{\varepsilon}}$:

$$\bar{\sigma} = K(\sqrt{3})^{m+1}\bar{\varepsilon}^n\dot{\bar{\varepsilon}}^m \tag{19}$$

The fully solid metal is then plastically incompressible and this is why Eq. (9) is replaced in the finite elements which are found fully solid (temperature at center lower than the solidus temperature) by the following equation which simply accounts for thermal dilatation terms:

$$\nabla \cdot \mathbf{v}_s + \frac{1}{\rho_s(T)} \frac{\mathrm{d}\rho_s(T)}{\mathrm{d}t} = 0 \tag{20}$$

8. Large scale experiment

In order to understand solidification defects; hot tearing and macrosegregation, a large scale experiment developed at Nippon Steel & Sumitomo Metal is employed. Its view is shown in Figure 9. In the late 1970s, such a large scale ingot punching test has been developed by steel industries in Japan [Sato 1975], [Miyamura 1976], [Marukawa 1978], [Narita 1978] and [Sugitani 1980] to estimate the CC-process viability. Such test has been also developed in Europe [Wintz 1994] in 1990s. They consist in bending, punching, or pressing the solidifying shell of an ingot during its solidification by means of a punch moved perpendicularly to the shell plane (or surface of the ingot), i.e. along the dendritic growth direction when solidification proceeds directionally away from the mold walls. The size of the ingot and the control of the bending/punching conditions have to represent the solicitations undergone by the solid shell during CC when it passes by the support rolls. Note that in CC, the alloy also endures the metallostatic pressure which induces bulging between each roll stand. The concept of the apparatus is similar to the above references, the deformation being applied on an ingot which is not fully solidified. The steel ingot thickness is 0.16 m so that solidification time is close to real process, around 15 min. It gives similar solidification microstructure and defects. What is nice in this named ingot punch pressing test is to control deformation using a servo hydraulic cylinder, saying that displacement and velocity of the punch are easily controlled. In addition to the control of deformation, solidification progress is monitored using thermocouple in the ingot. Using this monitoring together with numerical modeling, it is then possible to predict the ingot core solidification. At last, the defects like hot tearing and macrosegregation are successfully created. The detail of the experiment is presented in following chapter.

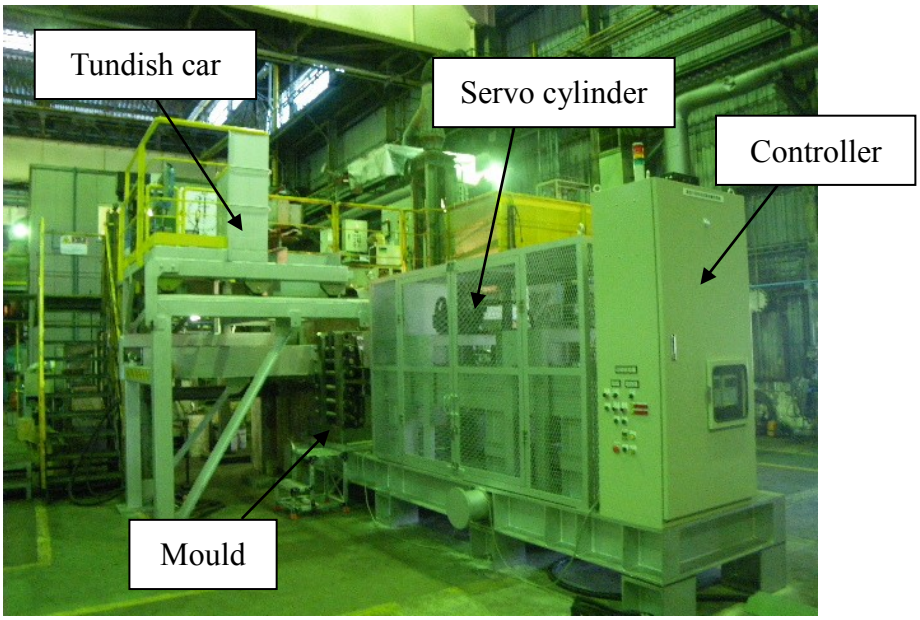

Figure 9 *Entire view of ingot pressing test developed at Nippon Steel & Sumitomo Metal Corporation. Steel mould is located at the centre of the photo and 450 kg molten metal is prepared in a ladle over the mould and it is introduced into the mould through a tundish. In fact, the servo cylinder which is in change to the punch movement and so the deformation on an ingot.*

This thesis consists of 3 articles; Chapter II explains microsegregation modeling for multicomponent steels based on thermodynamical point of view. A new numerical scheme is developed and the simulation results are discussed with experimental results. Chapter III presents prediction of hot tearing through 3D thermomechanical modeling with ingot punch pressing test. An excellent correlation in between the numerical results and observed cracks are seen and solidification path effect is then discussed. Chapter IV is linked to prediction of macrosegregation by 2D numerical modeling with ingot punch pressing test. The numerical simulation results show the essential of the driving force of the generation of macrosegregation. Chapter V and VI are then summary and perspective.

Chapter II

Computation of Phase Transformation Paths in Steels by a Combination of the Partial- and Para-equilibrium Thermodynamic Approximations

Takao KOSHIKAWA, Charles-André GANDIN, Michel BELLET, Hideaki YAMAMURA and Manuel BOBADILLA

DOI: http://dx.doi.org/10.2355/isijinternational.54.1274

Pages: 30 to 40 in this thesis

ISIJ International, Vol. 54 (2014), No. 6, pp. 1274–1282

Computation of Phase Transformation Paths in Steels by a Combination of the Partial- and Para-equilibrium Thermodynamic Approximations

Takao KOSHIKAWA,[1,2)]* Charles-André GANDIN,[1)] Michel BELLET,[1)] Hideaki YAMAMURA[3)] and Manuel BOBADILLA[4)]

1) MINES ParisTech & CNRS, CEMEF UMR 7635, 06904 Sophia Antipolis, France.
2) Nippon Steel & Sumitomo Metal Corporation, Oita Works Equipment Division, 1 Oaza-Nishinosu, Oita City, Oita Prefecture, 870-0992 Japan. 3) Nippon Steel & Sumitomo Metal Corporation, Steelmaking R&D Division, 20-1 Shintomi, Futtsu City, Chiba Prefecture, 293-8511 Japan.
4) ArcelorMittal Maizières, Research and Development, BP 30320, 57283 Maizières-lès-Metz Cedex, France.

(*Received on August 29, 2013; accepted on February 13, 2014*)

A model combining the partial-equilibrium and para-equilibrium thermodynamic approximations is presented. It accounts for fast diffusion of interstitial elements, such as carbon, and low diffusion of substitutional elements in the solid phases, while complete mixing is assumed for all elements in the liquid phase. These considerations are turned into classical mathematical expressions for the chemical potentials and the u-fractions, to which mass conservation equations are added. The combination of the two models permits application to steels, dealing with partial-equilibrium for solidification and para-equilibrium for both the δ-BCC to γ-FCC peritectic transformation and the γ-FCC to α-BCC solid state transformation. The numerical scheme makes use of calls to Thermo-Calc and the TQ-interface for calculating thermodynamic equilibrium and accessing data from the TCFE6 database. Applications are given for a commercial steel. The results are discussed based on comparison with classical microsegregation models and experimental data.

KEY WORDS: solidification; microsegregation; partial-equilibrium; para-equilibrium; peritectic transformation.

1. Introduction

Average alloy properties in multiphase temperature intervals are important for thermomechanical process simulations. Numerical tools have been developed to follow the transformation paths based on thermodynamic considerations. Two classical limits are routinely computed: the lever rule (LR) approximation and the Gulliver-Scheil (GS) approximation.[1,2)] For LR, full equilibrium is assumed, meaning that all chemical elements can diffuse rapidly. In contrast, the GS approximation neglects diffusion in solid phases where elements are completely frozen. In practice, most industrial steels include interstitial and substitutional elements. Interstitial elements, such as carbon, have high diffusivity in the solid phase while substitutional elements have low diffusivity. Thus, the above LR and GS approximations do not fully apply. To overcome this problem, the partial-equilibrium (PE) approximation[3,4)] has been developed. PE is intended to take into account perfect diffusion of interstitial elements but no diffusion of substitutional elements. However, the peritectic transformation often encountered in commercial alloys cannot take place if only PE is considered. This limitation could be circumvented by a LR treatment of the δ-BCC (or δ-ferrite)/γ-FCC (or γ-austenite) mixture during the peritectic transformation,[5)] thus permitting the activation of the δ-BCC to γ-FCC phase transformation. This will be later refereed as PE + LR solidification path. It is to be mentioned that, while in agreement with observations, no experimental quantitative data is yet available that could be directly compared with predicted kinetics of the peritectic phase transformation. The LR treatment of the peritectic transformation is also a very crude approximation that does not fix the problem in coherent manner with respect to the PE approximation.

In the present study, a new numerical scheme is presented for the computation of phase transformations in steels. It is coupled with thermodynamic equilibrium calculations based on call to the software Thermo-Calc[6)] through the TQ-interface using the TCFE6 database.[7)] The so-called para-equilibrium (PA) approximation presented by Hillert[8)] has been introduced to deal with the peritectic reaction during a PE solidification path, later refereed as PE + PA approximation. This is implemented in previous developments presented by Zhang *et al*.[4)] for the computation of LR, GS and PE + LR solidification paths. Because PA was initially developed for solid state transformations, it is also used to simulate phase transformations during cooling expe-

* Corresponding author: E-mail: takao.koshikawa@mines-paristech.fr
DOI: http://dx.doi.org/10.2355/isijinternational.54.1274

rienced during steel processing after solidification. The numerical scheme is applied to steel alloys experiments also presented in this contribution.

2. Experiments

2.1. Unidirectional Solidification Experiment

To investigate solidification path in Fe–C–Mn–S–Si–P–Al steels, Bridgman solidification experiments have been carried out. The principle of this classical method is explained elsewhere.[9,10] The sample is prepared with a 1 kg furnace. The nominal composition of the investigated alloy S-1 is shown in **Table 1**. The specimen was shaped to 5 mm diameter rod. After setting the sample to the apparatus, it was heated over the liquidus temperature in the hot zone of the Bridgman apparatus and then withdrawn at a constant velocity toward the cold zone, thus achieving solidification. The velocity was set to $8{\cdot}10^{-5}$ m s^{-1}. The measured temperature gradient along the main longitudinal axis of the sample reached 30°C cm^{-1} during the experiment. The sample was finally quenched while still mushy in order to abruptly solidify the remaining liquid. One could thus distinguish the remaining liquid quenched into a fine microstructure from the solid phase formed before quenching. The sample was cut along transverse sections at various heights along the rod axis. The fraction of the solid phase formed before quenching was then estimated by means of image analysis at each transverse section. The evolution of the solid fraction versus position along the length of the rod could be deduced. Using the temperature gradient, the length was converted into a temperature. A profile of solid fraction versus temperature could then be plotted. Note that even during the quenching process, solidification of the previously formed solid could continue. The profile is thus considered as an overestimate of the solid fraction (underestimate of the remaining liquid fraction) prior to quenching. To estimate the liquidus temperature, differential thermal analysis (DTA) was used on heating rate 15°C/min for the steel S-1-DTA given in Table 1. The apparatus used is a SETARAM Thermobalance, with 10 mm height - 5 mm outer diameter alumina crucibles. The sample weight is around 500 mg. Note that other reactions, such as eutectic, were not detected with sufficient precision to be used.

2.2. EPMA Measurement on a Steel Alloy Sample

Electron Probe Micro-Analysis (EPMA) was carried out on a 3 cm × 5 cm × 1 cm sample extracted from the center of a 450 kg ingot casting (0.5 m width, 0.16 m thickness and 0.75 m height), in a region where no macrosegregation was observed. Its nominal composition, S-2, is given in Table 1. After polishing, EPMA was performed for manganese, phosphor and sulfur with a 5 μm diameter beam spot. The beam current was set to 0.5 A, the integration time was 0.5 s and the measurement step was 50 μm. The analyzed area was 10 mm × 5 mm with a total number of probed points reaching 20 000. Sorting methods proposed in literature were used,[11] namely the Flemings-Gungor (FG) sort and the Weighted Interval Rank Sort (WIRS). FG is the simplest approach, in which all solutes are sorted independently as ascending order of the concentration. Only ascending order is employed since partition coefficients for manganese, phosphor and sulfur are less than unity. Each ordered data are assigned with a rank number from 1 to the total number of measurement points. Finally, the assigned rank is divided by the total number of points, providing with an estimation of the solid fraction. A chemical composition versus solid fraction curve could thus be drawn. WIRS takes into account the probed measurement data uncertainty in order to weight the compositions. The uncertainty is estimated by the difference between the average composition measured by EPMA and the nominal composition. The weighted compositional value is averaged at each probed position and the data are sorted according to the average weighted compositional values in ascending order. For a better analysis, the sorted data are finally averaged in each 0.01 solid fraction range.

Table 1. Nominal compositions (mass%) of steel alloys studied.

	Fe	C	Mn	S	Si	P	Al
S-1	Bal.	0.21	1.64	0.007	0.24	0.032	0.090
S-1-DTA	Bal.	0.20	1.50	0.007	0.22	0.020	0.024
S-2	Bal.	0.20	1.47	0.010	0.22	0.020	0.038

3. Numerical Algorithm

Computations of advanced phase transformation paths are based on thermodynamic equilibrium calculations conducted with various conditions together with mass balances. The four basic approximations found in the literature[1–4] are reminded hereafter since they serve as the basis for the new combination derived in the present contribution.

3.1. Lever Rule (LR) Approximation

LR assumes complete mixing of all phases and thermodynamic equilibrium at interfaces, meaning that the chemical potential is equal in all phases for each chemical element. A close system is considered with constant mole, N_0, compositions, x_{i0}, and pressure P_0. It is defined by its n^p phases, including solid phases s_1, s_2, … plus a liquid phase l when present, *i.e.* p_j phases with $p_j = \{s_1, s_2, \ldots, 1\}$ and $j = [1, n^p]$, as well as its total number of chemical elements, n^s, including both interstitial and substitutional elements. The system is at temperature ${}^{(k-1)}T$ with an initial phase fraction, ${}^{(k-1)}N^{p_j}$, at composition, ${}^{(k-1)}x_i^{p_j}$, with $p_j = \{s_1, s_2, \ldots, 1\}$, $j = [1, n^p]$ and $i = [1, n^s]$. A small temperature decrease by ΔT is imposed to the system in order to compute its thermodynamic equilibrium at a lower temperature ${}^{k}T = {}^{(k-1)}T - \Delta T$. Mathematical formulation of LR first relies on equal chemical potential of each element respectively in all phases, ${}^{k}_{LR}\mu_i^{p_j}\left({}^{k}_{LR}x_i^{p_j}\right)$. Considering mass conservation in the system, the set of equations are obtained as follows:

$$ {}^{k}_{LR}\mu_i^{p_j}\left({}^{k}_{LR}x_i^{p_j}\right) = {}_{LR}Cst_i \qquad p_j = \{s_1, s_2, \ldots, 1\},\ j = [1, n^p],\ i = [1, n^s] \quad (1) $$

$$ \sum_{i=1}^{n^s} {}^{k}_{LR}x_i^{p_j} = 1 \qquad p_j = \{s_1, s_2, \ldots, 1\},\ j = [1, n^p],\ i = [1, n^s] \quad (2) $$

$$\sum_{j=1}^{n^p} {}^{k}_{LR}x_i^{p_j}\ {}^{k}_{LR}N^{p_j} = \sum_{j=1}^{n^p} {}^{(k-1)}x_i^{p_j}\ {}^{(k-1)}N^{p_j}$$

$$p_j = \{s_1, s_2, \ldots, 1\},\ j = [1, n^p],\ i = [1, n^s] \quad .. (3)$$

where ${}^{k}_{LR}N^{p_j}$ are phase fractions and ${}^{k}_{LR}x_i^{p_j}$ are compositions at equilibrium. The number of unknowns is $n^s(n^p+1)+n^p$: $n^s n^p$ compositions, n^p phase fractions plus n^s constant ${}_{LR}Cst_i$. The number of equations is the same: $n^s n^p$ Eq. (1), n^p Eq. (2) plus n^s Eq. (3). In the flow chart given in **Fig. 1**, this corresponds to the dashed rectangle on the left-hand-side. It should be noticed that the temperature step ΔT is somewhat arbitrary and should be chosen small enough to ensure convergence of the entire transformation path. A single value equal to 0.05°C was used hereafter for all calculations.

3.2. Gulliver-Scheil (GS) Approximation

GS[1,2] assumes complete mixing of the liquid and thermodynamic equilibrium at the solid/liquid interface, with no diffusion of the chemical elements in the solid phases. The system is at temperature ${}^{(k-1)}T$ with an initial phase fraction, ${}^{(k-1)}N^{pj}$, at average compositions, ${}^{(k-1)}\bar{x}_i^{p_j}$, with $p_j = \{s_1, s_2, \ldots, 1\}$, $j = [1, n^p]$ and $i = [1, n^s]$. A small temperature decrease by ΔT is imposed to a subsystem reduced to the above liquid, with initial phase fraction ${}^{(k-1)}N^1$ and compositions ${}^{(k-1)}x_i^1$, in order to compute a new thermodynamic equilibrium at a lower temperature, ${}^{k}T = {}^{(k-1)}T - \Delta T$, using Eqs. (1)–(3). In order to distinguish between LR (full equilibrium) and the present local equilibrium step for the remaining liquid, the output of the solution of Eqs. (1)–(3) are denoted with index EQ instead of LR: ${}^{k}_{EQ}N^{p_j}$ and ${}^{k}_{EQ}x_i^{p_j}$ with $p_j = \{s_1, s_2, \ldots, 1\}$, $j = [1, n^p]$ and $i = [1, n^s]$.

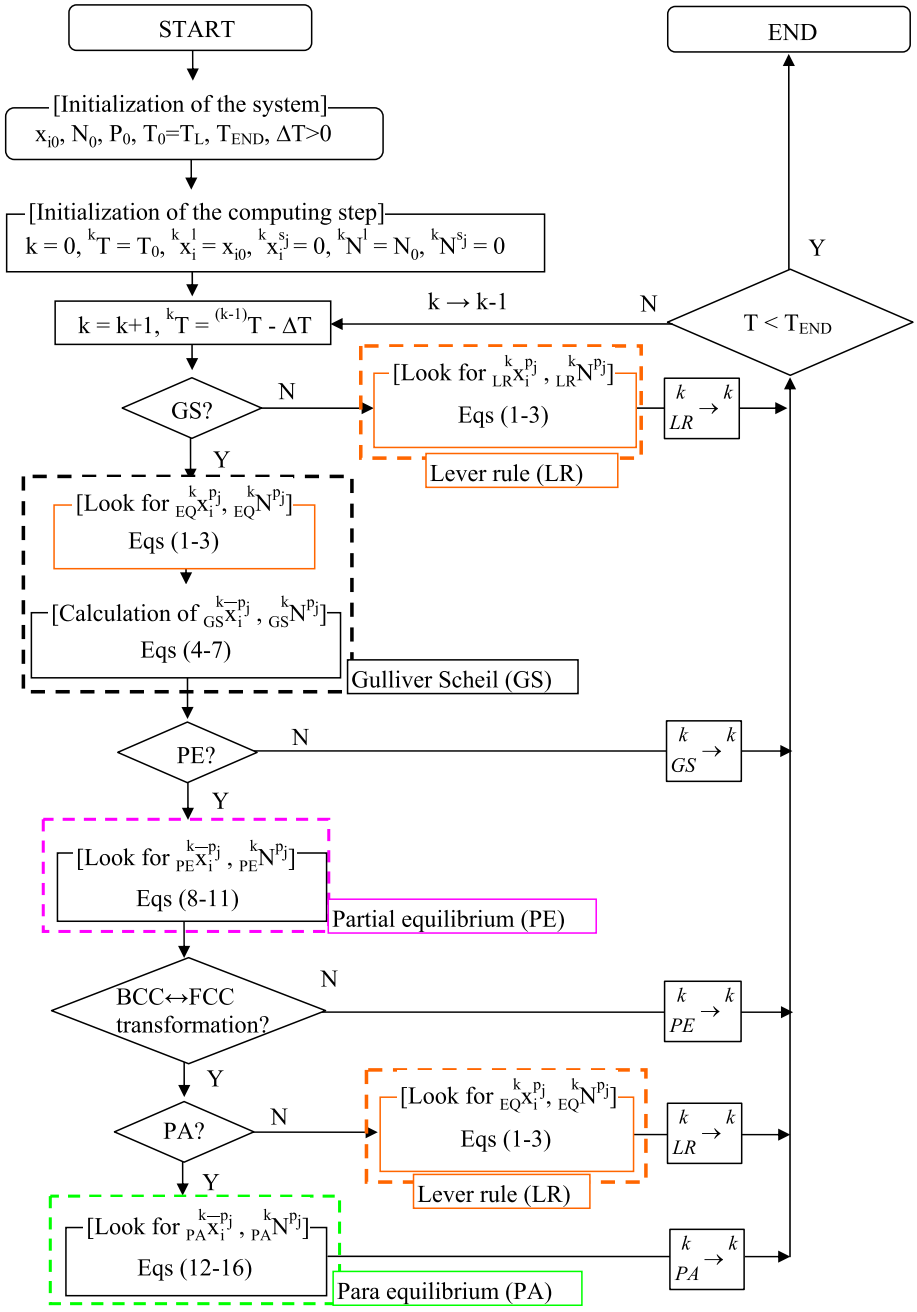

Fig. 1. Schematic of the numerical schemes accounting for combinations of various thermodynamic approximations: lever rule (LR), Gulliver-Scheil (GS), partial-equilibrium (PE) and para-equilibrium (PA). (Online version in color.)

Because of the absence of diffusion in the solid phases under the GS approximation, the average solid composition of the entire system at temperature ${}^{k}T$ is directly computed by adding the fraction of solid formed during cooling of the subsystem to the already existing solid using:

$$ {}^{k}_{GS}\overline{x}_i^{p_j\neq 1} = \left({}^{(k-1)}N^{p_j\neq 1}\ {}^{(k-1)}\overline{x}_i^{p_j\neq 1} + {}^{k}_{EQ}N^{p_j\neq 1}\ {}^{k}_{EQ}x_i^{p_j\neq 1} \right) / \left({}^{(k-1)}N^{p_j\neq 1} + {}^{k}_{EQ}N^{p_j\neq 1} \right) \quad j=[1,n^p],\ i=[1,n^s] \quad \text{... (4)} $$

The new total fraction of the solid phases for the entire system is equal to:

$$ {}^{k}_{GS}N^{p_j\neq 1} = {}^{(k-1)}N^{p_j\neq 1} + {}^{k}_{EQ}N^{p_j\neq 1} \quad j=[1,n^p],\ i=[1,n^s] \quad \text{..... (5)} $$

Liquid fraction and composition are simply given by the equilibrium solution:

$$ {}^{k}_{GS}x_i^1 = {}^{k}_{EQ}x_i^1 \qquad i=[1,n^s] \quad \text{..... (6)} $$

$$ {}^{k}_{GS}N^1 = {}^{k}_{EQ}N^1 \quad \text{..... (7)} $$

3.3. Partial-equilibrium (PE) Approximation

The PE approximation is intended to be used for systems with large differences in the diffusivity of chemical elements. This is typically the case in steels containing interstitial elements with high diffusivity and substitutional elements with low diffusivity. It is seen as an extension of the GS approximation and was initially developed for simulation of the solidification paths in steels[3,4] where carbon is interstitial and diffuses rapidly compared to *e.g.*, substitutional chromium. To simplify the problem, carbon is the only interstitial element considered in this study. Mathematical formulation of PE first relies on equal average chemical potential of carbon in all phases, ${}^{k}_{PE}\overline{\mu}_C^{p_j}\left({}^{k}_{PE}\overline{x}_i^{p_j}\right)$. It also considers unchanged values for the average u-fractions of the substitutional elements defined by ${}^{k}_{PE}\overline{u}_{i\neq C}^{p_j} = {}^{k}_{PE}\overline{x}_{i\neq C}^{p_j} / \left(1-{}^{k}_{PE}\overline{x}_C^{p_j}\right)$ with respect to the values provided by the last GS step at temperature ${}^{k}T$ for each phase participating to equilibrium, ${}^{k}_{GS}\overline{u}_{i\neq C}^{p_j} = {}^{k}_{GS}\overline{x}_{i\neq C}^{p_j} / \left(1-{}^{k}_{GS}\overline{x}_C^{p_j}\right)$. These conditions are added the mass conservation of carbon and of all the substitutional elements over all participating phases considering the values provided by the last GS step at temperature ${}^{k}T$. Thus, PE is initialized from a GS calculation as shown in Fig. 1. The above four considerations translate into:

$$ {}^{k}_{PE}\overline{\mu}_C^{p_j}\left({}^{k}_{PE}\overline{x}_i^{p_j}\right) = {}_{PE}Cst \qquad p_j=\{s_1,s_2,\ldots,1\},\ j=[1,n^p],\ i=[1,n^s] \quad \text{.... (8)} $$

$$ {}^{k}_{PE}\overline{u}_{i\neq C}^{p_j} = {}^{k}_{GS}\overline{u}_{i\neq C}^{p_j} \quad p_j=\{s_1,s_2,\ldots,1\},\ j=[1,n^p],\ i=[1,n^s] \quad \text{... (9)} $$

$$ \sum_{j=1}^{n^p} {}^{k}_{PE}\overline{x}_C^{p_j}\ {}^{k}_{PE}N^{p_j} = \sum_{j=1}^{n^p} {}^{k}_{GS}\overline{x}_C^{p_j}\ {}^{k}_{GS}N^{p_j} \qquad p_j=\{s_1,s_2,\ldots,1\},\ j=[1,n^p] \quad \text{.... (10)} $$

$$ \sum_{i=1}^{n^s} {}^{k}_{PE}\overline{x}_{i\neq C}^{p_j}\ {}^{k}_{PE}N^{p_j} = \sum_{i=1}^{n^s} {}^{k}_{GS}\overline{x}_{i\neq C}^{p_j}\ {}^{k}_{GS}N^{p_j} \qquad p_j=\{s_1,s_2,\ldots,1\},\ j=[1,n^p],\ i=[1,n^s] \quad \text{..... (11)} $$

The number of unknowns is $(n^s+1)n^p+1$: $(n^s n^p)$ compositions, n^p phase fractions plus the constant ${}_{PE}Cst$. The number of equations is the same: n^p Eq. (8), $(n^s-1)n^p$ Eqs. (9), (10) plus n^p Eq. (11).

3.4. Para-equilibrium (PA) Approximation

On the basis of Hillert's idea,[8] the PA approximation was originally developed for a transformation taking place between solid phases with local equilibrium at the phase interface and frozen composition of substitutional elements. It permits to deal with solid phase transformation with the same u-fraction of substitutional elements and equality of chemical potential for instertitial elements. The condition on the interstitial element thus writes similarly as for the PE approximation with equal average chemical potentials among solid phases. This means that diffusion of interstitial elements is assumed very high, as for PE. For substitutional elements, condition is given on the summation of the product of the average chemical potential by the average u-fraction which is deduced from no driving force on the interface. A detailed derivation is given in Ref. 8). As stated before, it is chosen to consider a unique average u-fraction for each substitutional element in all the solid phases, ${}^{k}_{PE}\overline{u}_{i\neq C}^{p}$, $i=[1,n^s]$, its value being defined below. Finally, as for previous approximations, mass conservation of interstitial and substitutional elements over all solid phases must also be verified. Considering only carbon as the interstitial element, the following set of equations must thus be satisfied:

$$ {}^{k}_{PA}\overline{\mu}_C^{p_j}\left({}^{k}_{PA}\overline{x}_i^{p_j}\right) = {}_{PA}Cst1 \qquad p_j=\{s_1,s_2,\ldots\},\ j=[1,n^p],\ i=[1,n^s] \quad \text{.... (12)} $$

$$ \sum_{j=1}^{n^p} {}^{k}_{PA}\overline{u}_{i\neq C}^{p_j}\ {}^{k}_{PA}\overline{\mu}_{i\neq C}^{p_j}\left({}^{k}_{PA}\overline{x}_i^{p_j}\right) = {}_{PA}Cst2 \qquad p_j=\{s_1,s_2,\ldots\},\ j=[1,n^p],\ i=[1,n^s] \quad \text{.... (13)} $$

$$ {}^{k}_{PA}\overline{u}_{i\neq C}^{p_j} = {}^{k}_{PE}\overline{u}_{i\neq C}^{p} \quad p_j=\{s_1,s_2,\ldots\},\ j=[1,n^p],\ i=[1,n^s] \quad \text{..... (14)} $$

$$ \sum_{j=1}^{n^p} {}^{k}_{PA}\overline{x}_C^{p_j}\ {}^{k}_{PA}N^{p_j} = \sum_{j=1}^{n^p} {}^{k}_{PE}\overline{x}_C^{p_j}\ {}^{k}_{PE}N^{p_j} \qquad p_j=\{s_1,s_2,\ldots\},\ j=[1,n^p] \quad \text{..... (15)} $$

$$ \sum_{j=1}^{n^p}\sum_{i=1}^{n^s} {}^{k}_{PA}\overline{x}_{i\neq C}^{p_j}\ {}^{k}_{PA}N^{p_j} = \sum_{j=1}^{n^p}\sum_{i=1}^{n^s} {}^{k}_{PE}\overline{x}_{i\neq C}^{p_j}\ {}^{k}_{PE}N^{p_j} \qquad p_j=\{s_1,s_2,\ldots\},\ j=[1,n^p],\ i=[1,n^s] \quad \text{..... (16)} $$

The number of unknown compositions is $(n^s+1)\,n^p+2$: $(n^s n^p)$ compositions, n^p phase fractions plus the constants ${}_{PA}Cst1$ and ${}_{PA}Cst2$. The number of equations is the same: n^p Eq. (12), n^p Eq. (13), $n^p(n^s-1)$ Eqs. (14), (15) plus Eq. (16). Comparing the set of equations for PA to PE approximations, the main difference appears through Eq. (13). In the literature, application of the PA approximation is usually limited to 2 solid phases. The above PA set of equations can be solved for a subsystem made of two solid phases $p_j = \{s_1, s_2\}$ undergoing a peritectic reaction, in which case this subsystem is extracted from a previous PE cal-

culation, thus explaining the index PE used in the above Eqs. (14)–(16). For the u-fraction, it is to be noticed that an average value is defined, ${}^{k}_{PE}\overline{u}^{p}_{i\neq C} = {}^{k}_{PE}\overline{x}^{p}_{i\neq C} / \left(1 - {}^{k}_{PE}\overline{x}^{p}_{C}\right)$ where ${}^{k}_{PE}\overline{x}^{p}_{i\neq C} = \sum_{j=1}^{n^p} {}^{k}_{PE}\overline{x}^{p_j}_{i\neq C}\, {}^{k}_{PE}N^{p_j} / \sum_{j=1}^{n^p} {}^{k}_{PE}N^{p_j}$. It is thus computed for the subsystem of the phases considered under PA. It is also worth noticing that when only solid phases coexist, a simple lever rule calculation can be used for initialisation.

Thus, PA provides with a local equilibrium condition at an interface that differs from LR or full equilibrium. PA and LR applied at a solid/solid interface can thus be combined with the PE approximation used to deal with a solid/liquid interface.

3.5. Numerical Scheme

The numerical scheme for a general cooling sequence during solidification is shown in Fig. 1. Several combinations of the above approximations are possible:

- LR (*i.e.*, not GS in Fig. 1). It obviously corresponds to full thermodynamic equilibrium transformation paths and is valid from a temperature higher than the liquidus temperature up to room temperature.
- GS (*i.e.*, not PE in Fig. 1). As explained above, it implies that all interstitial and substitutional elements in all solid phases are frozen, not permitting the peritectic reaction to take place. Because such approximation is difficult to maintain up to low temperature, a critical fraction of liquid (0.0001%) is chosen to stop the transformation, below which the average composition of all phases is kept constant: ${}^{k}_{GS}\overline{x}_i^{p_j\neq 1} = {}^{(k-1)}x_i^{p_j\neq 1}$ and ${}^{k}_{GS}N^{p_j\neq 1} = {}^{(k-1)}N^{p_j\neq 1}$.
- PE (*i.e.*, not BCC↔FCC in Fig. 1). Considered alone, it considers full equilibrium of interstitials while substitutional elements are frozen. This does change the solidification path compared to GS, yet still not permitting the peritectic reaction to occur.
- PE + LR (*i.e.*, not PA in Fig. 1). It keeps the PE approximation while handling the peritectic reaction by using a simple LR approximation among the δ-BCC and γ-FCC solid phases.[5] Note that the γ-FCC to α-BCC solid state transformation is considered in such situation.
- PE + PA (*i.e.*, PA in Fig. 1). This configuration provides with the most advanced configuration where the δ-BCC to γ-FCC peritectic transformation and the γ-FCC to α-BCC solid state transformation are both considered under PA conditions.

4. Application to Steel Alloys and Discussion

4.1. Solidification Path for S-1

The measured liquidus temperature by means of DTA and the calculated one are shown in **Table 2**. The calculated value based on thermodynamic equilibrium is slightly lower than measurement. It is yet within the uncertainty of the experimental method. During DTA, the temperature difference between the alloy sample and a reference sample is recorded during heating to reveal the latent heat required during melting. Such a phase transformation, however, needs a driving force leading to overheating of the sample to transform the solid into liquid, and hence uncertainty in the determination of the liquidus temperature. The other possible reason is inherent to the precision of the thermocouples and the accuracy of the thermodynamic database. Overall, the comparison is thus considered as very good.

Figure 2(a) shows calculated solidification paths as a function of temperature for composition S-1. Figures 2(b) and 2(c) present the same results for smaller temperature intervals. Measurements data are added in Figs. 2(a) and 2(b). Differences clearly appear between computations using the various approximations. All simulations yet lie within the LR and GS curves. This was indeed expected since, in the absence of undercooling, LR and GS could be regarded as the two extreme thermodynamic limits with respect to solid state diffusion. Under LR, the total solid

Table 2. Liquidus temperature (°C) and onset temperature for the peritectic transformation (°C) deduced from DTA measurement and from the TCFE6 database[11] for alloy S-1 using various approximations.

Liquidus	1 515 ± 5	1 511.45				
Peritectic transformation	1 490 ± 5	1 485.8	1 485.5	1 485.25	1484.6	1 484.25
	DTA	LR	GS	PE	PE + LR	PE + PA

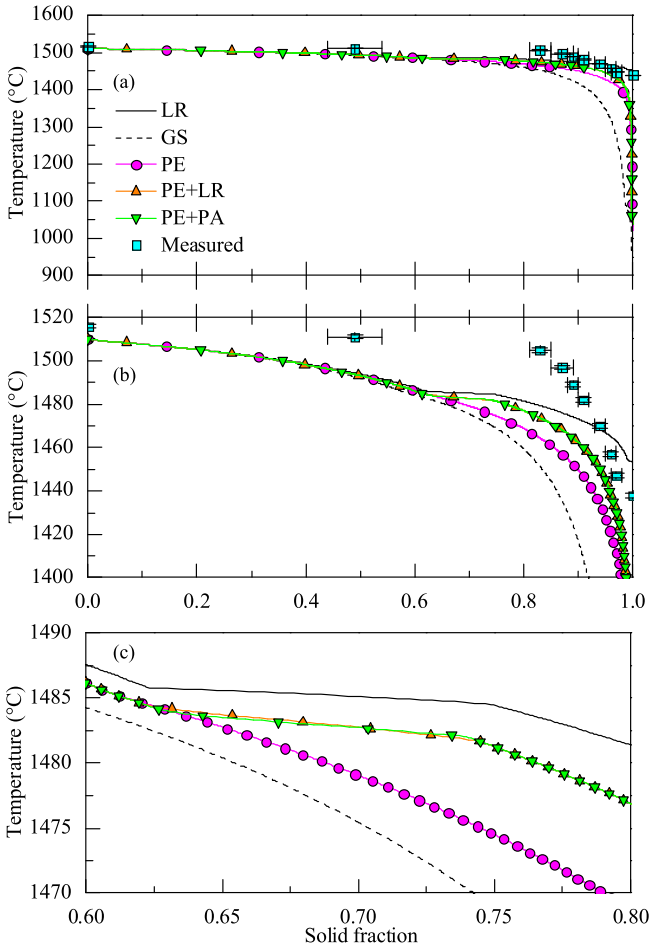

Fig. 2. Solidification paths displayed for (a) the maximum solidification interval deduced from the predictions, (b) the experimental range, and (c) around the peritectic reaction. Measurement data are added for comparison. Steel S-1 (Table 1), 5 microsegregation models. (Online version in color.)

fraction increases within the smallest temperature range, *i.e.* [1 510°C, 1 453°C], while it is the largest for GS, *i.e.* [1 510°C, 958°C]. This is a common finding for alloy solidification. In the absence of diffusion in the solid phases and with segregation of elements in the liquid, solidification proceeds up to low temperature and can lead to the formation of additional intermetallic phases.

Figure 2(b) provides with a temperature range that permits a better comparison with experimental results. It is clear from this graph that even the most favorable simulation, *i.e.* LR, significantly underestimates the fraction of solid up to more than 90%, *i.e.* from the liquidus temperature up to 1 470°C. In the present situation, the procedures for collecting the experimental data can certainly be discussed. During solidification in the Bridgman furnace, thermosolutal convection could take place that would lead to a non-uniform alloy composition in the quenched sample, thus modifying the solidification path. This is a well-known phenomenon in upward Bridgman configuration, often reported in the literature for similar experimental set-up or even during in-situ observation.[12] Furthermore, as stated before, solidification of the solid phases can continue during quenching, thus overestimating the fraction of solid prior to quenching. Of course the approximations of the simulations are also of prime importance, among which the kinetics of the microstructures. As previously stated for fusion, solidification proceeds with diffusion limited kinetics. With undercooling, the microstructure forms with a sudden burst of the solid fraction just behind its growing interface, *i.e.* from its working temperature. Such sudden increase is reported by the observations, the fraction of solid increasing from 0 to more than 80% from the liquidus temperature, 1 515 ± 5°C, to 1 505 ± 5°C, *i.e.* within a 10°C interval. Similar observation was reported in the literature. It was initially explained by considerations of the solute mass balance at the growth fronts[13] or more phenomenological analyses.[14] More sophisticated models were developed for this purpose, all taking into account growth undercooling of the microstructure due to limited diffusion in the liquid phase.[15] The analysis was made available in the presence of combined dendritic, peritectic and eutectic reactions.[16] However, it is still limited when considering multicomponent alloys.

A further magnification is provided in Fig. 2(c) around the peritectic reaction, *i.e.* the transformation of δ-BCC to γ-FCC. At around 1 485°C, all the curves present a slope change due to the formation of the peritectic γ-FCC phase. This is better seen in **Fig. 3** where the C and Mn composition of δ-BCC to γ-FCC are drawn for the same temperature interval as Fig. 2(c). Under LR, the δ-BCC to γ-FCC transformation starts at 1 485.5°C and end at 1 484.5°C. In the absence of diffusion in the solid phase (GS), the δ-BCC fraction is frozen at its composition up to room temperature. The set of conditions and equations for PE is shown to also freeze δ-BCC and its Mn composition while the C composition continues to evolve. However, it is not satisfying since peritectic reaction has to take place. For this reason, the PE + LR and PE + PA were computed. The difference between these two solidification paths can only be seen in Fig. 2(c). The present PE + PA transformation path differs very little from the original PE + LR treatment proposed by Chen *et al.*[5] One can yet mention the difference observed in Fig. 3. During the peritectic transformation under LR, PE + LR and PE + PA, the carbon composition decreases in both phases. In contrast, the manganese composition increases in both phases in case of LR and PE + PA, while it slightly decreases in case of PE + LR.

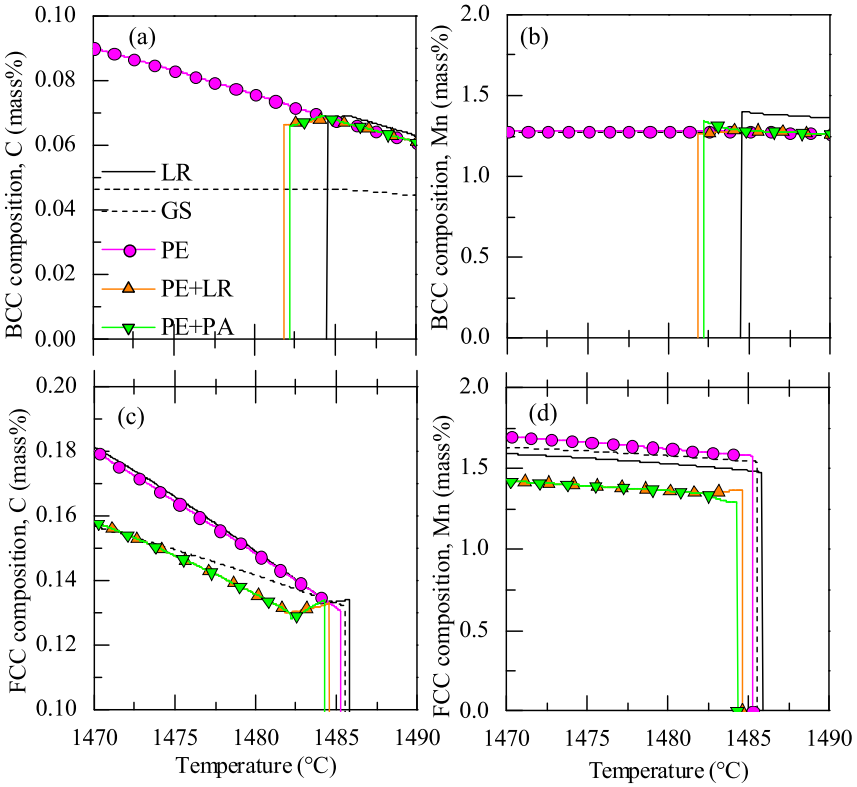

Fig. 3. Phase composition within the temperature range of the peritectic transformation for (left) carbon and (right) manganese in (top) BCC and (bottom) FCC phases. Steel S-1 (Table 1), 5 microsegregation models. (Online version in color.)

4.2. Transformation Path for S-2

In order to better analyze the PE + LR and PE + PA approximations, experimental and numerical studies were conducted on alloy composition S-2 given in Table 1. **Figure 4** shows the evolutions of BCC and FCC fractions when cooling the alloy from the liquid state up to room temperature. These evolutions are also given for intermetallics MnS, M_3P, and other phases in **Fig. 5**. Similar observations are found as for alloy S-1 upon primary δ-BCC solidification and the δ-BCC to γ-FCC peritectic transformation for the five approximations considered, *i.e.* δ-BCC is frozen below the peritectic temperature under GS and PE. Note in Figs. 5(a) and 5(b) the large differences found between the precipitation temperatures of the MnS and M_3P phases, respectively. The GS approximation predicts the lowest precipitation temperatures for these phases. It also reveals precipitation of Cementite and Graphite from the melt at around 950°C (Fig. 5(c)). Such large solidification interval is not likely to be achieved and this is clearly a limitation of the GS approximation. The PEs approximations also predict formation of the MnS and M_3P phases slightly above 1 000°C. At lower temperature, all phase fractions are locked under GS and PE. As stated before, this is coherent with solute mass balance analysis of frozen substitutional

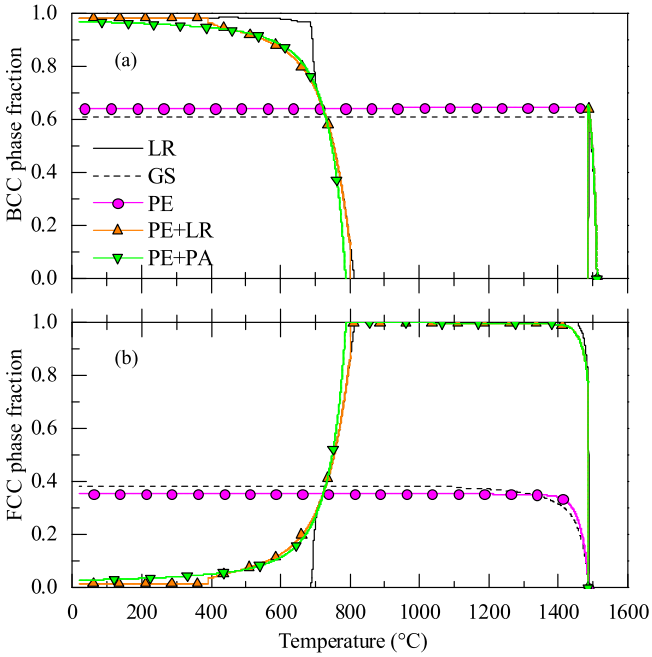

Fig. 4. Mass fraction of phases as a function of temperature for (top) δ-BCC and (bottom) γ-FCC. Steel S-2 (Table 1), 5 microsegregation models. (Online version in color.)

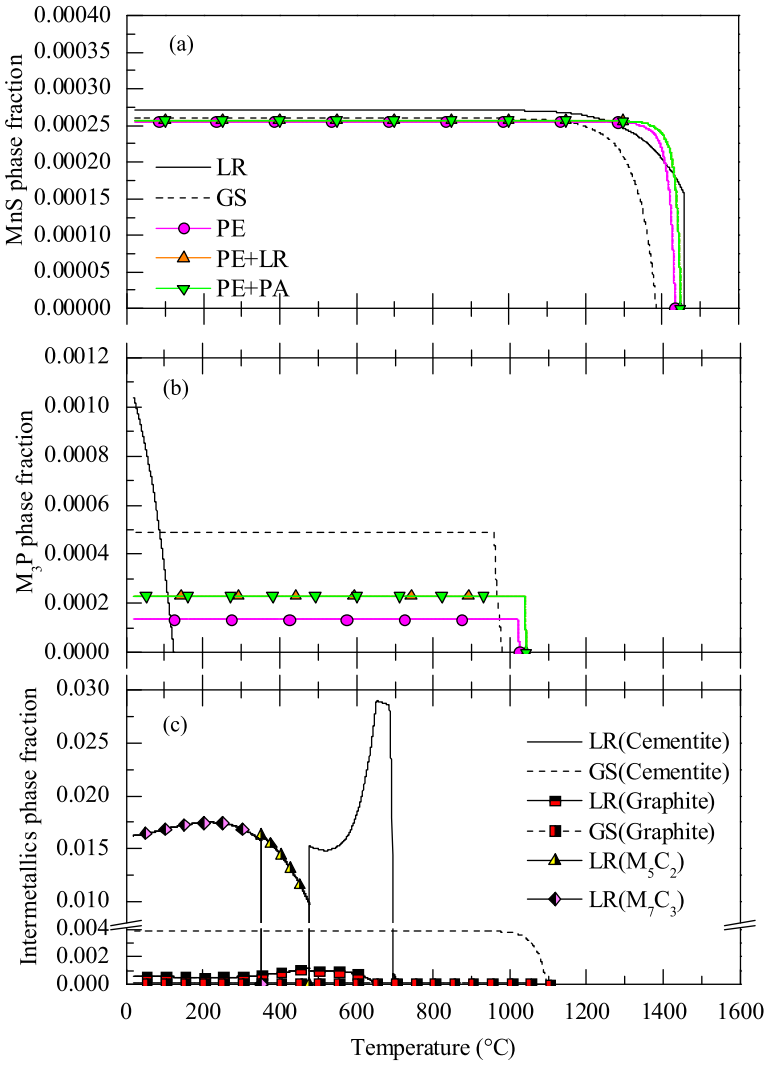

Fig. 5. Mass fraction of phases as a function of temperature for (top) MnS, (middle) M_3P and (bottom) other intermetallics. Steel S-2 (Table 1), 5 microsegregation models. (Online version in color.)

elements at phase interfaces.

When considering LR, PE + LR, and PE + PA, solid-solid interfaces are activated and phases can continue to evolve up to room temperature. These phase transformation paths are obviously more realistic since α-BCC (or α-ferrite) is classically found at room temperature. Figure 4 shows that the transformation starts below 800°C. Differences yet clearly appear on the curves, with LR prediction abruptly departing from the PE + LR and PE + PA curves at around 750°C with the transformation of γ-FCC into α-BCC. This behavior of the LR transformation path is only realistic if substitutional elements can rapidly equilibrate, leading to a full disappearance of γ-FCC. It also leads to the formation of Cementite, Graphite, M_5C_2 and M_7C_3 phases at lower temperatures as shown in Fig. 5(c). On the contrary, PE + LR and PE + PA show a continuous transformation of γ-FCC into α-BCC (Fig. 4) and no additional phases other than MnS and M_3P. The latter paths are thus more realistic.

Figure 6 presents the BCC and FCC compositions in C and Mn predicted by the five approximations. Obviously, C is only frozen after solidification under GS while Mn is frozen for GS, PE and PE + PA. For LR and PE + LR, Mn composition continues to change after solidification. Consequently, Mn is fully transferred from δ-BCC to γ-FCC at room temperature, while austenite is not likely to be present anymore for this alloy. In case of PE + PA, the Mn content is maintained close to the nominal composition (1.47 mass%) in both FCC and BCC phases.

For a better assertion of the most meaningful combination of the thermodynamic approximations, EPMA measurements conducted on the S-2 composition is presented in **Fig. 7**. It presents the predicted average Mn composition at 20°C (left) and the interfacial Mn composition obtained during GS step denoted as $_{EQ}^{k}x_{Mn}^{p_j\neq 1}$ in Fig. 1 (right). One should

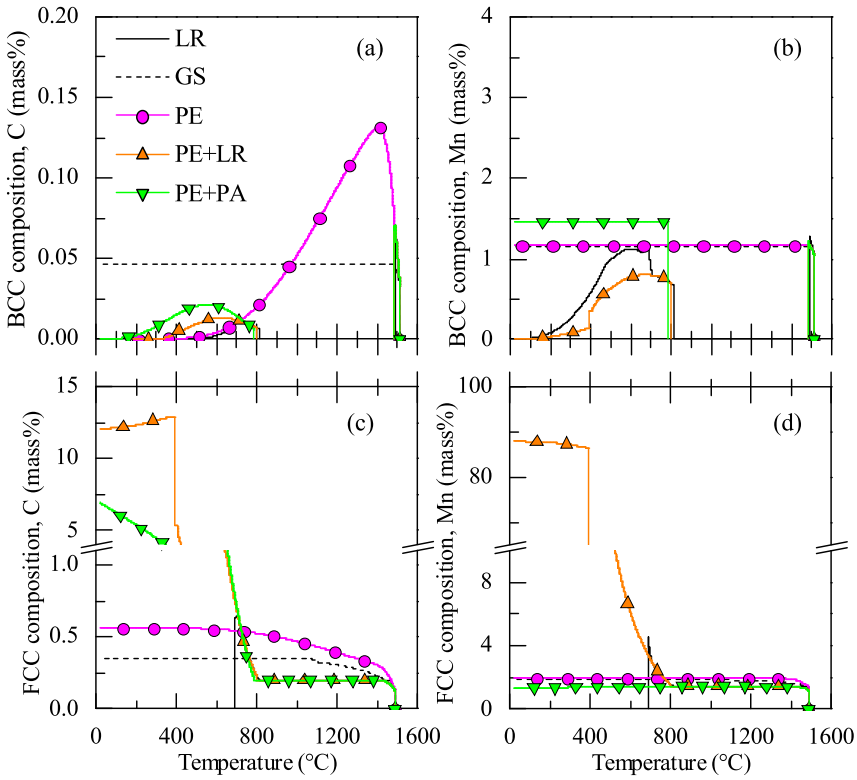

Fig. 6. Phase composition as a function of temperature for (left) carbon and (right) manganese in (top) BCC and (bottom) FCC phases. Steel S-2 (Table 1), 5 microsegregation models. (Online version in color.)

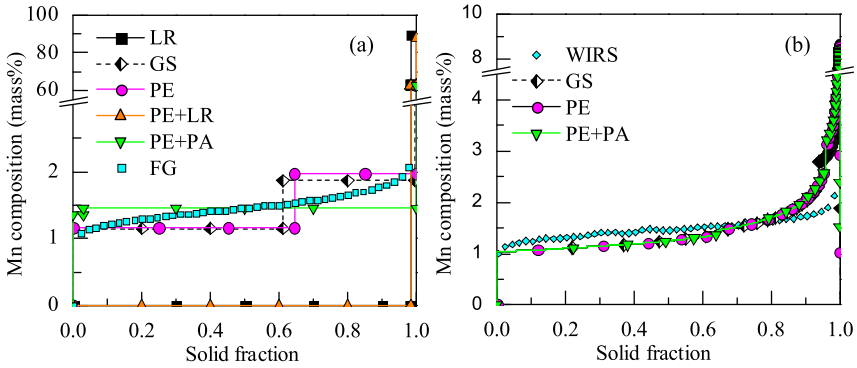

Fig. 7. Average Mn composition as a function of the mass fraction of solid with (left) FG and (right) WIRS sorting methods. Steel S-2 (Table 1), 5 microsegregation models. Parameters for the WIRS analysis are given in **Table 3**. (Online version in color.)

Table 3. Data for WIRS (mass%). σ is uncertainty, estimated as the difference between nominal composition and average composition of EPMA measurements.

	Mn	S	P
Min	0	0	0
σ	0.026	0.004	0.004

notice that the sample analyzed contains MnS, thus explaining the rapid increase of Mn content in the composition profiles for solid fraction above 0.95. The GS, PE and PE + PA approximations are found to provide better agreement with the measurements, using both the FG and WIRS sorting methods, *i.e*. when Mn diffusion is frozen. A clear change in the composition profile is yet predicted under GS, PE and PE + PA, when the solid fraction reaches around 0.65. It is due to the δ-BCC to γ-FCC transformation. According to previous considerations, the overall best agreement is thus found for the combination of PE + PA approximations.

5. Conclusion

(1) Combination of the partial- and para- equilibrium (PE + PA) thermodynamic approximations is proposed for the study of phase transformations in steels, from the liquid state to room temperature.

(2) Calculated solidification paths for multi-component alloys are discussed with respect to the peritectic transformation. It is found that, in case of PE + PA, the solidification path does not differ significantly from the lever rule (LR) and from the combination of the partial equilibrium plus lever rule (PE + LR) approximations.

(3) Differences with experimental results are discussed based on analyses of a sample processed by Bridgman solidification, showing the need for more accurate experimental results and removal of several modeling hypotheses (absence of microstructures kinetics and no treatment of limited diffusion in all phases).

(4) Regarding the solid state phase transformations, PE + PA is found to provide the most realistic composition profile of substitutional elements and evolution of the phase fractions. PE + PA is therefore recommended as the standard set of thermodynamic approximations to be used for the study of phase transformations in multicomponent steels.

Acknowledgments

This work has been supported by Nippon Steel & Sumitomo Metal Corporation (Tokyo, Japan) in a collaboration project with ArcelorMittal Maizières Research (Maizières-lès-Metz, France).

REFERENCES

1) G. H. Gulliver: *J. Inst. Met.*, **9** (1913), 120.
2) E. Scheil: *Z. Metallkd.*, **34** (1942), 70.
3) Q. Chen and B. Sundman: *Mater. Trans.*, **43** (2002), 551.
4) H. Zhang, K. Nakajima, C. A. Gandin and J. He: *ISIJ Int.*, **53** (2013), 493.
5) Q. Chen, A. Engstrom, X.-G. Lu and B. Sundman: MCWASP-XI, ed. by Ch.-A. Gandin and M. Bellet, TMS, Warrendale, PA, (2006), 529.
6) Thermo-Calc TCCS Mnuals, Thermo-Calc Sftware AB, Stockholm, Sweden, (2013).
7) P. Shi: TCS steels/Fe-alloys Dtabase, V6.0, Thermo-Calc Software AB, Stockholm, Sweden, (2008).
8) M. Hillert: Phase Equilibria, Phase Diagrams and Phase Transformations, Cambridge University, UK, (1998), 358.
9) W. Kurz and D. J. Fisher: Fundamentals of Solidification, Trans Tech Publications Ltd, Switzerland, (1998), 7.
10) J. A. Dantzig and M. Rappaz: Solidification, EPFL Press, Lausanne, Switzerland, (2009), 17.
11) M. Ganesan and P. D. Lee: *Mater. Trans. A*, **36** (2005), 2191.
12) A. Bogno, H. Nguyen-Thi, G. Reinhart, B. Billia and J. Baruchel: *Acta Mater.*, **61** (2013), 1303.
13) J. A. Sarreal and G. J. Abbaschian: *Mater. Trans. A*, **17** (1986), 2063.
14) B. Giovanola and W. Kurz: *Mater. Trans. A*, **21** (1990), 260.
15) C. Y. Wang and C. Beckermann: *Mater. Sci. Eng. A*, **171** (1993), 199.
16) D. Tourret, Ch.-A. Gandin, T. Volkmann and D. M. Herlach: *Acta Mater.*, **59** (2011), 4665.

Chapter III

Study of Hot Tearing During Steel Solidification Through Ingot Punching Test and Its Numerical Simulation

Takao KOSHIKAWA, Michel BELLET, Charles-André GANDIN, Hideaki YAMAMURA and Manuel BOBADILLA

DOI: 10.1007/s11661-016-3564-x

Pages: 42 to 58 in this thesis

Study of Hot Tearing During Steel Solidification Through Ingot Punching Test and Its Numerical Simulation

TAKAO KOSHIKAWA, MICHEL BELLET, CHARLES-ANDRÉ GANDIN, HIDEAKI YAMAMURA, and MANUEL BOBADILLA

Experimental and numerical studies of hot tearing formation in steel are reported. On the one hand, an ingot punching test is presented. It consists in the application of a deformation at the surface of a solidifying 450 kg steel ingot. The experimental parameters are the displacement of the pressing tool, together with its velocity, leading to variations of a global strain rate. On the other hand, three-dimensional finite element thermomechanical modeling of the test is used. The time evolution of the strain tensor serves to compute an index to evaluate the susceptibility to create hot tears. It is based on the integration of a hot tearing criterion (HTC) that compares the local accumulation of strain with the expression of a critical value proposed in the literature. The main variable of the criterion is the brittleness temperature range (BTR) that refers to the solidification interval during which strain accumulates and creates hot cracks or tears. Detailed comparison of the simulation results with the measurements reveals the importance of the BTR for the prediction as well as excellent capabilities of the HTC to predict the formation of hot tears.

DOI: 10.1007/s11661-016-3564-x

I. INTRODUCTION

THE present paper focuses on a major defect encountered during secondary cooling in steel Continuous Casting (CC) known as hot tearing. Also named hot cracking or solidification cracking, this defect takes place deep in the mushy zone in regions close to the end of solidification, typically exceeding 90 pct of solid. A comprehensive description of the physical phenomena involved in hot tearing is found in Reference 1. The liquid phase remaining at the late stage of solidification takes the form of thin interdendritic and intergranular films that cannot resist possible mechanical deformations. These are tensile stresses arising from external solicitations exerted by the immediate environment, for instance solidification shrinkage, thermal contraction of the neighboring regions, or boundary conditions restraining the product. Even low local deformations cannot be compensated by liquid feeding because of the extremely low permeability of the solid network at such high solid fractions. This leads to the rupture of the remaining liquid films, thus creating cracks. The material appears particularly vulnerable in a critical range of solid fraction, which is known as the Brittleness Temperature Range (BTR). Processing by CC leads to hot tearing formation during the bending or unbending of the strand, or as a consequence of bulging of the shell between support rolls under the effect of metallostatic pressure.

Locally and at small scale, various parameters influence the occurrence of hot tearing. The first of them is the chemical composition of the alloy. The larger the solidification interval is, the higher is its hot tearing sensitivity. Indeed, fragility strongly depends on the solidification path through the kinetic of liquid transformation near the end of solidification. In steels, some chemical elements such as sulfur, phosphorus or boron tend to increase the hot tearing sensitivity as they increase the solidification interval and thus decrease the solidus temperature.[2] Second, the microstructure also influences the hot tearing sensitivity. A fine microstructure decreases the sensitivity due to a better adaptation to the deformation: gliding at grain boundaries can accommodate small strains at low strain rates.[3] Accordingly, tearing resistance of an equiaxed structure is better than that of a columnar structure.[4] Note that the microstructure also determines the permeability and hence the compensation of strains by liquid feeding. Thirdly, wetting of the solid phase by the liquid phase depends on both temperature and liquid composition: a

TAKAO KOSHIKAWA, Manager, is with Nippon Steel & Sumitomo Metal Corporation Oita Works, Equipment division, Oita, Japan, and also Ph.D. Student at MINES ParisTech, Centre de Mise en Forme des Matériaux (CEMEF), UMR CNRS 7635, 06904 Sophia Antipolis, France. Contact e-mail: koshikawa.4eb.takao@jp.nssmc.com MICHEL BELLET, Professor and Group Leader, and CHARLES-ANDRÉ GANDIN, CNRS Researcher and Group Leader, are with MINES ParisTech, CEMEF UMR CNRS 7635. HIDEAKI YAMAMURA, formerly Chief Researcher with Nippon Steel & Sumitomo Metal Corporation, Steelmaking R&D Division, is now Secretary General with The Japan Institute of Metals and Materials, 1-14-32, Ichibancho, Aoba-ku, Sendai 980-8544, Japan. MANUEL BOBADILLA, Group Manager, is with ArcelorMittal Maizières, Research and Development, BP 30320, 57283 Maizières-lès-Metz, France.

Manuscript submitted January 3, 2016.

Published online: 06 June 2016

low wettability will promote the formation of solid bridges between grains which will help to resist tensions.[5] At last, the local thermomechanical behavior plays an important role in the appearance of hot tearing, itself being dependent on microstructure.

Recently, several researches focused on hot tearing phenomena. They can be divided into two groups; micro- and macroscopic scale studies. The last decade has seen a significant development of numerical simulations directly operated at the scale of a Representative Elementary Volume (REV) of the mushy material, in view of encompassing most of the small-scale physical phenomena mentioned above. Phillion *et al.*[6] showed the influence of microstructural features on tensile deformation of a REV of semi-solid aluminum alloy. Sistaninia *et al.*[7] have developed a numerical simulation using a discrete element method in order to account for the strain inhomogeneity in the mushy zone due to crack initiation and propagation, in other words, direct simulation of hot tearing. Zaragoci *et al.*[8] considered a domain of few cubic millimeters deduced from *in situ* X-ray tomography of a tensile test in an Al-Cu sample maintained in the mushy state. A finite element discretization of the 3D domain using the level set method and adaptive mesh refinement was conducted to accurately separate liquid films and grains. The liquid flow and grain deformation were calculated, intrinsic properties of the phases obeying a viscoplastic constitutive equation. However, in those recent works,[6–8] only fragments of the different physical phenomena taking part in hot tearing were accounted for. It can be thought that such small-scale models will develop in the future, integrating more and more relevant physical features, and thus will become useful tools for a better fundamental understanding of hot tearing. But upscaling of such models to deduce rules that can be applied at the processing scale, such as in continuous casting, will require time due to their computational cost and actual approximations of the physical phenomena. Therefore, it is necessary to focus on more macroscopic analysis methods to study hot tearing. Those constitute the second group of researches mentioned previously, if one is targeting process scale applications.

In the literature, lots of studies have proposed hot tearing criteria based on thermal considerations,[9] solid mechanics[10–15] or solid and fluid mechanics.[16] Bellet *et al.*[15] have evaluated four of those hot tearing criteria for steels[9,10,14,16] by means of constrained shrinkage tests and ingot bending tests. Systematic numerical simulation of the tests was conducted with the finite element package THERCAST® equipped with the different macroscopic criteria. The authors concluded that the only criterion able to show a qualitative agreement with the experimental tests was the strain-based criterion proposed by Won *et al.*[14] They proposed an enriched expression to reach quantitative agreement.[15] In addition, Pierer *et al.*[3] evaluated, by use of submerged split chill tensile tests, a stress-based criterion,[11] a strain-based criterion,[14] a criterion based on strain rate and including liquid feeding consideration,[16] and a criterion based on the sole BTR value.[9] The authors found that only the stress-based criterion and the strain-based criterion had good capability for predicting hot tearing. As a consequence, in the framework of the present study, we will essentially focus on hot tearing criteria based on critical strain.

Section II of this paper will consist of a review of macroscopic strain-based criteria and of their characterization through ingot bending or punching tests, as it will be shown that such tests are well suited to reproduce the context of continuous casting. Section III will present the ingot punching test developed in the framework of the present study. In Section IV, the thermomechanical finite element model will be presented including the effective implementation of the selected hot tearing criterion in the computation code THERCAST®. Results of the numerical simulation of the punching tests and their comparison to experimental measurements will be presented and discussed in Section V.

II. A REVIEW OF STRAIN-BASED CRITERIA AND ASSOCIATED CHARACTERIZATION THROUGH INGOT BENDING OR PRESSING TESTS

As initially suggested by Yamanaka *et al.*,[13] the basic expression to quantify the risk for the occurrence of hot tearing due to accumulation of strain is written as follows:

$$F_{HT} = \varepsilon_{BTR} - \varepsilon_c, \qquad [1]$$

where ε_{BTR} is the local cumulated strain for a REV in the mushy zone during its cooling within a range of solid fraction. The second strain, ε_c, is the critical strain at which cracks form. These quantities will be detailed and discussed hereafter. From Eq. [1], a positive value of the criterion function F_{HT} interprets as the onset of cracks as the cumulated strain locally exceeds the critical strain. Note that if one assumes a direct relationship between temperature and fraction of solid, the range of solid fraction transforms into a temperature interval called the brittleness temperature range (BTR).

For a given alloy, the critical strain value has to be established by experimental testing. The latter should be representative of the conditions of the solidification process for which the criterion is used. With this respect, the ingot bending or punching tests developed since the late 70s by steelmakers to estimate the CC-process viability are good candidates. Such tests have been developed by several authors.[2,17–21] They consist in bending, punching, or pressing the solidifying shell of an ingot during its solidification by means of a punch moved perpendicularly to the shell plane (or surface of the ingot), *i.e.*, along the dendritic growth direction when solidification proceeds directionally away from the mold walls. The size of the ingot and the control of the bending/punching conditions have to represent the solicitations undergone by the solid shell during CC when it passes through the support rolls. Note that in

CC, the alloy also endures the metallostatic pressure which induces bulging between each roll stand. Narita *et al.*[20] performed ingot punching tests on 72 kg steel ingots. This was done by moving a punch through an opening window designed in the mold. The displacement and the velocity of the punch were recorded during the tests, but the punching force was not measured. Another example is provided by Wintz *et al.*[2] who developed a three-point bending test performed on 300 kg steel ingots ($1200 \times 150 \times 250$ mm^3) during their solidification in a thin 6-mm-thick mold made of mild steel. The whole set—ingot plus mold—was bent by a cylindrical punch (maximum force 450 kN), the velocity of which was maintained constant in the range from 0.1 to 5.5 mm s^{-1} during a short time. The surface temperature of the mold was measured by a pyrometer. The knowledge of the solidified thickness at the bending instant was obtained by a sulfur print made on a cross section of a test-ingot in which the remaining liquid pool was on purpose and instantly enriched in sulfur at the instant of bending.

In this type of experiments, authors evaluated the applied deformation close to the solidification front by some simple bending formulae. The applied strain rate was directly deduced by dividing the total displacement imposed to the punch by the duration of its travel. It is worth noting that those estimations do not take into account neither the three-dimensional character of the test nor the fact that highly non-uniform thermal gradients prevail through the shell thickness, inducing a gradient in the material strength. Therefore, the quantitative results deduced from these tests should be considered cautiously. However, from a qualitative point of view, results clearly demonstrate that the first-order variable for crack occurrence is strain. Strain rate appears as a second-order parameter, as the critical strain depends on strain rate (the higher the strain rate, the smaller the critical strain).

Nagata *et al.*[12] summarized lots of experimental results conducted on steels and draw the conclusion that the critical strain is related to the strain rate, $\dot{\varepsilon}$, by a power law. The slope of the log-form of this power law is a constant whatever the steel grade. The corresponding relationship thus is written as follows:

$$\varepsilon_c = A\dot{\varepsilon}^{-m^*}, \qquad [2]$$

where m^* is a constant while A depends on steel grades (chemical composition). In addition, the authors introduced the concept of poor ductility zone in the direction of the ingot thickness, the extent of which is denoted η. Poor ductility is considered by the authors between the solidus temperature T_S and a lower temperature called "Zero Ductility Temperature" T_{ZD}. This should not be seen as being contradictory to the definition of the BTR given above. Indeed, this may express the effect of intergranular coalescence. As demonstrated by Rappaz *et al.*[22] and illustrated by Wang *et al.*,[23] stable liquid films could still cover grain boundaries to a lower temperature than the solidus temperature. Thus, in their paper, Nagata *et al.* proposed an expression of T_{ZD}, or equivalently of the coalescence undercooling, as a function of the carbon, phosphorus, and sulfur content.[12] Taking into account the non-linear temperature profile through the ingot shell (non-constant temperature gradient), the expression proposed for η is

$$\eta = d\left[1 - \left(\frac{T_{ZD} - T_{surf}}{T_S - T_{surf}}\right)^{1.291}\right], \qquad [3]$$

where d is the thickness of solidified shell and T_{surf} is the surface temperature. It is worth noticing that η can equivalently be expressed by the following formula:

$$\eta = \frac{T_S - T_{ZD}}{\|\nabla T\|_\eta}, \qquad [4]$$

which involves the local temperature gradient $\|\nabla T\|_\eta$ within the poor ductility zone. Nagata *et al.* noticed that the critical strain also obeys the following expression[12]:

$$\varepsilon_c = C\eta^{-n^*}, \qquad [5]$$

where C and n^* are constants with positive values. Interpretation is that the smaller the poor ductility zone is, the larger is the critical strain required to form cracks (that is the smaller is the risk of hot tearing). Finally, in line with Eqs. [2] and [5], and on the basis of a compilation of several ingot bending experiments, the expression of the critical strain, as suggested by Nagata *et al.*, is written as follows[12]:

$$\varepsilon_c = \frac{\phi}{\eta^{n^*}}\left(\frac{\dot{\varepsilon}}{3 \times 10^{-4}}\right)^{-m^*} \qquad [6]$$

where $m^* = 0.167$ and parameters ϕ and n^* are as follows:

$$\begin{cases} \text{If } 1 \text{ mm} < \eta < 3 \text{ mm}, & \text{then } \phi = 0.0602 \text{ and } n^* = 2.13 \\ \text{If } 3 \text{ mm} < \eta, & \text{then } \phi = 0.0077 \text{ and } n^* = 0.258 \end{cases} \qquad [7]$$

Won *et al.*[14] proposed a similar expression. But rather than using the poor ductility extent η, which requires the knowledge of both the surface temperature T_{surf} and the solidified shell thickness d, as in Eqs. [3] and [6], they preferred to use directly the BTR value. The proposed expression for the critical strain is then

$$\varepsilon_c = \frac{\varphi}{\dot{\varepsilon}^{m^*}(\Delta T_{BTR})^{n^*}}, \qquad [8]$$

where ΔT_{BTR} is the extent of the BTR in Kelvin and φ, m^*, and n^* are parameters. Through the analysis of many experimental data,[18,20,24,25] the authors identified constant values for those three parameters: $\varphi = 0.02821$, $m^* = 0.3131$, $n^* = 0.8638$. They also mention that ΔT_{BTR} should be calculated with a non-equilibrium microsegregation analysis, taking into account the steel composition and the cooling rate. Bellet *et al.*[15] conducted a similar discussion, showing the strong

Table I. Compositions and Experimental Conditions

	Composition (Mass Pct)									
	C	Si	Mn	P	S	Al	Mold Removal (s)	Punching Start (s)	Displacement (mm)	Velocity (mm s^{-1})
Target	0.21	0.24	1.64	0.032	0.007	0.090	—	—	—	—
N-2	0.20	0.20	1.47	0.020	0.010	0.038	450	574	6	2.0
N-3	0.19	0.24	1.50	0.022	0.010	0.064	457	517	6	1.0
N-4	0.19	0.21	1.49	0.021	0.010	0.064	300	499	6	0.5
N-5	0.19	0.21	1.50	0.020	0.010	0.041	321	510	6	0.25
N-6	0.20	0.21	1.48	0.021	0.010	0.055	340	510	3	0.25

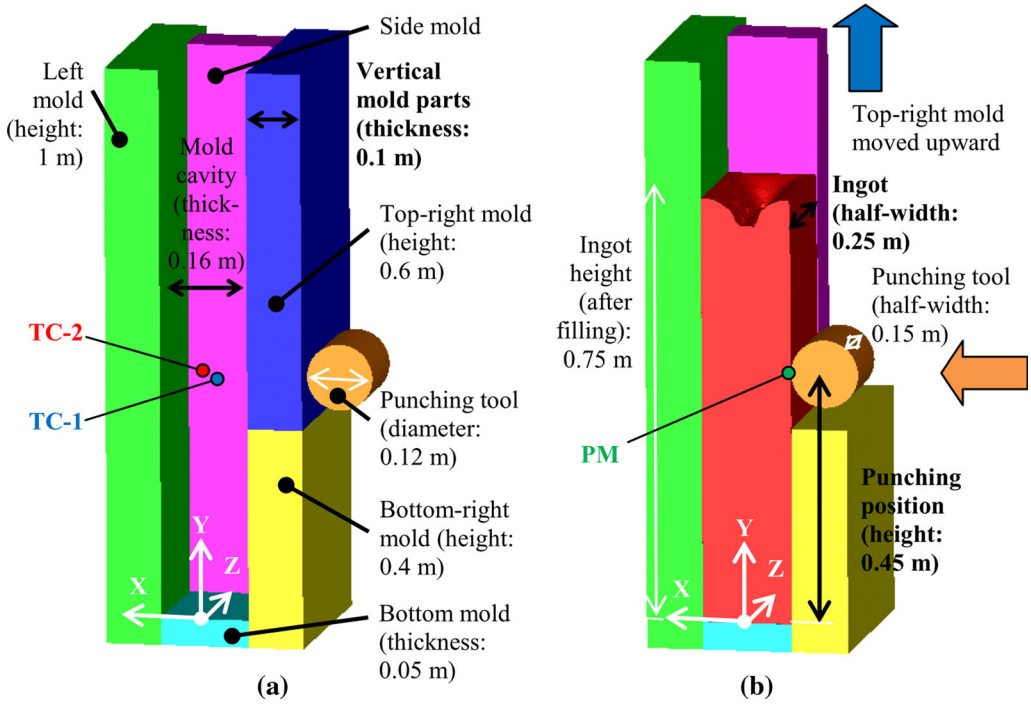

Fig. 1—Schematic of half of the hot tearing experiment setup developed at Nippon Steel & Sumitomo Metal Corporation showing configuration (*a*) prior to the filling stage and (*b*) at the onset of the punching stage when filling, partial solidification with the mold configuration shown in (a), removal of the top-right mold and displacement of the cylindrical punching tool to come into contact with the ingot. The coordinate system is defined in (a). The Y = 0 m plane is defined by the top surface of the bottom mold part, also defining the lowest ingot surface in (b). The Y-axis, opposite to the gravity vector, is directed toward the top of the ingot at mid-width and mid-thickness. The X-axis is directed toward the fixed left-mold surface. Thermocouples, TC-1 and TC-2, are located at (X, Y, Z) positions (0, 0.43, 0.06) m and (0.02, 0.43, 0.16) m, respectively. As schematized, pyrometer measurement (PM) is performed around the punched surface of the ingot, before and after punching.

dependence of the effective value of the critical strain, ε_c, with respect to the microsegregation model used for the determination of ΔT_{BTR}. Accordingly, and in line with Won *et al.*,[14] they proposed a new expression for the critical strain, based on a BTR value calculated with a microsegregation model in equilibrium conditions, but with correction terms expressing the effective extent of the brittleness domain especially due to sulfur and phosphorus. This model was validated against the experimental results of Wintz *et al.*[2]

In the present study, a strain-based criterion—hereafter named WYSO from the initials of its authors—will be considered with the shape of Eq. [8], the BTR extent being calculated by means of different microsegregation models presented in the literature.[28] The latter point will be detailed and discussed in Section V.

III. INGOT PUNCHING TEST

The present punch press test has been designed and operated by Nippon Steel and Sumitomo Metal Corporation in the R&D Centre of Futtsu, Japan. Steel grade for the present study is shown in Table I. A schematic of the test is shown in Figure 1. It has been designed to mimic the thermomechanical solicitations taking place during CC processing of steel, for instance, with respect to the evolution of the cooling rate and deformation. The procedure of the experiments was as follows: the molten metal was prepared in an electric ladle furnace and the temperature was maintained at 1913 K (1640 °C), *i.e.*, 129 K (129 °C) above the liquidus temperature. The molten metal was poured into the mold from the top through a tundish. The filling duration was about

70 seconds during which the temperature of the molten metal started decreasing due to heat exchanges with the tundish and with the mold. After filling, powder was added at the top of the ingot to limit heat exchanges with the air. The size of the ingot was 0.75 m height, 0.5 m width, and 0.16 m thick. Its mass was approximately 450 kg. In practice, a thermal insulator whose thickness was 5 mm covered the bottom part of the inner mold walls from the base of the ingot and up to 0.2 m height. This was required to avoid molten metal sticking and to make demolding easier. At a precise time after filling, the upper part of one of the two largest ingot surfaces (top-right mold in Figure 1) was moved upward. The lateral surface of the ingot was then in direct contact with the air. Note in Figure 1 that this side of the mold is made of two parts positioned one on top of the other. The bottom part could thus be kept at the same place when the top part was removed. A punching tool was then put into contact with the lateral vertical free surface of the ingot. It consists of a horizontal 0.12-m-diameter and 0.3-m-long cylinder with length centered on the main vertical face of the ingot and with its longitudinal axis aligned with the Z direction at height 0.45 m from the bottom of the ingot. The tool velocity and displacement are controlled by means of a hydraulic system and recorded during the test. The reaction force is also measured using the time evolution of the hydraulic system pressure. The test conditions referred to as N-2 to N-6 are summarized in Table I, together with measured nominal compositions in the ladle before filling. Note that a unique alloy composition was targeted for the experimental results reported hereafter. To know temperature evolution during the test, type-B thermocouples labeled TC-1 and TC-2 in Figure 1 were positioned in the ingot. For that purpose, two horizontal holes were created in the fixed large face of the mold (at left in Figure 1). Thermocouples were inserted into these holes from outside. They were positioned in the mold cavity at desired location. The holes' diameter was 5.5 mm. For sealing purpose, thermal insulator was put into the holes after setting thermocouples. In addition, type-K thermocouples were placed in the fixed large face of the mold in trial N-4. The ingot surface temperature was also measured with a pyrometer, labeled PM in Figure 1, in trial N-4 before and after deformation when the top-right mold was removed.

After completion of casting and cooling to room temperature, the ingot was cut and appropriate etching was conducted to investigate hot tearing occurrence considering its intensity and locations in micrographs. The cut was performed in the section $Z = 0$ m as schematized in Figure 1(b), *i.e.*, a transverse section that reveals the entire ingot thickness and height and is located at mid-width. Figure 2(a) shows a typical section for trial N-4. The punching tool comes from the right-hand side in the figure. In front of the punching tool, a columnar dendritic microstructure grew from the ingot surface toward the ingot center. The columnar dendrites are slightly oriented upward as shown in Figure 2(b). This could be due to a downward liquid flow in the melt in front of the growing dendrites, as expected from previous analyses.[29] Around the center of the ingot, the morphology is changed to equiaxed due to the decrease of the temperature gradient in the liquid ahead of the growing front.[30] At the top, primary shrinkage is observed with a large void located slightly below the top solid shell. In order to avoid thermal exchange at the top, a thermal insulator powder was put on the free liquid/air interface just after filling. However, thermal exchange was not completely stopped and a thin solid shell formed. Upon further cooling, shrinkage flow leads to a typical ingot top-surface depression shape and a large void underneath. Considering the bottom of the ingot, the morphology is almost equiaxed and voids are also found. These observations are attributed to shrinkage upon solidification of an isolated hot liquid pocket. In fact, solidification is delayed in the bottom part of the ingot compared to the area located in front the punching tool because of the thermal insulator material deposited at the bottom surface of the mold to avoid metal sticking. The temperature gradient is also lowered at the bottom part, facilitating the formation of an equiaxed zone and large shrinkage porosity. Yet, void formation is not studied hereafter, as the main interest for this study is hot tearing in the section of the ingot located in front of the punching tool. Detailed analysis reveals the formation of the hot tears, as shown in Figure 2(b). The cracks are aligned with the columnar dendrites, as expected from previous observations in the literature.[31] In this micrograph, it seems stopped by the equiaxed zone. Its length reaches 20 mm in the cross section, although hot tears are obviously three-dimensional objects and this value should be seen as an underestimation. Also worth noticing is the absence of hot tear on the side of the ingot opposite to the punching tool (*e.g.*, in region $X > 0$ according to Figure 1). The total number and length of cracks observed in the transverse metallographic cross sections were measured to estimate the intensity of hot tearing as a function of the experimental conditions.

IV. THERMOMECHANICAL FINITE ELEMENT MODELING

A. *Finite Element Modeling with THERCAST®*

The numerical simulation of the punching tests consists of a thermomechanical stress/strain analysis. It is conducted using the 3D finite element code THERCAST®. The essential characteristics of the code are found in References 32 and 33. Non-linear average conservation equations for the total mass, momentum, and energy are solved at each time increment on all interacting domains as shown in Figure 1: the ingot, the different components of the mold, and the pressing punch. Yet, as regards the mechanical problem, only the ingot is considered as deformable; the mold components and the punch are assumed rigid. In the ingot, the solution covers the whole domain occupied by the metal, whatever its state: liquid, solid, or mushy. The semi-solid steel (composed of liquid and solid phases) is simply considered as a homogenized continuum with

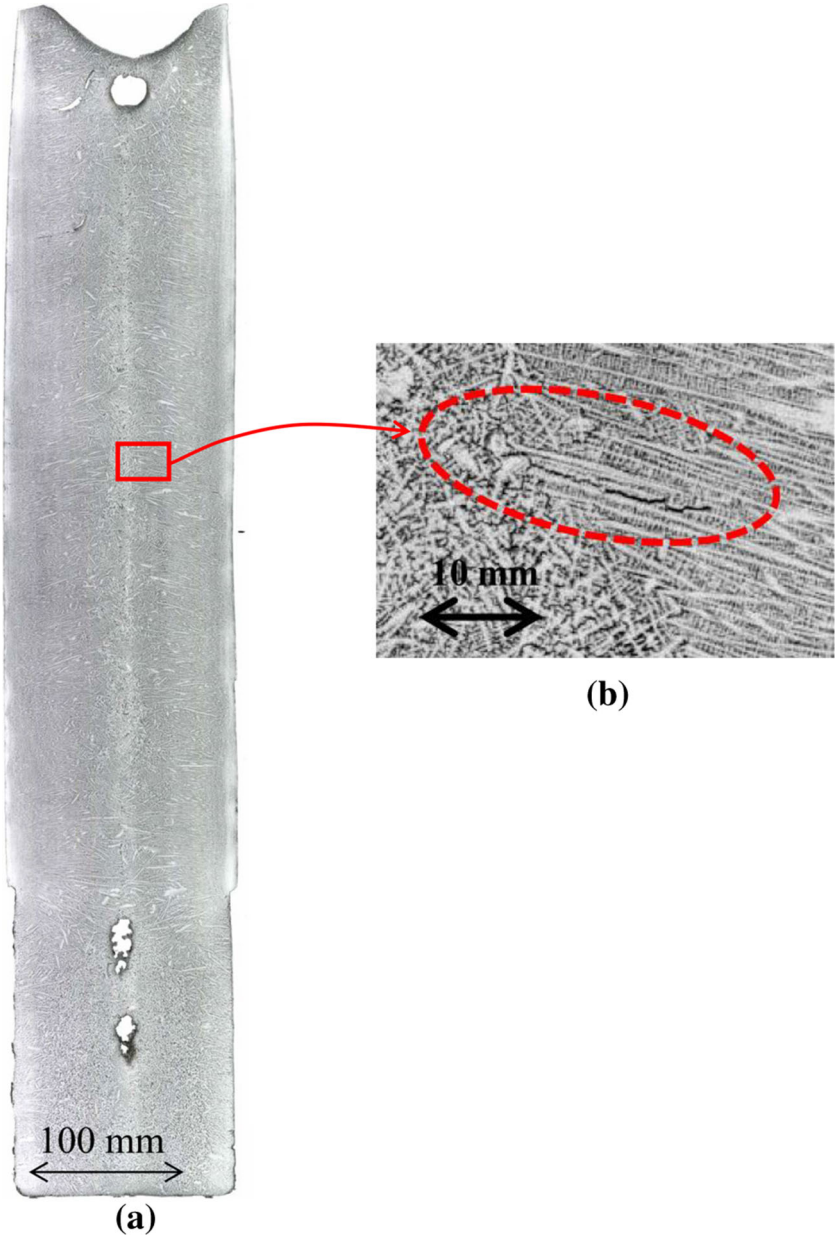

Fig. 2—Micrographs for trial N-4 with (*a*) global view of the full ingot section in plane $Z = 0$ m (Fig. 1) and (*b*) magnified view in the rectangular red window shown in (*a*) revealing a hot tear circulated with a red dashed contour. Punching was performed from the right-hand-side surface of the ingot at the window height (Color figure online).

averaged properties and a unique average velocity field $\mathbf{v}$. The thermal problem and the mechanical problem are solved sequentially at each time increment. First, the average energy conservation is solved in all domains taking into account heat exchange between them. This equation can be expressed by

$$\rho \frac{dh}{dt} = \nabla \cdot (\lambda \nabla T), \qquad [9]$$

where ρ is the average density, h is the average specific enthalpy per unit mass, λ is the average thermal conductivity and T is the temperature. Second, the mechanical problem is considered. The following average momentum and mass conservation equations are solved concurrently in the framework of a velocity-pressure formulation.

$$\begin{cases} \nabla \cdot \mathbf{s} - \nabla p + \rho \mathbf{g} - \rho \boldsymbol{\gamma} = 0 \\ \operatorname{tr} \dot{\boldsymbol{\varepsilon}}^{\mathrm{vp}} = 0 \end{cases} \qquad [10]$$

where $\mathbf{s}$ is the deviatoric stress tensor, p is the pressure, $\mathbf{g}$ is the gravity vector, $\boldsymbol{\gamma}$ is the acceleration vector and $\dot{\boldsymbol{\varepsilon}}^{\mathrm{vp}}$ is the viscoplastic part of the strain rate tensor $\dot{\boldsymbol{\varepsilon}} = (\nabla \mathbf{v} + \nabla^{\mathrm{T}} \mathbf{v})/2$.

The alloy is modeled with a hybrid constitutive equation. Details can be found elsewhere,[34] only main lines being recalled here. Over the solidus temperature,

the alloy is considered as a non-Newtonian fluid obeying a temperature-dependent viscoplastic multiplicative law, as follows:

$$\bar{\sigma} = K\left(\sqrt{3}\right)^{m+1}\dot{\bar{\varepsilon}}^{m} \qquad [11]$$

where $\bar{\sigma}$ is the equivalent von Mises stress, K is the viscoplastic consistency, $\dot{\bar{\varepsilon}}$ is the generalized strain rate and m is the strain rate sensitivity. The value of m over the liquidus temperature is equal to 1 (Newtonian fluid). In the frame of the present study, liquid flow in liquid regions is ignored and the liquid viscosity is defined as 10 Pa s for numerical stability reasons. Below the solidus temperature, the alloy obeys an elastic-viscoplastic constitutive equation, which is expressed as

$$\bar{\sigma} = K\left(\sqrt{3}\right)^{m+1}\dot{\bar{\varepsilon}}^{m} + H\bar{\varepsilon}^{n}, \qquad [12]$$

in which $\bar{\varepsilon}$ is the cumulated plastic strain, H is the strain hardening coefficient and n is the strain sensitivity. Physical properties and constitutive parameters are temperature dependent.

B. *Implementation of the Hot Tearing Criterion*

In this study, the WYSO hot tearing criterion proposed by Won *et al.*[14] is evaluated. Being interpreted like in Reference 15, this criterion is based on the cumulated strain in the plane perpendicular to the dendritic growth direction, this direction being assumed as the temperature gradient direction. The corresponding strain rate is denoted $\dot{\hat{\varepsilon}}$. Following Eqs. [1] and [8], the strain-based criterion $F_{\mathrm{HT}}^{\mathrm{WYSO}}$ is expressed as follows:

$$F_{\mathrm{HT}}^{\mathrm{WYSO}} = \int_{BTR} \dot{\hat{\varepsilon}}\,\mathrm{d}t - \hat{\varepsilon}_{\mathrm{c}} \qquad \text{with} \qquad \hat{\varepsilon}_{\mathrm{c}} = \frac{\varphi}{\dot{\hat{\varepsilon}}^{m^*}\left(\Delta T_{\mathrm{BTR}}\right)^{n^*}} \qquad [13]$$

where $\hat{\varepsilon}_{\mathrm{c}}$ denotes the strain limit which depends itself on the strain rate perpendicular to the thermal gradient and on the BTR extent. The values of parameters φ, m^*, and n^* have already been reported in Section II.[14] The values of the characteristic solid fractions bounding the BTR will be discussed further. As regards $\dot{\hat{\varepsilon}}$, it is calculated as follows. The strain rate tensor $\dot{\boldsymbol{\varepsilon}}$ is first calculated in a reference frame attached to the temperature gradient direction, the two complementary directions defining the perpendicular plane. From the four components of the tensor $\dot{\boldsymbol{\varepsilon}}$ in this plane, it is possible to calculate two eigen values. Considering that hot tearing takes place under tension, $\dot{\hat{\varepsilon}}$ is defined as the largest positive eigen value.

In THERCAST®, given the linear interpolation of the velocity field in tetrahedral elements, the velocity gradient is uniform in each element, and so is the value of $\dot{\hat{\varepsilon}}$. Hence, the criterion $F_{\mathrm{HT}}^{\mathrm{WYSO}}$ has been implemented as a constant field in each finite element, e. It is seen from Eq. [13] that the definition of the strain rate used to define the critical strain $\hat{\varepsilon}_{\mathrm{c}}$ can give rise to interpretations and discussions. The selected implementation procedure is detailed here. At each time increment i, the following quantity is calculated:

$$F_{\mathrm{HT},e}^{\mathrm{WYSO},i} = \sum_{j=i\_\mathrm{start}}^{i} \dot{\hat{\varepsilon}}_e^{j}\Delta t^{j} - \frac{\varphi}{\left(\dot{\hat{\varepsilon}}_e^{i}\right)^{m^*}\left(\Delta T_{\mathrm{BTR}}\right)^{n^*}} \qquad [14]$$

where $i_$start is the time increment at which element e enters the BTR, and Δt^{j} is the time step at time increment j. The time increment at which element e exits the BTR is denoted $i_$end. During the crossing of the BTR, the maximum value of the quantities $F_{\mathrm{HT},e}^{\mathrm{WYSO},i}$ is retained to form the hot tearing criterion. Finally, in each element e, the criterion value is defined as

$$F_{\mathrm{HT},e}^{\mathrm{WYSO}} = \underset{i=i\_\mathrm{start},i\_\mathrm{end}}{\mathrm{Max}}\left(F_{\mathrm{HT},e}^{\mathrm{WYSO},i}\right). \qquad [15]$$

C. *Simulation of Ingot Punching Tests*

As illustrated in Figure 1, half of the setup is simulated, because of the symmetry with respect to the central transverse vertical section plane. The simulation encompasses 7 domains: the ingot, 5 mold components, and the punching tool. In the ingot, the initial mesh size

Table II. Extent of the Brittleness Temperature Range (BTR) Calculated with (LR) the Lever Rule Approximation, (PE + PA) the Partial- Plus Para-Equilibrium Approximation and (EX) Deduced from Measurements

	LR	PE + PA	EX
BTR extent (K)	17.2	57.3	44.5

The corresponding solidification paths and exact alloy composition are reported in Fig. 3.

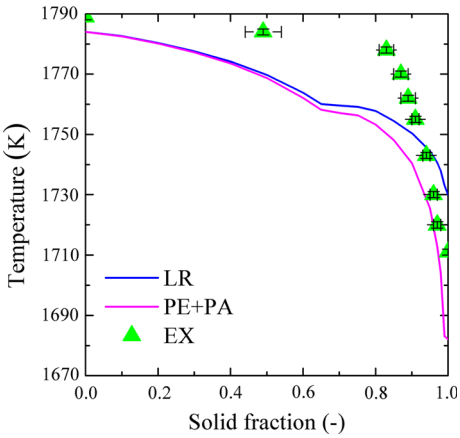

Fig. 3—Three solidification paths for targeted alloy composition (Table I) corresponding to (blue curve, LR) the lever rule approximation, (red curve, PE + PA) a combination of the partial- and para-equilibrium approximations[26,27] and (green marks with error bars, EX) experimental investigation[28] (Color figure online).

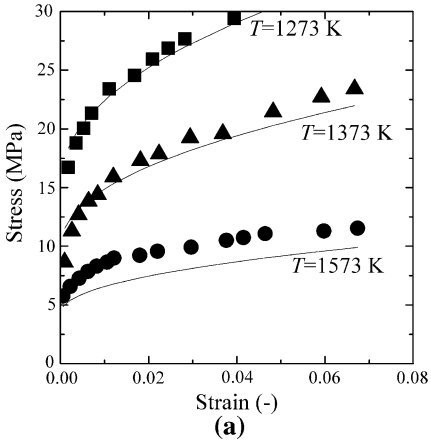

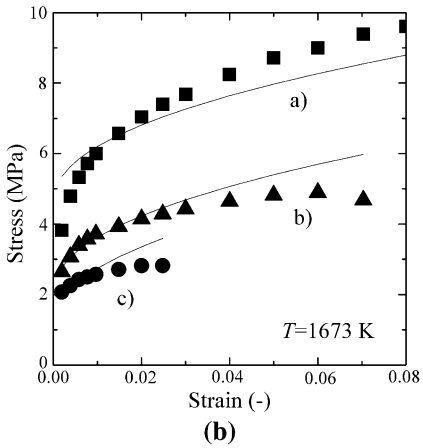

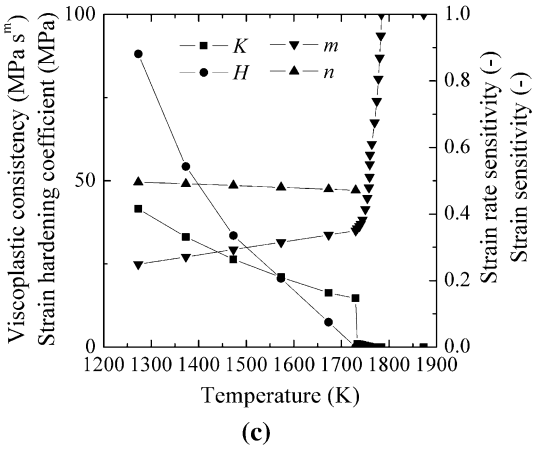

Fig. 4—Strain-stress ($\bar{\varepsilon}$-$\bar{\sigma}$) curves established by means of (marks) high-temperature tensile tests[36,37] and (curves) calculations based on Eq. [12] for (*a*) 3 temperatures from 1273 K to 1573 K (1000 °C to 1300 °C) at constant strain rate, 6.67×10^{-4} s^{-1}, (*b*) at a higher temperature, 1673 K (1400 °C), for 3 strain rates, a) 2.78×10^{-3} s^{-1}, b) 2.78×10^{-4} s^{-1}, and c) 5.58×10^{-5} s^{-1}, and (*c*) obtained constitutive parameters as a function of temperature.

is 8 mm and the number of elements is approximately 600,000. For better accuracy in the deformed region, remeshing is performed to decrease the mesh size to 4 mm just before punching, leading to 1,000,000 elements. The filling stage is not taken into account so that the thermomechanical simulation starts at the end of the

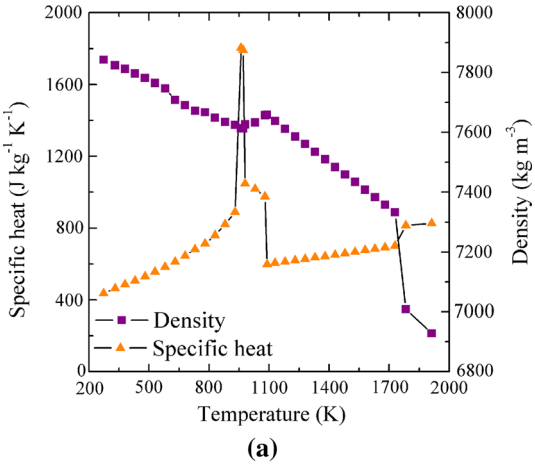

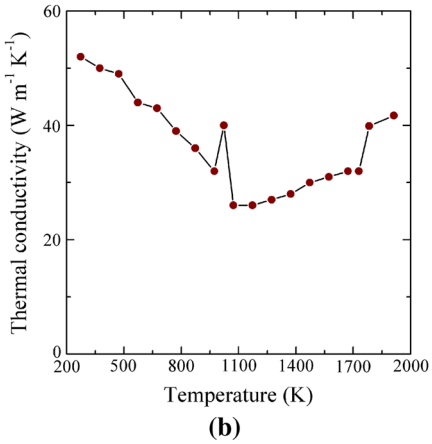

Fig. 5—Temperature-dependent average properties for thermomechanical simulations including (*a*) specific heat per unit mass c_P and density ρ while assuming full equilibrium[38,39] and (*b*) thermal conductivity λ.[40]

filling stage (70 seconds after filling start). The corresponding "initial" temperature of the ingot at that time, 1823 K (1550 °C), is estimated thanks to the measurements. It is set to 293 K (20 °C) for all other domains. The thermal boundary condition in between ingot and mold is defined through a heat transfer coefficient, the value of which depends on the air gap which may form at the interface because of shrinkage and thermal contraction. When the ingot is into contact with the mold, the heat transfer coefficient is calibrated by comparison with measurements. Its value is set to 850 W m^{-2} K^{-1}. When air gap forms, its width is considered and a heat transfer coefficient is computed taking into account of radiation and heat conduction through the air gap.[34] Regarding the ingot top, an adiabatic condition is used, thus modeling the use of the powder thermal insulator. After partial mold removal, a free surface heat exchange condition is applied to this region of the ingot surface by accounting for radiation and convection with the air at 293 K (20 °C), with the values for emissivity and convective heat transfer coefficient taken as 0.8 and 15 W m^{-2} K^{-1}, respectively.

Three different solidification paths are given in Figure 3. The first one is based on the lever rule (LR)

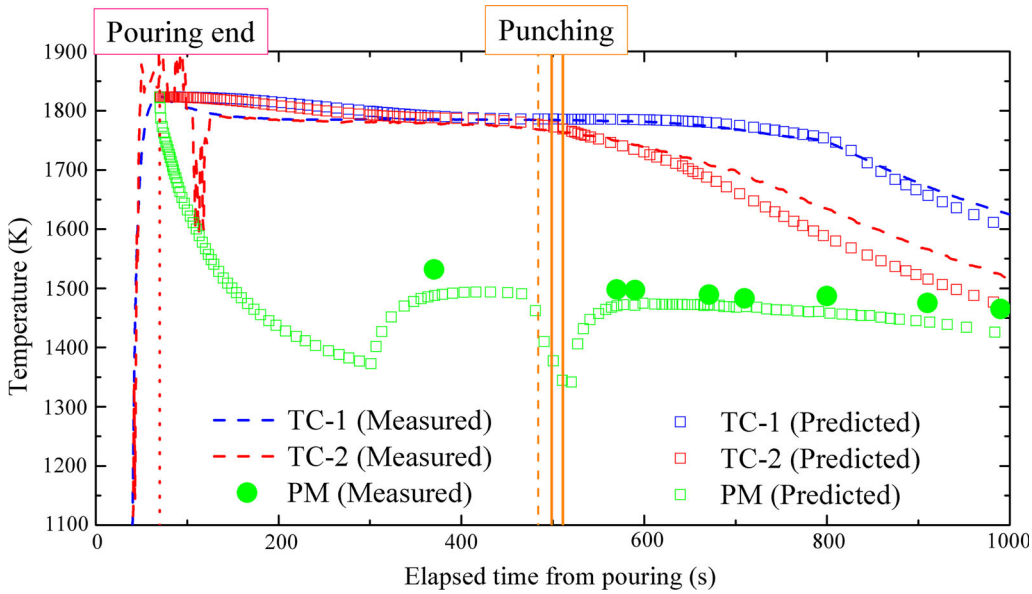

Fig. 6—Cooling curves (dashed) measured during trial N-4 and (plain) computed. Positions of thermocouples TC-1 and TC-2 and pyrometer PM are reported in Fig. 1.

approximation, meaning that full thermodynamic equilibrium is assumed in all existing phases at any temperature. The second one is a combination of the partial equilibrium (PE) approximation together with the para-equilibrium approximation (PA). It accounts for the fact that C is an interstitial element with large diffusivity compared to substitutional elements that are frozen in the solid phases. In addition, the PE + PA approximation accounts for the peritectic reaction taking place in the steel grade investigated in this study. The details of these approximations and the solidification paths for similar alloy compositions are given elsewhere.[28,35] The last solidification path (EX) is extracted from measurements conducted on a sample using interrupted unidirectional solidification. Finally, the BTR chosen in the present study is limited by solid fractions 0.9 and 0.99. Calculated values are listed in Table II for the three solidification paths given in Figure 3.

Graphs in Figures 4(a) and (b) show a comparison of experimental stress-strain plots with calculated curves based on Eq. [13]. The comparison indicates a good agreement. The temperature dependence of the corresponding constitutive coefficients in Eqs. [12] and [13] is given in Figure 4(c). Thermophysical properties shown in Figure 5(a) are deduced from the TCFE6 database assuming full equilibrium solidification path.[38,39] Latent heat is estimated to 260,000 J kg^{-1}. Tabulation of the thermal conductivity as taken from Reference 36 is also given in Figure 5(b).

V. RESULTS AND DISCUSSION

Results for experiment N-4 are first considered, a global view of the structure observed in a transverse metallographic cross section being provided in Figure 2. Analyses of the temperature history and punch force evolution permit to introduce measurements and their comparison with numerical simulations. This is done considering the 3 solidification paths shown in Figure 3, corresponding to the BTR values reported in Table II, as parameters for the simulations. The set of data detailed for N-4 are then compared with those for N-5 and N-6. As can be deduced from Table I, the punching time is doubled in N-5 as the total displacement of the punching tool is the same as for N-4 while the velocity of the punching tool is twice smaller. For trial N-6, the punching time is the same as for N-4 since the total displacement has been reduced by a factor 2 with the same velocity as for N-5. Finally, results for all trials are reported in the same graphs for a global analysis and discussion.

A. *Thermomechanical Validation*

Figure 6 shows the cooling curves recorded in the N-4 trial ingot by thermocouples TC-1 and TC-2. TC-1 (blue curves in Figure 6) is located at the center of the ingot thickness and at 190 mm from the narrow face (or inner wall of the side mold). Comparatively, TC-2 (red curves in Figure 6) is closer to the narrow face (90 mm from the side mold) but still close to mid-thickness (only 20 mm off). Both thermocouples are at the same height, *i.e.*, only 20 mm below the impact position of the punching tool with the ingot surface. Surface temperatures at the height of the punching tool using the pyrometer are also reported (circle marks in Figure 6). The calculated temperature evolution at the location of the thermocouples is in good agreement with measured data from about 300 seconds. Before this time, simulated cooling curves reveal an overestimation of the temperatures compared to measurements. A series of additional simulations were performed by progressively

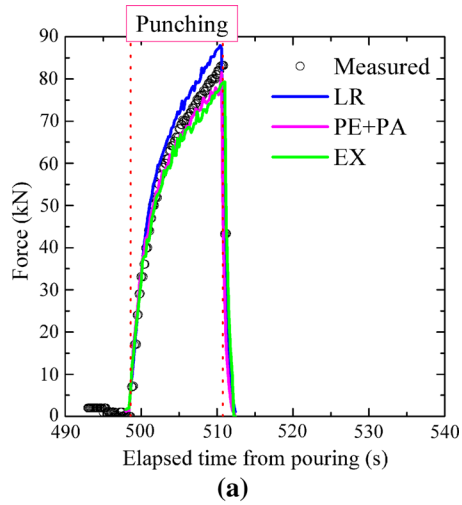

Fig. 7—Time evolution of the reaction force due to the displacement of the punching tool during trial (*a*) N-4, (*b*) N-5, and (*c*) N-6. Curves correspond to (black marks) measurements thanks to hydraulic system used to impose the movement of the cylindrical tool and (curves) simulations. Results are presented as a function of the 3 solidification paths presented in Fig. 3.

decreasing the liquid viscosity during the first 300 seconds. With more realistic properties of the melt, the predicted temperature came closer to the measurements. It should also be pointed out that the filling stage of the mold by the molten metal was not modeled. It is expected that it would further homogenize the temperature. Temperature evolution during the punching test is yet well predicted.

After 300 seconds, the top-right mold located in front of the punching tool is removed (Table I). Simulation shows that the surface temperature of the ingot then increases (green curve in Figure 6). This is expected as the heat flux decreases in the absence of the mold. At 484 seconds, identified by a dashed vertical orange line, the punching tool is in contact with the ingot surface. Pressing starts 15 seconds later, at 499 seconds, and lasts for 12 seconds (Table I). The start/end of the pressing sequence is identified by the 2 vertical orange lines in Figure 6. While no thermal signature of the punching test is made visible with the thermocouples located in the core of the ingot, it can be seen on the simulated curve extracted at the ingot surface in front of the punching tool. A large temperature decrease precedes the punching sequence, with a minimum temperature reached immediately after punching. While the punching tool goes backward with a velocity of 1.0 mm/s after punching, the temperature increases up to approximately the same level as before punching. Although it cannot be measured during pressing, the calculated temperature evolution is in good agreement with the pyrometer measurement (green symbols in Figure 6).

In order to further validate the thermomechanical simulations, the time evolution of the reaction force acting against the imposed displacement of the punching tool is plotted in Figure 7(a) for trial N-4. It is to be compared with the recorded force on the punching tool. Globally, the agreement of the simulation with measurement is good. When comparing the predictions obtained with the different solidification paths, it can be seen that an excellent agreement with the measurement is reached for the simulation using the PE + PA approximation. No large variation can be found when using EX or LR. However, the fact that the prediction using LR leads to a larger reaction force reveals the presence of a stiffer solid shell when pressing is applied. Indeed, according to LR, a higher quantity of solid is indeed present as expected from Figure 3 when considering a given temperature distribution.

Overall, the comparison of temperature and force evolutions demonstrates that thermomechanical evolutions are well simulated from about 300 seconds and up to the completion of solidification, thus demonstrating the use of satisfying thermophysical and rheological properties, as well as boundary conditions. Similar observations could be done for the other trials as shown for N-5 and N-6 in Figures 7(b) and (c). These results confirm that quantitative agreement is found for the thermomechanical load applying on the ingot surface.

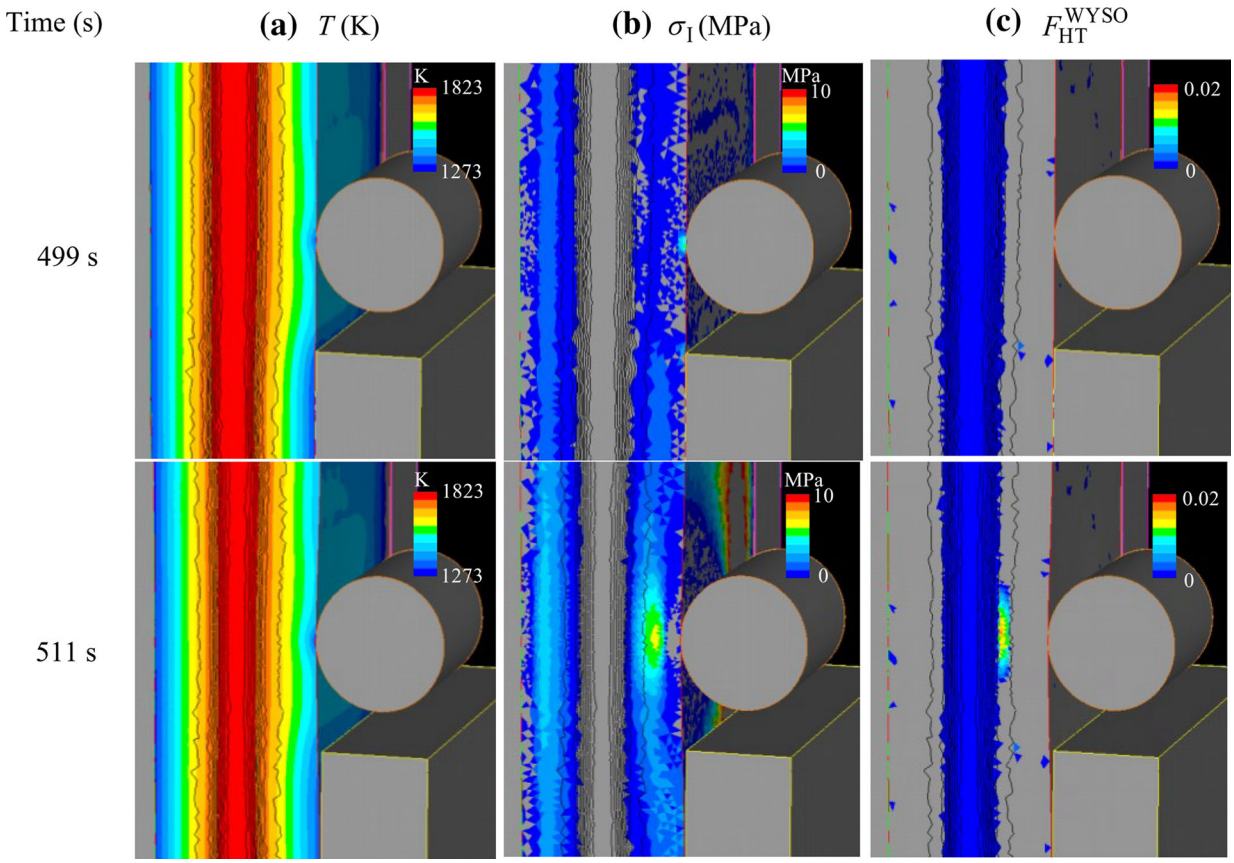

Fig. 8—Predicted results for trial N-4 (Table I) with the PE + PA solidification path (Fig. 3, Table II) showing (*a*) the temperature field, (*b*) the regions with positive values of the first principal stress, *i.e.*, under tension, the gray regions within the ingot being under compression, and (*c*) the hot tearing criterion F_{HT}^{WYSO}. The top and bottom lines show the different fields just before and after punching, respectively. Black vertical lines indicate iso-liquid fraction contours from 0 to 100 pct with 10 pct step.

This provides a sound basis in the use of the model for further interpretation of the distribution of stresses and strains, as well as their exploitation to evaluate the selected hot tearing criterion.

B. *Stress Distribution and Hot Tearing Criterion*

Figure 8 shows the numerical simulation results just after punching for trial N-4 with the solidification path labeled PE + PA in Figure 3 and Table II. The various parts of the mold and the punching tool appear with a uniform gray color, while the ingot section and surface are colored according to the distribution of (a) the temperature, (b) the first principal stress component σ_I, and (c) the hot tearing criterion F_{HT}^{WYSO}. As this is a magnified view through the various domains of the simulation shown in Figure 1, only the left, bottom-right and side parts of the mold are partially made visible. The top-right part of the mold has already been removed and the bottom part is invisible in this field of view. The cylindrical punching tool is also visible. From this view, one can better see the analogy made with the interaction with rolls in the secondary cooling zones of continuous casting machines. At the end of punching, for trial N-4, it can first be seen that a region of fully molten liquid steel still exists at the center of the ingot where the temperature is higher than the liquidus temperature of the alloy, 1784 K (1511 °C), while the surface temperature remains over 1273 K (1000 °C). Isotherms also reveal that the average temperature of the right-hand-side domain of the ingot is hotter than the left-hand side. This is compatible with the previous description of the predicted cooling curves shown in Figure 6 as cooling was found to be delayed in the absence of the top-right mold.

Figure 8(b) presents the field of the first principal stress component, just before and just after punching. For a better representation, only the tensile state is colored, regions in compression (with negative value of this first principal stress component) being represented with the same gray color as the mold parts and tool. First, it can be seen that a small region below the ingot surface, in front of the tool, is compressed. Second, and as expected from the bending created by the punch movement, tensile stresses generate and their values increase when going deeper into the ingot. However, the maximum value (around 6 MPa) is not found in the mushy zone, but in the solid, just beside the mushy zone. This is because the stiffness of the material is continuously decreasing with increasing temperature, with an

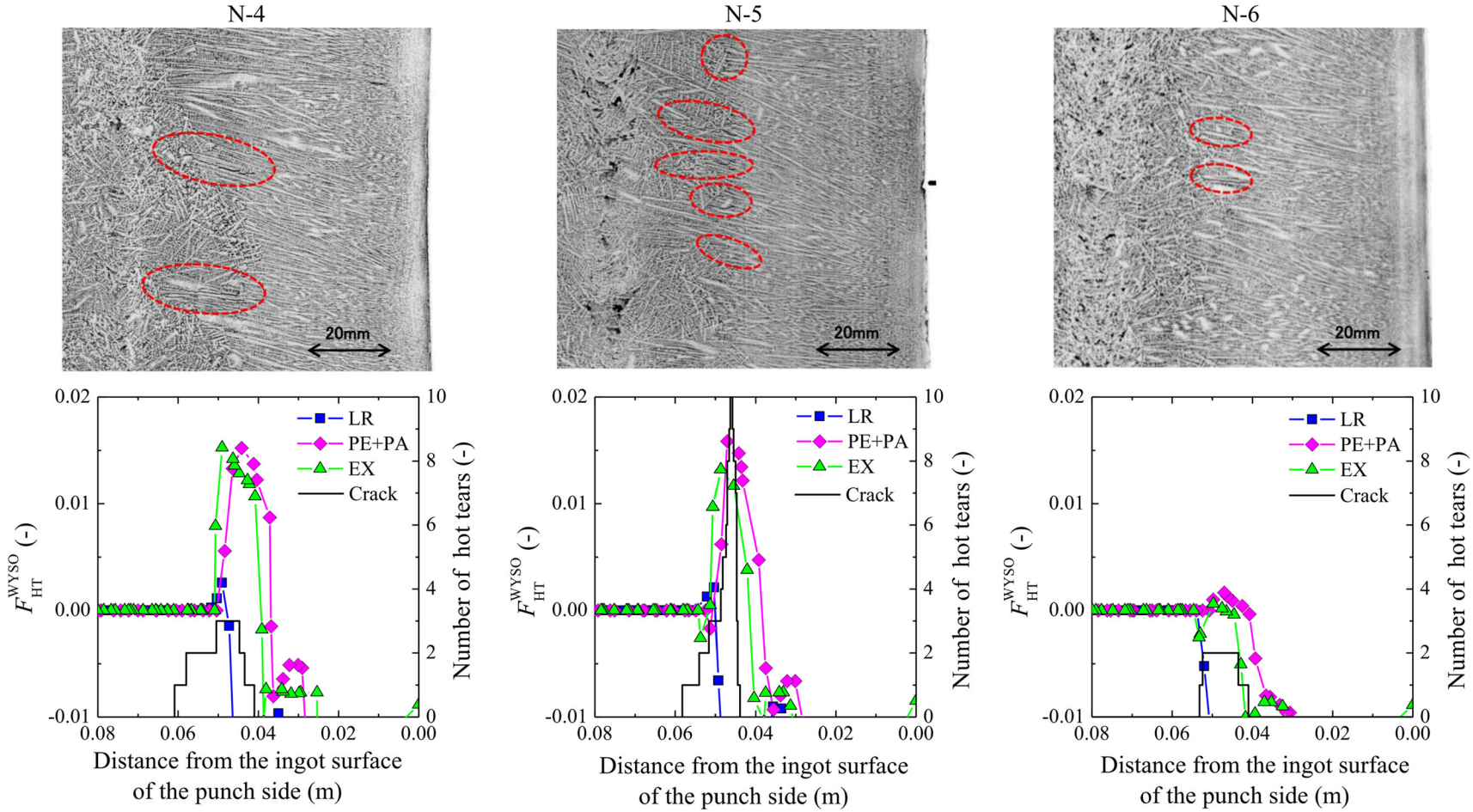

Fig. 9—Magnified micrographs for trials N-4, N-5, and N-6 on the top. In all cases, hot tears are observed and circled with dashed red contours. Note that the top circle crack in N-4 is the same as the one shown in Fig. 2(b). Also, the view being limited, not all cracks found are shown. Profiles along the ingot thickness for (black curve, right-hand-side legend) the number of hot tears and (colored curves, left-hand-side legend) the hot tearing criterion F_{HT}^{WYSO} on the bottom. Results are presented as a function of the 3 solidification paths presented in Fig. 3 for trials N-4, N-5, and N-6 (Color figure online).

abrupt decay at the solid/mushy transition. Tensile stresses also form on the left-hand side but with a much lower intensity than on the punch side.

The distribution of the values of the hot tearing criterion F_{HT}^{WYSO} is displayed in Figure 8(c). It is reminded here that those values result from an incremental build-up when crossing the BTR, as expressed by Eqs. [14] and [15]. Like for the tensile stress, only representations of regions with positive value are shown, corresponding to higher risk to form tear defects. Before punching and outside of the punching zone, there is no trace of hot tearing risk. The negative values of the criterion express that the "natural" solidification of the ingot is globally sound. Conversely, after bending, positive values appear, the higher ones being found on the punching side, at the height of the punching tool, close to the end of solidification, within the BTR. This is clear in Figure 8(c): after punching the maximum values are within the contours defined for the fractions of solid 0.9 and 1. At the end of a casting simulation, when the ingot is fully solid, the final F_{HT}^{WYSO} map is made by retaining those values and reveals a high hot tearing sensitivity only in the ingot region facing the punching tool.

C. *Hot Tearing Prediction vs Observations*

Figure 9 shows a magnified view of the micrograph for trial N-4. It is extracted from the cut schematized in Figure 1(b) and shown in Figure 2(a). In fact, the top hot tear circled in Figure 9 is the same as the one shown in Figure 2(b). Cracks were only found on the punching side of the ingot. Their number and position were measured. This was done by counting the number of cracks along the height of the ingot as a function of the distance from the punching side, *i.e.*, the right-hand-side limit of the images. Results are also presented in Figure 9 for trial N-4. The black stepwise line is thus a direct reading of the intensity of defects found. In fact, the range over which cracks are present depends on the crack lengths and the crack density is directly proportional to the number of cracks. A total of maximum 3 tears were counted 50 mm away from the ingot surface where pressing was applied. Cracks are present between 40 to 60 mm. Note that this range is close to the length of the circled crack in Figure 2(b), thus the longest in this sample.

Profiles are also provided for the criterion F_{HT}^{WYSO} in Figure 9. Positive values normally correspond to the occurrence of cracks. Considering the PE + PA solidification path (red curve), cracks are predicted to occur over a distance ranging from 36 to 50 mm. This is not far from the prediction using the experimental solidification path (EX, green curve). However, it also becomes clear from Figure 9 that prediction using the LR approximation (blue curve) is not satisfying as it almost never leads to positive values for F_{HT}^{WYSO}. The reason is linked to the small extent of the BTR (Table II) in the case of LR. Cumulated strain computed within this small temperature interval does not permit to reach the critical strain thus positive values of F_{HT}^{WYSO} over a satisfying distance. This also corroborates the finding described for the simulated reaction force that LR does not lead to results as good as the PE + PA approximation. However, while differences between PE + PA and LR when predicting the reaction force were not large, the effect on F_{HT}^{WYSO} becomes spectacular. The effect of the solidification path is thus evidenced, revealing the crucial role of the microsegregation model for the prediction of hot tearing.

D. *Comparison of Experiments and Discussions*

Figures 7 and 9 also present results of analyses for trials N-5 and N-6. Similar observations can be given for the reaction force prediction and its comparison with measurements through Figure 7. In Figure 9, however, a large number of cracks are visible for trial N-5 while very few and short ones are found for trial N-6. Again, a more quantitative illustration is given in the bottom line of Figure 9. This observation is retrieved in the distribution with a maximum number of cracks count reaching 10 at around 50 mm reported in Figure 9 for trial N-5, while only a maximum of 2 cracks are reported in Figure 9 for trial N-6. Similar trends are predicted with the distribution of the F_{HT}^{WYSO} value along the profile. The maximum F_{HT}^{WYSO} value is reached for trial N-5 while it only slightly overpasses the zero-limit from which defects are expected to form for trial N-6. In Figure 9, trial N-5 corresponds to twice the time for the reaction time and a lower reaction force for trial N-6 since the total displacement has been reduced by a factor 2 compared to trial N-4. Such results confirm the pertinence of the selected hot tearing criterion. Similar analyses as for N-4 again reveal the critical role played by the solidification path to determine the BTR extent.

In an effort to analyze the cumulated strain criterion and to compare results with literature, Figure 10 presents limit curves predicted by the WYSO criterion when based on the three solidification paths. The continuous curves correspond to the strain limit $\hat{\varepsilon}_c(\dot{\bar{\varepsilon}})$ that constitutes the second term of the WYSO criterion in Eq. [13].

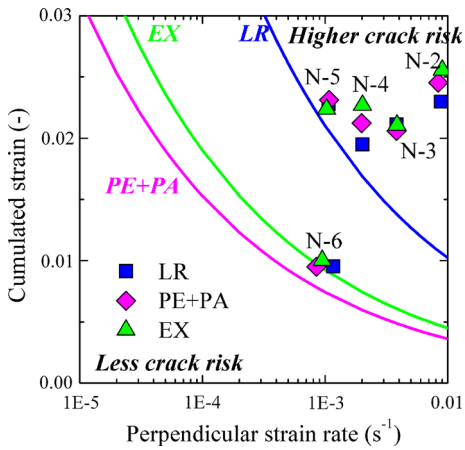

Fig. 10—Computed cumulated strain $\int_{BTR} \dot{\hat{\varepsilon}}\, dt$ as a function of the strain rate $\dot{\hat{\varepsilon}}$ perpendicular to the temperature gradient calculated when passing through the BTR. Values are taken from the F_{HT}^{WYSO} profile at the punching height, an example being shown in Fig. 9. The three continuous curves indicate the strain limit $\hat{\varepsilon}_c$ (Eq. [13]).

Note that in the expression of $\hat{\varepsilon}_c(\dot{\bar{\varepsilon}})$, the BTR extent is known a priori from the solidification path (Table II). Thus, for each curve, the half space located above the curve corresponds to $F_{HT}^{WYSO} > 0$, expressing a higher risk to form hot tearing defects. According to its smaller BTR extent, the LR limit curve is shifted toward the top-right region of the graph while the PE + PA limit curve is located in a lower (left-bottom) region, the EX limit falling in between. Calculated values are superimposed on the figure for trials N-2 to N-6. To this end, for each test, the profile of F_{HT}^{WYSO} along the thickness of the ingot at the punching tool height is exploited. The maximum value for F_{HT}^{WYSO} is taken from the profile as well as the corresponding value at the same position for the perpendicular cumulated strain: $\int_{BTR} \dot{\bar{\varepsilon}}\, dt$. The corresponding perpendicular strain rate is then recomputed with Eq. [13], using the obtained values for the maximum F_{HT}^{WYSO} and the cumulated strain. The distribution of the results in the graph is linked to the applied displacement and velocity of the punching tool as shown in Table I. It is found that the microsegregation model does not play a major role on the perpendicular cumulated strain and the perpendicular strain rate in the BTR since the three points for each trial are very close. Note that, while metallographic investigations of all these trials have revealed the presence of hot tears, only the PE + PA and EX curves give a good response. The simulation using LR does not work as N-6 is not located in the crack risk region and was yet shown to present defects.

Considering the results presented above, it appears that the expression of F_{HT}^{WYSO} not only provides us with a criterion to predict the formation of hot tears but also has potential to predict their magnitude. In order to reveal this behavior, a hot tearing index is built by considering a simple addition of the crack length measured in each of the experiments. Figure 11 presents the value of cumulated hot tearing length, expressed in millimeters, as a function of the maximum value for F_{HT}^{WYSO} obtained from its profile at punching height based on the PE + PA solidification path for each experiment. A positive slope is found that shows a significant correlation between the calculated value of the criterion function and the effective crack intensity as deduced from cumulated measured crack lengths. This indicates that the strain-based criterion can also be used to predict the hot tearing magnitude.

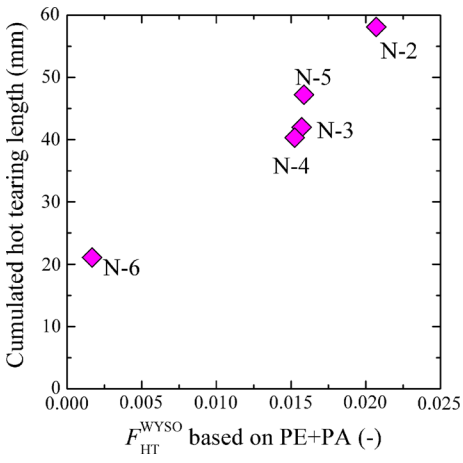

Fig. 11—Cumulated hot tearing length measured as a function of the calculated value of the maximum hot tearing criterion F_{HT}^{WYSO} using the PE + PA solidification path.

VI. CONCLUSIONS

A hot tearing study has been performed during steel solidification. Analyses include

1. punching tests using a tool to press the semi-solid ingot while it is solidifying, thus mimicking deformation under the rolls of a continuous casting machine,
2. several trials conducted for various values of the total deformation and velocity of the pressing tool,
3. measurements including thermal history through the use of thermocouples and a pyrometer as well as the reaction force acting against the imposed displacement of the pressing tool,
4. thermomechanical simulations of each trials using finite element simulations,
5. metallographic investigation of a transverse cross section of the ingot and systematic count of all cracks found to evaluate the intensity of defect formation,
6. integration of a cumulated strain-based hot tearing criterion (HTC),
7. comparison of predictions with observations.

Main findings are as follows:

1. the HTC is able to predict the risk of crack formation, provided that the brittleness temperature range (BTR) is adequately reproduced,
2. predictions in a cumulated strain versus strain rate perpendicular to the temperature gradient, as well as the reaction force, do not evidence large variation with the BTR, nor did the thermal history,
3. the role of the BTR is evidenced when drawing the HTC profile along the ingot thickness, thus revealing the critical effect of the selected solidification path,
4. excellent correlation is found between measurements and simulations concerning the position and intensity of the hot tears.

As a perspective to the present work, considering the strong sensitivity of the hot tearing prediction to the solidification path, coupling with macrosegregation has to be modeled. Indeed, deformation-induced composition variations are expected to generate variations in solidification paths.[37] This is particularly true when considering alloying elements such as C, S, or P for which low concentration variations can generate large deviations of the solidus temperature. The numerical modeling of this coupling with macrosegregation requires in turn the calculation in the mushy zone of the concurrent deformation of the solid phase and liquid flow. Some work has

been initiated by the authors of the present paper[41–43] by use of a two-dimensional "two-phase" thermomechanical model.[42,43] However, a general 3D framework implementing concurrently macrosegregation *and* hot tearing is still missing in the literature. Further developments in this direction are foreseen.

ACKNOWLEDGMENTS

This work is supported by Nippon Steel & Sumitomo Metal Corporation (NSSMC) in a collaborative project with ArcelorMittal (AM). The authors are deeply grateful to Dr Olivier Jaouen and Dr Frédéric Costes from TRANSVALOR (Mougins, France), for their kind help and discussion about thermomechanical modeling using software THERCAST®.

REFERENCES

1. J. Campbell: *Castings*, Butterworth-Heinemann, Oxford, 1991.
2. M. Wintz, M. Bobadilla, and M. Jolivet: *La Revue de Métallurgie*, 1994, vol. 4, pp. 105–14.
3. R. Pierer, C. Bernhard, and C. Chimani: *La Revue de Métallurgie*, 2007, vol. 2, pp. 72–83.
4. D.G. Eskin, Suyitno, and L. Katgerman: *Prog. Mater. Sci.*, 2004, vol. 49, pp. 629–711.
5. M. Braccini: Doctotal Thesis, Institut National Polytechnique de Grenoble, 2000.
6. A.B. Phillion, S.L. Cockcroft, and P.D. Lee: *Acta Mater.*, 2008, vol. 56, pp. 4328–38.
7. M. Sistaninia, A.B. Phillion, J.M. Drezet, and M. Rappaz: *Metall. Mater. Trans. A*, 2011, vol. 42A, pp. 239–48.
8. J.F. Zaragoci, L. Silva, M. Bellet, and C.A. Gandin: *Proc. MCWASP XIII, 13th Int. Conf. on Modelling of Casting, Welding and Advanced Solidification Processes*, Schladming (Austria), June 17–22, 2012, A. Ludwig, M. Wu, A. Kharicha, eds., IOP Conference Series 33 (2012) 012054.
9. T.W. Clyne and G.J. Davies: *Solidification and Casting of Metals*, TMS, Warrendale, PA, 1977, pp. 275–78.
10. N.N. Prokhorov: *Russ. Cast. Prod.*, 1962, vol. 2, pp. 172–75.
11. B. Rogberg: *Scand. J. Metall.*, 1983, vol. 12, pp. 51–66.
12. S. Nagata, T. Matsumiya, K. Ozawa, and T. Ohashi: *ISIJ Int.*, 1990, vol. 76 (2), pp. 214–21.
13. A. Yamanaka, K. Nakajima, K. Yasumoto, H. Kawashima, and K. Nakai: *Proc. 5th Int. Conf. on Modeling of Casting, Welding and Advanced Solidification Processes*, 1991, M. Rappaz, M.R. Ozgu, and K.W. Mahin, eds., TMS, pp. 279–84.
14. Y.M. Won, T.J. Yeo, D.J. Seol, and K.H. Oh: *Metall. Mater. Trans. B*, 2000, vol. 31A, pp. 779–94.
15. M. Bellet, O. Cerri, M. Bobadilla, and Y. Chastel: *Metall. Mater. Trans. A*, 2009, vol. 40A, pp. 2705–17.
16. M. Rappaz, J.M. Drezet, and M. Gremaud: *Metall. Mater. Trans. A*, 1999, vol. 30A, pp. 449–56.
17. H. Sato, T. Kitagawa, K. Murakami, and T. Kawawa: *Tetsu to Hagane*, 1975, vol. 61, p. S471.
18. K. Miyamura, A. Ochi, K. Kanamaru, and N. Kaneko: *Tetsu to Hagane*, 1976, vol. 62, p. S482.
19. K. Marukawa, M. Kawasaki, T. Kimura, and S. Ishimura: *Tetsu to Hagane*, 1978, vol. 64, p. S661.
20. K. Narita, T. Mori, K. Ayata, J. Miyazaki, and M. Fujimaki: *Tetsu to Hagane*, 1978, vol. 64, p. S152.
21. Y. Sugitani, M. Nakamura, H. Kawashima, and M. Kawasaki: *Tetsu to Hagane*, 1980, vol. 66, p. S193.
22. M. Rappaz, A. Jacot, and W.J. Boettinger: *Metall. Mater. Trans. A*, 2003, vol. 34A, pp. 467–79.
23. N. Wang, S. Mokadem, M. Rappaz, and W. Kurz: *Acta Mater.*, 2004, vol. 52, pp. 3173–82.
24. H. Fujii, T. Ohashi, and T. Hiromoto: *Tetsu to Hagane*, 1976, vol. 62, p. S484.
25. T. Matsumiya, M. Ito, H. Kajioka, S. Yamaguchi, and Y. Nakamura: *ISIJ Int.*, 1986, vol. 26, pp. 540–46.
26. Q. Chen and B. Sundman: *Mater. Trans.*, 2002, vol. 43, pp. 551–59.
27. M. Hillert: *Phase Equilibria, Phase Diagrams and Phase Transformations*, Cambridge University, Cambridge, 1998.
28. T. Koshikawa, C.A. Gandin, M. Bellet, H. Yamamura, and M. Bobadilla: *ISIJ Int.*, 2014, vol. 54, pp. 1274–82.
29. T. Carozzani, C.A. Gandin, H. Digonnet, M. Bellet, K. Zaidat, and Y. Fautrelle: *Metall. Mater. Trans. A*, 2013, vol. 44A, pp. 873–87.
30. C.A. Gandin: *Acta Mater.*, 2000, vol. 48, pp. 2483–501.
31. H. Fujii, T. Ohashi, and T. Hiromoto: *Tetsu to Hagane*, 1976, vol. 62, pp. 1813–22.
32. M. Bellet and V.D. Fachinotti: *Comput. Methods Appl. Mech. Eng.*, 2004, vol. 193, pp. 4355–81.
33. M. Bellet, O. Jaouen, and I. Poitrault: *Int J. Num. Methods Heat Fluid Flow*, 2005, vol. 15, pp. 120–42.
34. B.G. Thomas and M. Bellet: *ASM Handbook Volume 15: Casting, Division 4: Modeling and Analysis of Casting Processes*, American Society of Metals, 2008, pp. 449–61.
35. T. Koshikawa, M. Bellet, H. Yamamura and M. Bobadilla: *SteelSim2013, 5th Int. Conf. on Modelling and Simulation of Metallurgical Processes in Steelmaking,* Ostrava, Czech Republic, September 10–12, 2013, DVD published by the Czech Metallurgical Society.
36. Iron and Steel Institute of Japan: Mechanical behavior in Continuous Casting, ISIJ, 1985, NCID:BN03702225 (Citation Information by National institute of informatics: CiNii).
37. A. Palmaers, A. Etienne, and J. Mignon: *Stahl und Eisen*, 1979, vol. 99, pp. 1039–50.
38. P. Shi: *TCS steels/Fe-alloys database V6.0*, Thermo-Calc Software AB, Stockholm, 2008.
39. Thermo-Calc: *TCCS Manuals*, Thermo-Calc software AB, Stockholm, 2013.
40. British Iron and Steel Research Association: *Physical Constants of Some Commercial Steels at Elevated Temperatures (Based on Measurements Made at the National Physical Laboratory*, Butterworths Scientific Publications, Teddington), 1953.
41. G. Lesoult, C.A. Gandin, and N.T. Niane: *Acta. Mater.*, 2003, vol. 51, pp. 5263–83.
42. V.D. Fachinotti, S. Le Corre, N. Triolet, M. Bobadilla, and M. Bellet: *Int. J. Num. Methods Eng.*, 2006, vol. 67, pp. 1341–84.
43. T. Koshikawa, M. Bellet, C.A. Gandin, H. Yamamura and M. Bobadilla: *Proc. MCWASP XIV, 14th Int. Conf. on Modeling of Casting, Welding and Advanced Solidification Processes*, Awaji Island, Japan, 21–26 June 2015, H. Yasuda, ed., IOP Conference Series: Materials Science and Engineering 84 012096.

Chapter IV

Experimental study and two-phase numerical modelling of macrosegregation induced by solid deformation during punch pressing of solidifying steel ingots

Takao KOSHIKAWA, Michel BELLET, Charles-André GANDIN, Hideaki YAMAMURA and Manuel BOBADILLA

DOI: 10.1016/j.actamat.2016.11.023

Pages: 60 to 76 in this thesis

Acta Materialia 124 (2017) 513–527

Contents lists available at ScienceDirect

Acta Materialia

journal homepage: www.elsevier.com/locate/actamat

Full length article

Experimental study and two-phase numerical modeling of macrosegregation induced by solid deformation during punch pressing of solidifying steel ingots

Takao Koshikawa [a, b], Michel Bellet [a], Charles-André Gandin [a, *], Hideaki Yamamura [c], Manuel Bobadilla [d]

[a] MINES ParisTech, PSL Research University, CEMEF, CNRS UMR 7635, 06904 Sophia Antipolis, France
[b] Nippon Steel & Sumitomo Metal Corporation, Oita Works Equipment Division, 1 Oaza-Nishinosu, Oita City 870-0992, Japan
[c] The Japan Institute of Metals and Materials, 1-14-32, Ichibancho, Aoba-ku, Sendai 980-8544, Japan
[d] ArcelorMittal Maizières, Research and Development, BP 30320, 57283 Maizières-lès-Metz, France

ARTICLE INFO

Article history:
Received 28 April 2016
Received in revised form
7 November 2016
Accepted 8 November 2016

Keywords:
Solidification
Steel
Segregation
Modeling
Deformation

ABSTRACT

Ingot punching tests are performed on the already formed solid shell of a 450 kg steel ingot during solidification. Such test is designed in order to be representative of the thermomechanical conditions that give rise to macrosegregation during secondary cooling in steel continuous casting. In order to understand the different physical phenomena, a numerical model of the test has been developed, consisting of a two-dimensional planar finite element simulation in the median section of the ingot. A two-phase formulation has been implemented, in which the velocities of the liquid and solid phases are concurrently solved for. The simulation shows how solutes are redistributed through the central mushy zone of the ingot under the effect of the compression of the solid phase and the induced fluid flow resulting from the punching of the solid shell. By comparison with measurements of macrosegregation operated on two ingots of same initial composition but punched under different conditions, the simulation proves its capacity to reproduce the main experimental trends. However the predicted intensity of macrosegregation is lower than the one measured. Through discussion and analysis of different numerical sensitivity tests, critical material parameters and model improvements are identified in view of attaining better quantitative predictions in the future.

1. Introduction

The paper focuses on a major defect encountered during secondary cooling in steel Continuous Casting (CC): macrosegregation. This critical defect is observed at the center of continuously cast semi-products, such as slabs and billets. Like in any solidification process, macrosegregation results from the concurrent effect of microsegregation on the one hand, and the relative movement of the liquid phase with respect to the solid phase on the other. Microsegregation consists of the enrichment or depletion of the liquid phase in solutes at the scale of the dendritic microstructure. As analyzed in the pioneer work by Flemings and Nereo [1], the differential liquid motion with respect to the solid may have different causes: i) the solidification shrinkage and the thermal contraction of the solid phase, ii) the convection flow of liquid arising from its local variations of density with temperature and chemical composition, iii) the movement of equiaxed solid grains transported by the liquid flow, and iv) the deformation of the solid phase within the mushy zone. In steel ingot casting, all coupled phenomena are present and play a part in the formation of macrosegregation, but the last one (iv) can often be neglected. Regarding numerical modeling, one can refer to Wu and Ludwig, Li et al. [2,3] and Zaloznik and Combeau [4] who developed the more advanced numerical models at the present time, in the context of the finite volume method. The latter authors have also worked with two authors of the present paper to demonstrate the feasibility of finite element (FE) formulation [5].

Conversely to ingot casting, the deformation of the solid phase within the mushy zone plays a major role in continuous casting of steel. This deformation is created by the bulging of the solid shell

* Corresponding author.
E-mail address: charles-andre.gandin@mines-paristech.fr (C.-A. Gandin).

http://dx.doi.org/10.1016/j.actamat.2016.11.023
1359-6454/

between support rolls of the CC machine, which is due to the metallostatic pressure, the possible bending and unbending of the strand, and by the possible so-called "soft reduction" consisting of a mechanically applied thickness reduction of the strand operated close to the end of solidification. Such a thickness reduction of the cast product generates deformations of the underlying solid phase within the mushy zone and, as a consequence, macrosegregation. Several researchers studied these phenomena in the context of CC process with numerical modeling. Miyazawa and Schwerdtfeger [6] modelled solidification and macrosegregation, considering bulging between support rolls and the associated mushy zone deformation. In their model, mass, liquid phase momentum, solute and energy conservation equations are described in a fully Eulerian approach. The solid phase momentum equation is not solved so the velocity fields of the solid shell and of the solid phase in the central mushy region are arbitrarily given. The numerical simulation shows the formation of a center line with positive macrosegregation due to bulging. Kajitani et al. [7] studied the so-called soft reduction process using the same approach and discussed the quantitative impact of the soft reduction technique to reduce the intensity of the central macrosegregation. In a more recent contribution, Domitner et al. [8] developed a two-dimensional (2D) model covering the whole length (25 m) of the product in the caster, but still with a predefined motion of the solid phase, like in Refs. [6,7]. Fachinotti et al. [10] developed a different approach to model the mushy zone in the context of CC, using an arbitrary Lagrangian-Eulerian approach in which solid and liquid velocity fields are concurrently solved for, avoiding then the strong hypothesis over the solid velocity field which was present in previous works. With this model, the authors simulated continuous casting and similarly retrieved the effect of bulging on the formation of central macrosegregation [11]. More recently, Rivaux [12] developed an alternative approach to model the deformation of the solid phase and its Darcy-type interaction with the liquid phase in the mushy state, through a staggered scheme in which the two fields are separately and successively solved for at each time increment. However, in the end and despite lots of efforts made in developing those numerical models, none of them has been successfully applied up to the scale of a three-dimensional (3D) simulation representative of the complexity of the industrial process. This is certainly due to the considerable amount of computational power required to run the models encompassing a significant part of the secondary cooling section of an industrial caster.

This is one of the reasons why, in order to study and better understand the origin of the defect, experiments such as ingot bending or ingot punch pressing, have been developed by several researchers for many years [13–18]. The objective of these experiments is to analyze macrosegregation phenomena when they arise essentially from the deformation of the solid phase, and to do this in a configuration a priori simpler than continuous casting: ingot casting. This is obtained by deforming the external solid shell of an ingot during its solidification. The present study reports on an ingot punch pressing test which has been designed and operated by Nippon Steel & Sumitomo Metal Corporation (Tokyo, Japan). In order to analyze the test, especially from the macrosegregation point of view, a FE numerical simulation has been developed using the research code R2SOL previously developed at MINES ParisTech CEMEF [10,11]. The paper presents the test and its application to two steel ingot of similar initial composition but punched at different times (that is for different degrees of solidification progress). Then, FE modeling of thermomechanics and solute transport is introduced. Finally, results are presented and the predicted occurrence, location, and intensity of macrosegregation are explained and discussed in the light of experimental measurements.

2. Ingot punch pressing test

The schematic of the ingot punch pressing test, as developed at Nippon Steel & Sumitomo Metal Corporation, is shown in Fig. 1. It has been designed to mimic the thermomechanical loads taking place during CC process; for instance, with respect to the evolution of the cooling rate and deformation. The procedure of the experiment is as follows: the molten metal is prepared in an electric ladle furnace and the temperature is maintained at 1640 °C before pouring. The molten metal is poured into the mold from the top through a tundish. The filling duration is about 70 s. After filling, powder is added at the top of the ingot to limit heat exchanges with air. The mass of metal is approximately 450 kg. The size of the ingot is 0.16 m in thickness, 0.5 m in width and 0.75 m in height. In practice, a fibrous thermal insulator of thickness 5 mm covers the inner walls of the lowest part of the mold up to 0.2 m from the bottom of the ingot in order to avoid molten metal sticking. At a precise time after filling, the upper part of one of the two large faces of the mold is removed, as illustrated in the right part of Fig. 1(b). The ingot is then deformed during solidification by pushing a horizontal cylindrical tool perpendicularly to the surface of the ingot, its longitudinal axis being located 0.45 m from the bottom of the ingot. The tool velocity and displacement are controlled by means of a hydraulic system and measured during the test. The reaction force is also measured using the time evolution of the hydraulic system pressure.

For the alloy targeted in the present work, a total of 9 experiments, labelled N-1 to N-9 were performed. They belong to a series that aims at studying both macrosegregation and hot tearing sensitivity as these defects are frequently found to form concomitantly [19]. However, due to very demanding efforts to analyze and present the trials with respect to macrosegregation, only the test conditions referred to as N-1 and N-9 are considered in the present work. Parameters are summarized in Table 1, together with measured nominal compositions in the ladle before filling. Note that a unique alloy composition was targeted for the experimental results reported hereafter. The two tests differ first by the time at which the punching starts. For N-1 punching starts earlier on a central mushy zone richer in liquid. Conversely, for N-9, solidification is more advanced at the beginning of punching. Tests show also differences in punch displacement, the maximum punch force being limited to 450 kN for the protection of the bending equipment. In case N-9, this limiting punch force is obtained for a displacement of 9 mm, after which the punch stops. In case N-1, which is a priori less resistant, due to a less advanced solidification, the limiting force is obtained for a larger displacement of 13 mm. The temperature evolution during the test is recorded by a B-type thermocouple positioned in the ingot cavity, as shown in Fig. 1(a). For the thermocouple setting, a hole along horizontal direction, of diameter 5 mm, is pierced through the fixed large face of the mold. A thermocouple is inserted into the hole from outside and is placed at the desired position. For sealing purpose, a thermal insulator is put into the hole after setting of the thermocouple.

After the experiment, ingots were cut along their central transverse symmetry plane and micrographs were carried out after appropriate etching. Fig. 2 shows micrographs for both trials N-1 and N-9. The punching tool moves from the right to the left and the surface deformation due to punching appears clearly. Concerning microstructure, one can see a dendritic columnar microstructure which has grown from the ingot surface toward the center. Note that the primary trunk of the dendritic structure is slightly oriented upward. This is expected when considering liquid melt thermal convection oriented downward in front of the growing dendrites. Because the direction of dendrite trunks and arms correspond to ⟨100⟩ crystallographic directions in the present system, a texture of

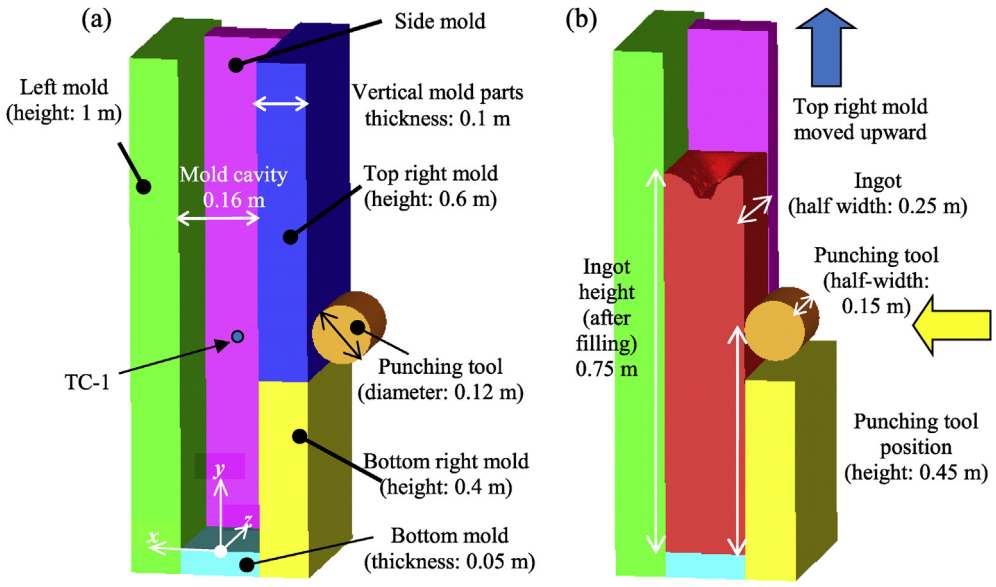

Fig. 1. Schematic of the ingot punching test developed at Nippon Steel & Sumitomo Metal Corporation showing (a) initial state and (b) punching stage after the top right mold was removed. The configuration shown is half of the setup, considering symmetry with respect to the central transverse section through the whole system. A thermocouple (TC-1) is placed at coordinates (0, 0.43, 0.06), with reference frame centered at the top surface of the bottom mold plate.

the columnar zone is thus defined. Further recirculation of the liquid in the mushy zone will no longer modify this texture settled during primary solidification. Around the center of the ingot, the morphology is changed to equiaxed due to the decrease of the temperature gradient close to the center of the ingot. At the top, primary shrinkage shape is observed and a macro void is also found below the very thin top solid shell. In order to avoid thermal exchange at the top, powder is put after filling. However, the thermal exchange is not completely prevented. So, a thin solid shell is formed at the top and the macro void is then generated below, due to shrinkage. Looking at the bottom of the micrographs, the morphology is almost of equiaxed type due to the same reason. This is associated here with the presence of the thermal insulator along the bottom surface to avoid sticking; its presence being made visible by the shape of the ingot transverse section at bottom and up to approximately 200 mm height. Because of the thermal insulation, solidification is delayed, compared to the top area. Close to the end of ingot solidification the liquid melt cannot be provided from the upper central regions due to earlier completion of solidification there. In the end, a macro void necessarily forms because of shrinkage as shown in Fig. 2 at about 150 mm height from the bottom of the ingot. The vertical white band at the ingot center reveals negative segregation. It appears very clearly so that the solute variation could be large, especially for test N-1. For quantitative analysis, Electron Probe Micro Analyzer (EPMA) measurements were performed on both ingots, for species Mn and P. Measurement conditions were as follows: beam diameter 50 μm, beam current 1 μA, integration time 50 ms, measurement step 50 μm. Line scan measurements were carried out along a horizontal line at punch height. For comparison to numerical simulation results, the measurement values were averaged over 2 mm where 40 measurement points are contained and the standard deviations were calculated at each average point. Results will be presented further (Section 4), together with the predicted macrosegregation profiles, for comparison purposes.

3. Thermomechanical and macrosegregation FE modeling

3.1. "Two-phase" thermomechanical and macrosegregation modeling

The macrosegregation formed in such a punch pressing test clearly results from the concurrent deformation of the solid phase in the mushy zone, and from the liquid flow induced by this deformation. In order to consider separately - but solve concurrently - for the liquid and solid velocity fields in the mushy zone, we apply the so-called "two-phase" model initially developed by Bellet et al. [10,11] to address macrosegregation in continuous casting. This model is also named "sponge-like" model by reference to the title of the paper of Lesoult et al. [9] in which the balance equations governing the deformation of an alloyed mushy zone were expressed. This model allows simulating solute transport phenomena leading to macrosegregation induced by deformation, shrinkage and advection. It is performed with the 2D FE code R2SOL. The main assumptions and features of the model are reminded hereafter.

- The conservation equations for the solid-liquid mixture are expressed on a representative elementary volume (REV) and are obtained using the spatial averaging method [20].
- The mushy material is considered as a saturated two-phase medium only made of solid, s, and liquid, l (i.e. $g_s + g_l = 1$ where g_k denotes the volume fraction of phase k).

Table 1
Measured nominal compositions and experimental punching conditions.

	Nominal composition (wt.pct)						Mold removal [s]	Punching start [s]	Displacement [mm]	Velocity [mm s^{-1}]
	C	Si	Mn	P	S	Al				
N-1	0.20	0.22	1.50	0.021	0.007	0.039	590	792	13	2.0
N-9	0.20	0.22	1.49	0.021	0.010	0.039	590	881	9	2.0

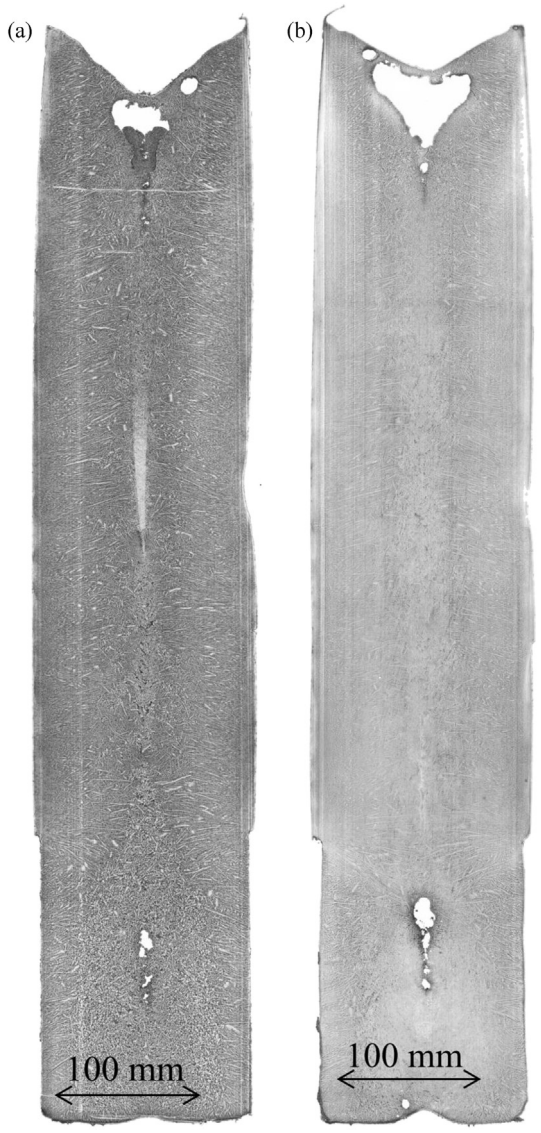

Fig. 2. Micrograph at central transverse section of (a) N-1 and (b) N-9 ingots. Macrosegreation is qualitatively revealed by the variations of the grey level. The print og the punching tool is visible on the right hand side in these images.

- At the so-called microscopic scale, within the REV, the liquid phase is considered as an incompressible Newtonian fluid. After spatial averaging, the macroscopic behavior of the liquid phase is Newtonian compressible.
- In the same way, the solid phase is considered intrinsically as an incompressible non-Newtonian fluid, and its macroscopic averaged behavior is the one of a compressible non-Newtonian fluid for which inertia effects are neglected.
- The momentum interaction between solid and liquid phases is formulated with an isotropic Darcy law.
- Solidification shrinkage is taken into account by considering different densities for the solid and liquid phases, respectively ρ_S and ρ_L. Those values are assumed constant within the solidification interval using the value at the liquidus temperature for ρ_L and the value at the solidus temperature for ρ_S, the latter being the volume-average of the density of all solid phases.
- A multi component system under lever rule approximation is assumed, meaning that the partition coefficient k_i and the liquidus slope m_i are constant for each solute element *i*.
- Local thermal equilibrium holds within the REV, ensuring the uniformity of temperature within the different phases.

The previous assumptions lead to the following set of averaged conservation equations:

$$\nabla\cdot\boldsymbol{\Sigma}^s - g_s\nabla p_l + g_l^2\mu_l\kappa^{-1}(\mathbf{v}_l-\mathbf{v}_s) + g_s\rho_S\mathbf{g} = 0 \tag{1}$$

$$\nabla\cdot\left\langle\mathbf{s}^l\right\rangle - g_l\nabla p_l - g_l^2\mu_l\kappa^{-1}(\mathbf{v}_l-\mathbf{v}_s) + g_l\rho_L\mathbf{g} = \rho_L\frac{\partial(g_l\mathbf{v}_l)}{\partial t} + \rho_L\nabla\cdot(g_l\mathbf{v}_l\times\mathbf{v}_l) \tag{2}$$

$$\nabla\cdot(g_l\mathbf{v}_l) + \frac{\rho_S}{\rho_L}\nabla\cdot(g_s\mathbf{v}_s) = \left(\frac{\rho_L-\rho_S}{\rho_L}\right)\frac{\partial g_s}{\partial t} \tag{3}$$

$$\langle\rho\rangle\frac{\partial\langle h\rangle}{\partial t} + \nabla\langle h\rangle\cdot\langle\rho\mathbf{v}\rangle + L\nabla\cdot(g_lg_s\langle\rho\rangle(\mathbf{v}_l-\mathbf{v}_s)) - \nabla\cdot(\langle\lambda\rangle\nabla T) = 0 \tag{4}$$

$$\frac{\partial\langle w_i\rangle}{\partial t} + \nabla\cdot(\langle w_i\rangle\mathbf{v}_s) + \nabla\cdot(g_lw_{l,i}(\mathbf{v}_l-\mathbf{v}_s))\nabla\cdot\left(g_lD_l\nabla w_{l,i}\right) = 0 \tag{5}$$

in which $\mathbf{v}_s$ and $\mathbf{v}_l$ are the solid and liquid velocity vectors (intrinsic average phase velocities: $\mathbf{v}_l\equiv\langle\mathbf{v}^l\rangle^l$; $\mathbf{v}_s\equiv\langle\mathbf{v}^s\rangle^s$), p_l is the liquid phase pressure ($p_l\equiv\langle p^l\rangle^l$), μ_l is the dynamic viscosity of the liquid phase, $\langle\rho\rangle$ and $\langle\lambda\rangle$ are the average density and the average heat conductivity of the solid-liquid mixture, $\langle h\rangle$ is the average enthalpy of the mixture. $\langle w_i\rangle$ and $w_{l,i}$ are respectively the average solute mass concentration and the intrinsic average concentration in the liquid phase for each solute *i*. In the momentum equations, the Darcy term introduces the permeability κ of the porous medium constituted by the solid phase. It is derived from the liquid volume fraction and the secondary dendrite arm spacing λ_2, through the Carman-Kozeny model.

$$\kappa = \frac{\lambda_2^2g_l^3}{180(1-g_l)^2} \tag{6}$$

Constitutive models for the liquid and the solid phases in the mushy zone are presented in detail in Refs. [10,11]. In summary, the average deviatoric stress tensor in the liquid phase is expressed by:

$$\left\langle\mathbf{s}^l\right\rangle = 2\mu_l\,g_l\mathrm{dev}(\dot{\boldsymbol{\varepsilon}}(\mathbf{v}_l)) = 2\mu_l\,g_l\left(\dot{\boldsymbol{\varepsilon}}(\mathbf{v}_l) - \frac{1}{3}\mathrm{tr}(\dot{\boldsymbol{\varepsilon}}(\mathbf{v}_l))\right) \tag{7}$$

where $\dot{\boldsymbol{\varepsilon}}(\mathbf{v}_l)$ is the symmetric part of the liquid velocity gradient $\nabla\mathbf{v}_l$. For solid, it is assumed that the behavior of the fully solid material is viscoplastic, of power law type, as will be introduced later. The strain-rate sensitivity coefficient of the fully solid material being denoted *m*, it can be shown that the effective macroscopic stress tensor for the solid phase in the mushy state, $\boldsymbol{\Sigma}^s = \langle\boldsymbol{\sigma}\rangle + p_l\mathbf{I}$, is a degree *m* homogeneous function with respect to the strain rate tensor $\langle\dot{\boldsymbol{\varepsilon}}\rangle^s = \dot{\boldsymbol{\varepsilon}}(\mathbf{v}_s)$. Adopting a compressible viscoplastic potential, its expression writes:

$$\begin{aligned}\boldsymbol{\Sigma}^s &= 3K\left(\sqrt{3}\,\langle\dot{\bar{\varepsilon}}\rangle^s\right)^{m-1}\left(\frac{1}{A}\langle\dot{\boldsymbol{\varepsilon}}\rangle^s + \left(\frac{1}{9B}-\frac{1}{3A}\right)\mathrm{tr}\langle\dot{\boldsymbol{\varepsilon}}\rangle^s\mathbf{I}\right)\\ &= 3K\left(\sqrt{3}\,\langle\dot{\bar{\varepsilon}}\rangle^s\right)^{m-1}\left(\frac{1}{A}\mathrm{dev}(\langle\dot{\boldsymbol{\varepsilon}}\rangle^s) + \frac{1}{9B}\mathrm{tr}\langle\dot{\boldsymbol{\varepsilon}}\rangle^s\mathbf{I}\right)\end{aligned} \tag{8}$$

in which *K* is the viscoplastic consistency of the solid material and *m* its strain rate sensitivity, both taken at the solidus temperature. The equivalent strain rate $\langle\dot{\bar{\varepsilon}}\rangle^s$ is expressed by

$$\langle\dot{\bar{\varepsilon}}\rangle^s = \left(\frac{1}{A}\langle\dot{\boldsymbol{\varepsilon}}\rangle^s : \langle\dot{\boldsymbol{\varepsilon}}\rangle^s + \left(\frac{1}{9B} - \frac{1}{3A}\right)(\mathrm{tr}\langle\dot{\boldsymbol{\varepsilon}}\rangle^s)^2\right)^{\frac{1}{2}} = \left(\frac{1}{A}\mathrm{dev}(\langle\dot{\boldsymbol{\varepsilon}}\rangle^s) : \mathrm{dev}(\langle\dot{\boldsymbol{\varepsilon}}\rangle^s) + \frac{1}{9B}(\mathrm{tr}\langle\dot{\boldsymbol{\varepsilon}}\rangle^s)^2\right)^{\frac{1}{2}} \quad (9)$$

In the flow rule (Eq. (8)), A and B are two coefficients depending on the solid volume fraction. In the present study, the expressions introduced in Ref. [10] are used:

$$A = \frac{3}{2}(1 + k_A B)\ ; \quad B = k_B \frac{1 - g_s}{g_s - g_s^{crit}} \quad (10)$$

The values of the parameters are taken from the same reference. Taking the trace of Eq. (8), it can be seen that the compressibility of the solid phase is essentially controlled by the value of coefficient B:

$$\mathrm{tr}\boldsymbol{\Sigma}^s = K\left(\sqrt{3}\langle\dot{\bar{\varepsilon}}\rangle^s\right)^{m-1}\frac{1}{B}\mathrm{tr}\langle\dot{\boldsymbol{\varepsilon}}\rangle^s \quad (11)$$

As expressed by Eq. (10), g_s^{crit} can be seen as the coherency temperature at which the compressibility of the solid phase is extremely high ($B \to \infty$). Conversely, when the solid fraction tends to one (fully solid material), A and B tend toward 3/2 and 0, respectively: the usual power law relating stress and strain rate for a dense metal at high temperature is retrieved.

In the FE code, the weak (integral) form of Eqs (1)–(5) is implemented in 2D triangular finite elements. At each time increment, the sequence of numerical resolutions is as follows:

- The *thermal resolution* is operated on the set of the different domains involved: in the present context, the solidifying ingot, the different components of the mold, and the pressing punch. The (non-linear) heat transfer resolution is carried out on each domain, successively, up to convergence (i.e. stabilization of the temperature field). In the ingot, a FE resolution of Eq. (4) is done, while in the other domains a more classical single phase form of heat diffusion is solved. Heat exchanges at interfaces between domains are expressed by the Fourier law, using heat transfer coefficients.
- The *macrosegregation resolution* is performed in the ingot, through a FE resolution of Eq. (5) for each considered solute *i*. In these resolutions, like in the thermal one, the microsegregation model (here the lever rule) is considered as it links the average concentrations in the liquid phase $w_{l,i}$ with the average mixture concentrations $\langle w_i\rangle$, and the averaged enthalpy $\langle h\rangle$ with the temperature T.
- The *mechanical resolution* is performed in the ingot, the other domains being assumed perfectly rigid and fixed. A non-linear Newton-Raphson algorithm is used, providing the nodal values of $\mathbf{v}_s$, $\mathbf{v}_l$ and p_l through a single FE resolution of Eqs (1)–(3). As the mechanical formulation presented above encompasses the central mushy zone but also the fully solidified regions, a specific treatment applies. In the FE assembly procedure, elements are considered either mushy or fully solid, according to the temperature at their center. In mushy elements, the contribution to the residue directly results from the weak form of Eqs (1)–(3). In fully solid elements, it can be noted that, by applying these equations, the liquid velocity is still present but has no real physical meaning: it is then kept close to the solid velocity field by means of the sole Darcy term in the liquid momentum equation, acting as a penalty term. The deviatoric stress tensor $\mathbf{s}$ is expressed as a function of the velocity field by the viscoplastic Norton-Hoff power law including strain hardening:

$$\mathbf{s} = 2K\bar{\varepsilon}^n\left(\sqrt{3}\dot{\bar{\varepsilon}}\right)^{m-1}\mathrm{dev}(\dot{\boldsymbol{\varepsilon}}) \quad (12)$$

where $\mathrm{dev}(\dot{\boldsymbol{\varepsilon}})$ denotes the deviatoric part of the strain rate tensor, K the viscoplastic consistency, m the strain rate sensitivity coefficient, $\dot{\bar{\varepsilon}}$ the generalized strain rate and $\bar{\varepsilon}$ the generalized strain. Strain-hardening is assumed null at solidus temperature. This is why only K (and not $K\bar{\varepsilon}^n$) appears in Eq. (8) to express the behavior model of the solid phase in the mush. The tensor Eq. (12) yields the one dimensional relation between the von Mises stress $\bar{\sigma}$ and the generalized strain-rate $\dot{\bar{\varepsilon}}$:

$$\bar{\sigma} = K\left(\sqrt{3}\right)^{m+1}\bar{\varepsilon}^n\dot{\bar{\varepsilon}}^m \quad (13)$$

The fully solid metal is then plastically incompressible and this is why, in the finite elements which are found fully solid (temperature at center lower than the solidus temperature), Eq. (3) is replaced by the following equation which simply accounts for thermal dilatation terms:

$$\nabla\cdot\mathbf{v}_s + \frac{1}{\rho_s(T)}\frac{\mathrm{d}\rho_s(T)}{\mathrm{d}t} = 0 \quad (14)$$

3.2. Specific modeling of ingot punch pressing test

The numerical simulation is two dimensional, in plane strain conditions, along the transverse mid-section of the casting system. Such a 2D approach seems a priori reasonable to analyze the results produced in this symmetry plane, the width of the ingot (500 mm) being more than 3 times greater than its thickness (160 mm). As illustrated in Figs. 1 and 7 domains are involved: the ingot, 5 mold components, and the punch. The base mesh size is 8 mm but the punching region of the ingot is refined up to 2 mm and the number of elements in the ingot is approximately 40,000. The filling stage is not taken into account so that the simulation starts immediately after the end of filling, that is 70 s after its start. The temperature of the liquid steel at that time is supposed to be homogeneous in the ingot domain. According to measurements, it is estimated to 1550 °C. Temperature is supposed uniform and equal to 20 °C for all other domains. The thermal boundary condition between ingot and

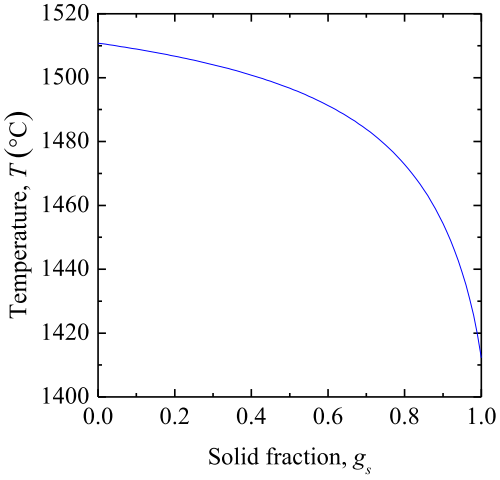

Fig. 3. Solidification path with nominal steel composition N-1 given in Table 1, by use of Thermo-Calc with the TCFE6 database [23,24] and assuming the lever rule approximation (Al is omitted in the calculation).

Table 2
Partition coefficient and liquidus slope for solutes [23,24].

	C	Si	Mn	P	S
Partition coefficient k_i	0.162	0.639	0.703	0.282	0.027
Liquidus slope m_i [K (wt.pct)$^{-1}$]	−81	−12	−5	−29	−34

mold components is defined as a constant heat transfer coefficient which is calibrated with measurement and set to 550 W m^{-2} K^{-1}. Regarding the ingot top, an adiabatic condition is used, modeling the powder thermal insulator. After partial mold removal, the free surface heat exchange takes into account radiation and convection, with values for emissivity and convective heat transfer coefficient taken as 0.8 and 15 W m^{-2} K^{-1}, respectively.

It has been underlined above that the "two-phase" solid-liquid FE model can be extended to the fully solidified metal. However, the extension to the fully liquid state is not possible. This is the reason why the simulation is actually decomposed in two successive steps, as described hereafter.

- In a *first simulation step*, started at time 70 s, a "standard" thermomechanical calculation is conducted up to the moment of punching. In this first calculation, solute transport resolution is not carried out because the mushy zone is considered as a homogenized continuum in which solid and liquid velocities are not distinguished. Instead, the mush is supposed to behave like a homogenized non-Newtonian fluid with a viscoplastic consistency and a strain-rate sensitivity varying with the sole solid fraction. The nature of the FE modeling operated is not detailed here and can be found in Refs. [21,22]. During this simulation step, solidification is governed by a unique solidification path which is defined a priori by the lever rule, based on the nominal steel composition. This solidification path is shown in Fig. 3 (see details hereunder), the liquidus temperature being 1511 °C and the solidus 1412 °C.
- A *second simulation step* is then chained to the previous one, through an automatic restart procedure including the transmission of the spatial distribution of all required variables. In this second step the "two-phase" model presented above (Section 3.1) now applies. At this moment, just before punching, the solidification of the ingot is significantly advanced and the central region of the ingot is fully in the mushy state, without any region containing liquid phase only. In the ingot domain, the simulation covers then the central mushy zone and the

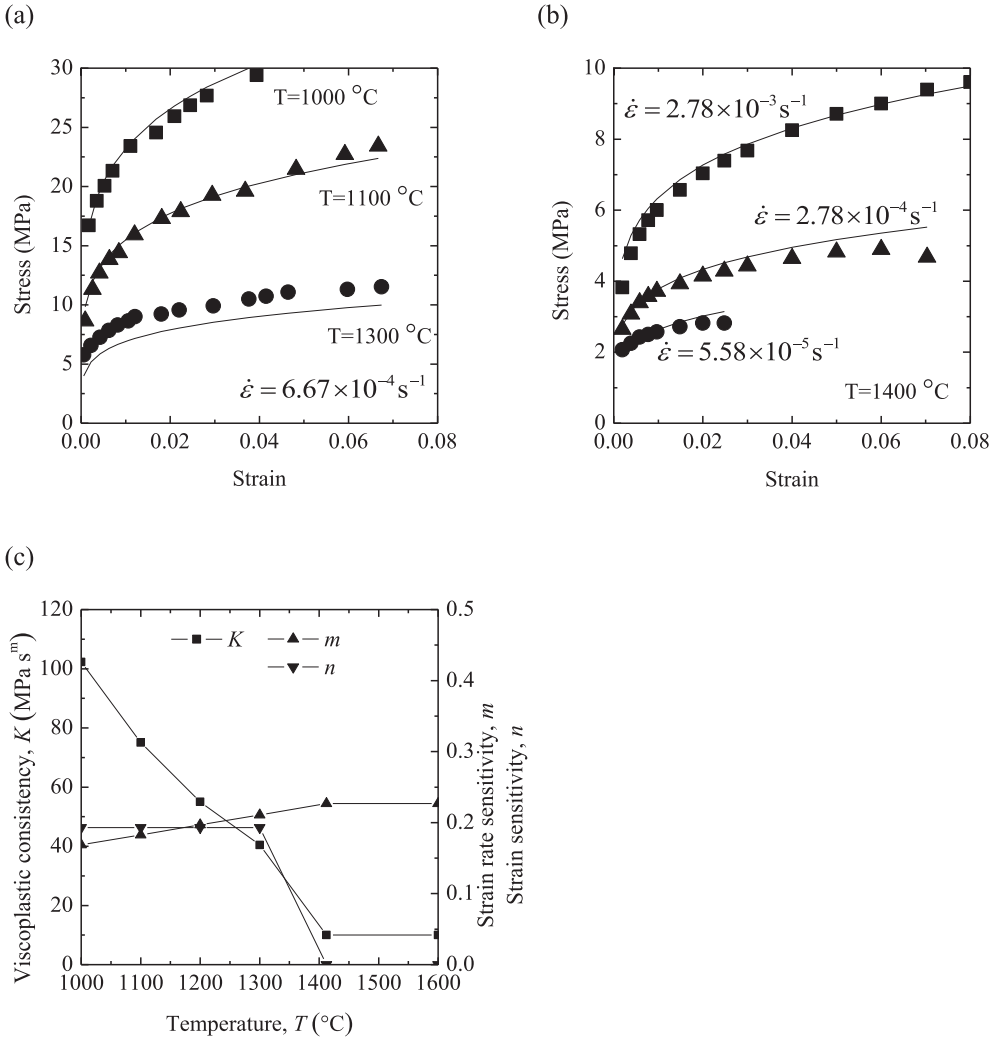

Fig. 4. Rheological behavior as strain-stress ($\bar{\varepsilon}$-$\bar{\sigma}$) relation (a) for 3 temperatures from 1000 °C to 1300 °C at constant strain rate, 6.67 × 10^{-4} s^{-1} and (b) at a higher temperature, 1400 °C, for 3 different strain rates established by means of (marks) high temperature tensile tests [25,26] and (curves) calculations based on Eq. (13). The temperature dependence of constitutive parameters for Eq. (13), assuming full equilibrium solidification, are given in (c).

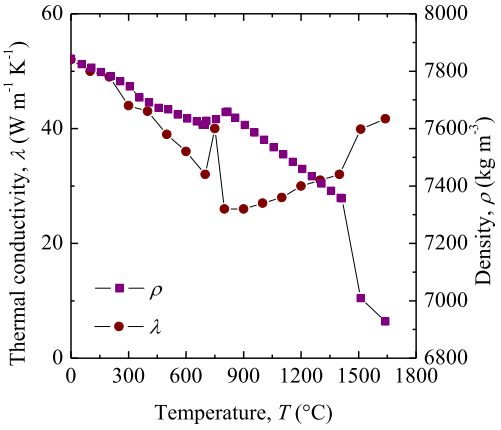

Fig. 5. Temperature dependent average properties for thermomechanical simulations including density while assuming full equilibrium [23,24] and thermal conductivity [27].

solidified shell, and is run up to complete solidification of the ingot, in order to compare macrosegregation profiles with EPMA measurements. During this second simulation step, the solidification path is no more defined a priori, since solutes concentrations vary due to liquid flow and solid deformation. Given a multicomponent system involving N_S solutes, the lever rule approximation is used to model the microsegregation phenomena. Assuming constant partition coefficients k_i and liquidus slopes m_i for each solute element i, one obtains the following relations:

$$T = T_m + \sum_{i=1}^{N_S} m_i w_{l,i} \tag{15}$$

$$\langle w_i \rangle = (g_l + (1 - g_l)k_i) w_{l,i} \tag{16}$$

$$\langle h \rangle = c_p T + g_l L \tag{17}$$

where T_m is the melting temperature of pure iron, c_p is the heat capacity (assumed constant in the present study), and L is the latent heat (also assumed constant). The number of equations is N_S+2.

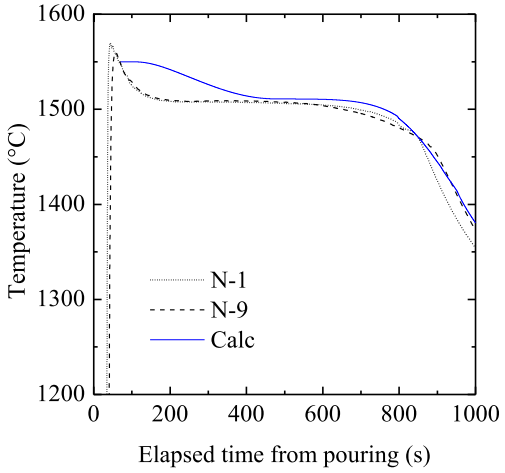

Fig. 6. Measured cooling history recorded at thermocouple TC-1 (Fig. 1) during experiments N-1 and N-9, and calculated with the finite element simulation at the nominal location of the thermocouple.

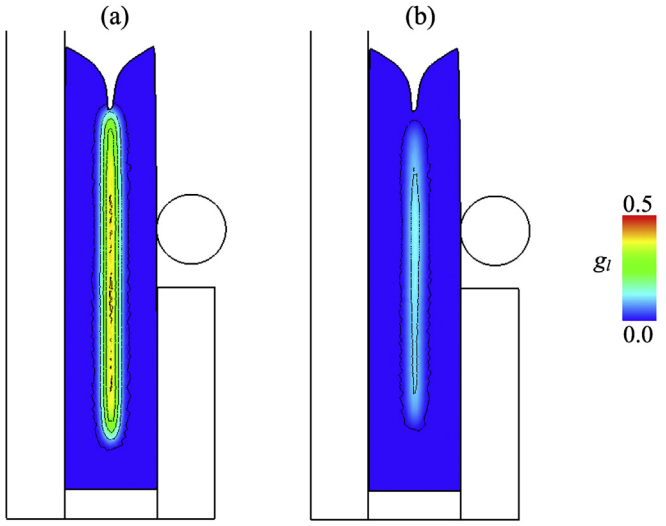

Fig. 7. Calculated shape of the ingot and distribution of the liquid fraction just before punching (a) at time 792 s (corresponding to trial N-1) and (b) at time 881 s (corresponding to trial N-9).

The average quantities $\langle h \rangle$ and $\langle w_i \rangle$ are known since these variables are obtained thanks to the global energy and solutes conservation resolutions. The number of unknowns is then N_S+2: T, g_l and $w_{l,i}$. Thus, the set of equations is well posed and can be solved iteratively at each node of the mesh. The required characteristic solutal coefficients k_i and m_i are obtained using Thermo-Calc with TCFE6 database [23,24]: their values are given in Table 2, for each of the 5 solutal elements which are considered here: C, Si, Mn, P and S. The melting temperature for pure iron is defined as 1538 °C. The constant values of the specific heat c_p and of the latent heat L are 815 J kg^{-1} K^{-1} and 260,000 J kg^{-1}, respectively. With the nominal composition, i.e. in the absence of macrosegregation, one can obtain the solidification path shown in Fig. 3. When proceeding to the initialization of nodal variables at the beginning of this second simulation step, at each node the average concentrations $\langle w_i \rangle$ are set to the nominal ones w_{i0}. Then, knowing $\langle h \rangle$ from the first simulation step, a first calculation of T, g_l and $w_{l,i}$ is carried out by solving Eqs (15)–(17).

Regarding now the mechanical data, Fig. 4 shows a comparison between experimental stress-strain plots, obtained by tensile tests performed at different high temperatures and various strain rates, and calculated curves based on Eq. (13) for optimized values of K, n and m coefficients identified by regression analysis. The comparison indicates a good agreement over the whole set of conditions tested. The temperature dependence of the constitutive parameters is shown in Fig. 4(c). As regards the liquid viscosity, it is defined arbitrarily as 0.005 Pa s [7,8]. In the Darcy term the permeability of the Carman-Kozeny model considers a constant predefined value of 300 μm for the secondary dendrite arm spacing λ_2, on the basis of measurements carried out on micrographs in case N-1. Finally, the heat conductivity and the density, as used in Eqs (3) and (14) for the latter, are shown in Fig. 5. Densities were obtained by use of Thermo-Calc software and TCFE6 database assuming full

Table 3
Comparison of calculated liquid fraction at ingot center when punching starts.

	N-1	N-9
Calculated liquid fraction	0.39	0.12
Calculated temperature, at TC-1 nominal location [°C]	1493	1455
Temperature measured by TC-1 [°C]	1487 ± 4	1461 ± 4

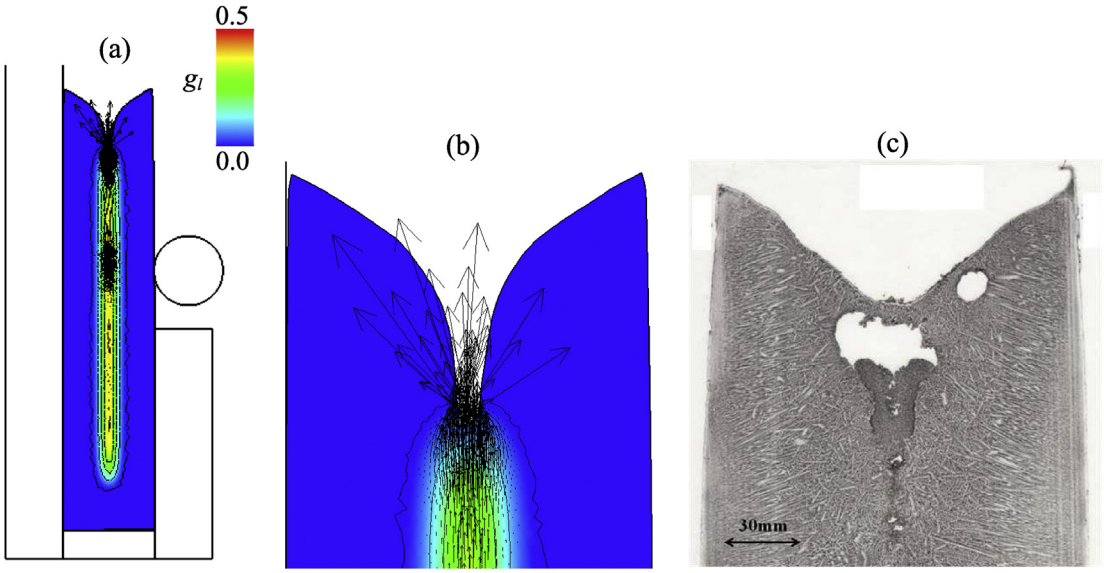

Fig. 8. Simulated and observed ingot shape showing (a) a global view of its deformation at time 792.4 s (0.4 s after punch start) for trial N-1 and (b) a zoom in the top region with shrinkage pipe to be compared with (c) observation. The simulation also shows (color map) the distribution of the liquid fraction and (black contours) isofractions of liquid, as well as the (arrows) the relative velocity of the liquid phase with respect to the solid one, $\mathbf{v}_l$ - $\mathbf{v}_s$. The darker region at the center of the micrograph is expelled liquid in the primary shrinkage cavity as a result of punching. (For interpretation of the references to colour in this figure legend, the reader is referred to the web version of this article.)

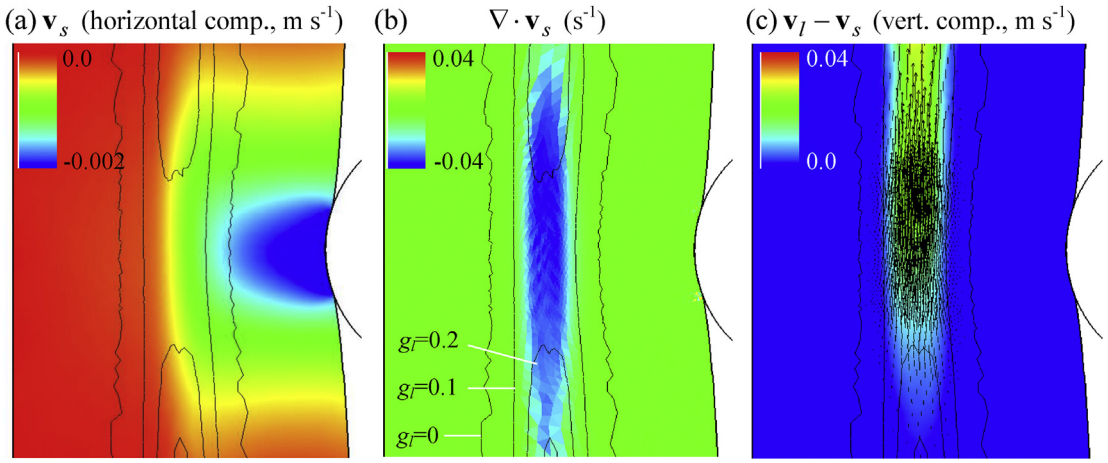

Fig. 9. Central region in the simulation of ingot N-1, 6 s after punch start, showing (a) the distribution of the horizontal component of the velocity of the solid phase $\mathbf{v}_s$, (b) $\nabla \cdot \mathbf{v}_s$ with evidence of negative values in the mushy zone at the height of the punch tool and (c) the vertical component of the relative velocity of the liquid phase with respect to the solid one, $\mathbf{v}_l$ - $\mathbf{v}_s$. The simulation also shows (black contours) isofractions of liquid, from 0 to 0.3, and (arrows) the vector field $\mathbf{v}_l$ - $\mathbf{v}_s$.

equilibrium solidification path [23,24], while the temperature dependence of thermal conductivity was taken from the literature [27].

4. Results and discussion

4.1. Micrographs for the two trials

Coming back to Fig. 2, showing micrographs for the two ingots, we note two important differences between N-1 and N-9. First of all, the clear vertical white band observed in case of N-1 is not observed in N-9. Secondly, the microstructure in the top region is found different. In case of N-1, a darker microstructure is observed, well delimited and located at the bottom of the main shrinkage pipe. It seems to partially fill the initially formed pipe cavity. This is not seen in the shrinkage cavity of N-9. Those differences are interpreted in the following section.

4.2. Numerical simulation of trials N-1 and N-9: heat transfer and mechanical analysis

Fig. 6 shows a comparison of temperature evolutions close to the ingot center. It is seen that the two cooling histories measured by thermocouples for trials N-1 and N-9 are quite close, indicating a good reproducibility obtained through an appropriate control of the procedures of mold preparation and casting. A small deviation between the two tests can be seen after 800 s, but this occurs after the punching stage and should not affect the quantitative comparison of macrosegregation.

The calculated curve shown in the figure has been obtained by the “standard” thermomechanical simulation presented above and is in good agreement with the measurements, especially during the

punching stage (starting at 792 s for N-1, and at 881 s for N-9). This good agreement is maintained up to full solidification, which is obtained after 900 s, according to the numerical simulation. This expresses a good quality of the set of thermophysical data used in the simulation, as well as a good calibration of heat exchange at interfaces. The state of the ingot just before punching, as simulated by the "standard" thermomechanical simulation in the first simulation step defined above, can be visualized in Fig. 7.

It can be seen that at that time, solidification is quite advanced. Table 3 contains quantitative information on temperature and the maximum of liquid fraction at the core of the ingot. In case of N-1, we note that the calculated liquid fraction is higher (0.39) than for N-9 (0.12). This is of course consistent with the fact that punching is activated earlier in case N-1 (792 s) than for N-9 (881 s) as reported in Table 1.

Let's consider now the deformation of the solid phase and the associated liquid flow, as calculated in the "two-phase" approach. This is illustrated in Fig. 8, for the simulation of trial N-1. The deformation of the solid shell by the punch induces a compression of the solid phase in the mushy zone (not visible in Fig. 8), which in turn induces liquid flow. For evident reasons (global quasi incompressibility of the mushy material, closed mushy pool at the bottom of the ingot), liquid flow is necessarily oriented upward. In case N-1, solidification is less advanced. The alloy is still in the mushy state in its top central region. This makes possible such an upward liquid flow, with liquid expulsion at the top surface into the primary shrinkage cavity: the expelled melt covers the already formed solid shell. The simulated liquid flow can be seen in the central part of Fig. 8. Experimental evidence of such an expulsion of liquid flow is provided by the micrograph on the right part of the figure, in which a residue of enriched (darker) expelled liquid is present at the bottom of the wedge-shaped shrinkage cavity. It is interesting to compare the shape of the shrinkage cavity between simulation and micrograph. Of course the real ingot shows a complex form, especially with a residual thin skin at the extreme top, which results from a complex thermomechanical interaction with the cover powder. This is not simulated. However, the section of the wedge-shape at the lower surface of the cavity is well reproduced by the thermo-mechanical simulation.

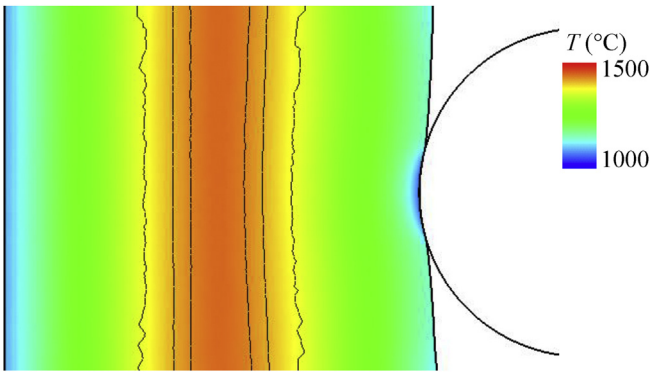

Fig. 11. Chill effect during punching shown 4 s after punching start with liquid fraction isolines.

Fig. 9 reveals in more details what happens in the mushy zone at the height of the punch tool. Due to the motion of the punching tool, the solid shell in its vicinity is displaced as shown by the horizontal component of the solid velocity (Fig. 9(a)). The resulting compression of the solid phase within the mushy zone is expressed by negative values of the divergence of the solid velocity field, $\nabla \cdot \mathbf{v}_s$, displayed in Fig. 9(b). A relative liquid flow is thus created as shown in Fig. 9(c). The compression of the solid phase primarily affects the regions of the mush for which the liquid fraction is higher than 0.1. Indeed, when liquid fraction decreases, the value of coefficient B, which controls the compressibility of the solid phase (cf. Eq. (11)), decreases as well, tending towards zero which is the limit of the B-value associated with a fully dense solid material. This continuous decrease of coefficient B hinders the compression of the solid phase

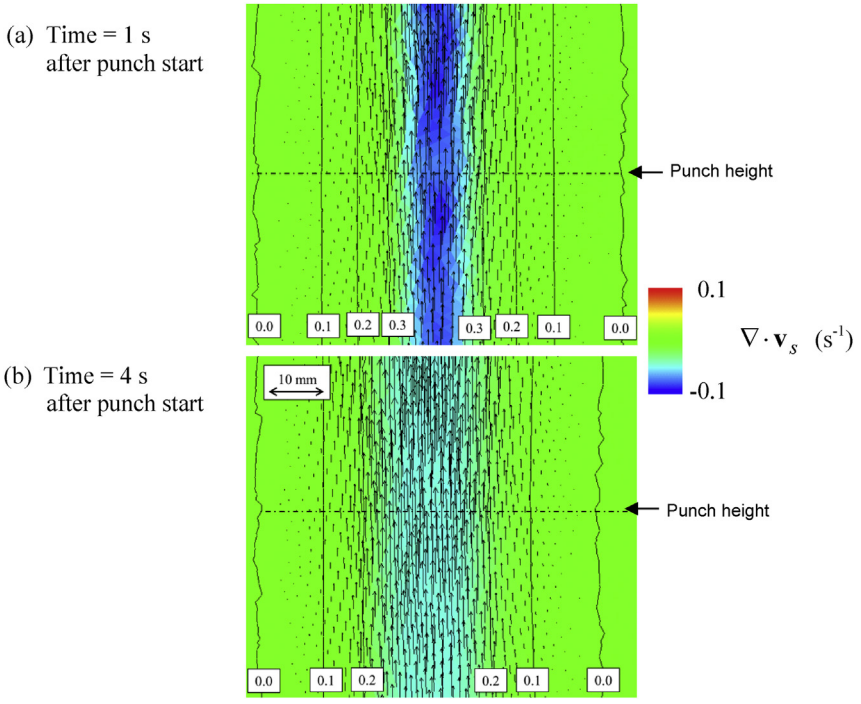

Fig. 10. Distribution of the divergence of the solid phase velocity field, together with the isolines for the liquid fraction, and a vector representation of the relative velocity field of the liquid phase with respect to the solid one: $\mathbf{v}_l - \mathbf{v}_s$. Information is given for trial N-1 during punching (a) 1 s and (b) 4 s after punch start. The horizontal dot line indicates the height of the punching tool.

at the periphery of the mushy zone, where solidification is more advanced.

Considering the mass balance equation, Eq. (3), and taking into account that advancement of solidification described by the right hand side term is much lower than $\nabla\cdot(g_s\mathbf{v}_s)$, the compression of the solid phase ($\nabla\cdot(g_s\mathbf{v}_s)<0$) creates a liquid flow. Because of the presence of the solid shell, this liquid flow is severely constrained along the horizontal direction. Therefore it is found essentially vertical but showing a positive velocity gradient along the vertical direction, thus ensuring $\nabla\cdot(g_l\mathbf{v}_l)>0$. Accordingly, the flow of the liquid phase is accelerated vertically. This resulting flow can be seen in Fig. 9(c). Note that there is no "neutral point" in front of the punch inside the mushy zone, which would separate an upper region with upward $\mathbf{v}_l$ from a lower region with a downward $\mathbf{v}_l$. As mentioned earlier, this is because of the closure of the mushy pool at the bottom of the ingot, where the solid shell cannot move, being blocked by the mold. For this reason, the liquid velocity field is uniformly oriented upward throughout the whole mushy zone, but with a vertical gradient in order to comply with the compression of the liquid skeleton through the mass balance equation (Eq. (3)).

Looking now at two different instants during punching, like in Fig. 10 at 1 and 4 s after punch start, it can be seen that the distribution of liquid fraction has changed significantly, showing a general decrease and a shift towards the opposite side to the punch (here, a shift to the left). Different phenomena contribute to the evolution of the liquid fraction.

- First, the global solidification of the ingot explains a general decrease of the liquid fraction, which should be found more or less symmetric. Looking at the left side of the mushy zone, this phenomenon is found negligible on the time interval considered: the isolines 0.1 and 0.2 for the liquid fraction are stationary.
- Second, the chill effect due to the contact with the punch. The cooling associated with the heat extraction through the punch can be seen in Fig. 11. This effect is non-symmetric but has no significant influence on the core of the ingot. Indeed, a quick estimation of the affected distance (through the expression $\sqrt{\alpha\Delta t}$ where α is the thermal diffusivity of the material and $\Delta t = 3$ s) leads to a distance of about 4 mm: the chill effect only affects the skin of the ingot, as shown in Fig. 11.
- Third, the motion of the solid phase, which is compressed and pushed toward the left direction as a consequence of the displacement of the solid shell induced by the motion of the punch. The punch velocity being 2 mm/s, the 6 mm displacement of the solid shell to the left can be seen through the displacement of the isolines 0 and 0.1 for the liquid fraction on the right side of the mushy zone. Clearly this effect is dominant. It also induces the expulsion of the liquid phase, because of mass conservation (Eq. (3)).

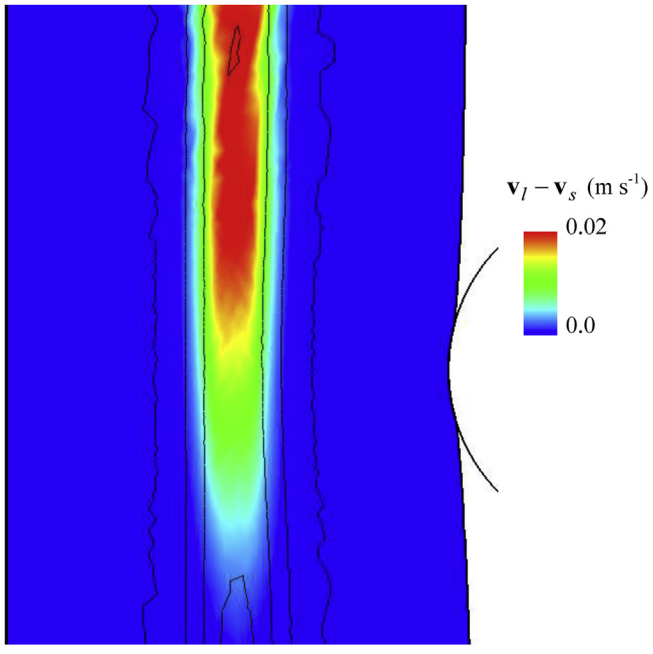

Fig. 12. Relative velocity field along vertical direction with the isolines of liquid fraction 4 s after the start of punching.

At time 4 s after punch start (Fig. 10(b)), the liquid velocity is more or less maintained, which is normal since the punch keeps moving (total duration of the motion: 6.5 s in case N-1). However, the liquid flow appears to be more uniform through the thickness of the mushy zone than at time 1 s (Fig. 10(a)). To understand this, one has to consider again the expression of coefficient B. It is maximum in the center of the mushy zone (where g_s is minimum) and continuously decreases up to the boundary of the mushy zone, where it takes the value zero. Therefore, upon combined forced movement of the solid phase and solidification, the maximum value in the center continuously decreases, and so the module of the gradient of B through the mushy zone. This expresses that the compressibility of the solid phase becomes more and more uniform throughout the thickness of the mushy zone. As a consequence, the amplitude of the values of $\nabla\cdot\mathbf{v}_s$ decreases, and so the amplitude of $\nabla\cdot\mathbf{v}_l$. Finally, that explains a decrease in the liquid velocity gradient through the thickness of the mush, as shown in Fig. 10(b).

Over the punching region, the compression of the solid phase decreases rapidly with height as it can be seen in Fig. 9(b). As a consequence, in this region, the liquid flow coming from the lower regions of the mush is distributed in the mush according to the permeability, as shown in Fig. 12. That explains higher velocities in the center, where permeability is the highest, while liquid flow is found much slower at the periphery of the mushy zone, where permeability is lower.

In the case of trial N-9, punching is triggered later in the ingot solidification. As indicated in Table 3, the maximum liquid fraction at ingot center is here limited to 0.12. Consequently, both the compressibility and the permeability of the solid phase are much lower than in case N-1. Therefore, relative velocity of the liquid flow with respect to the solid is very low. This is illustrated in Fig. 13. The mushy material tends to behave like a homogenized material in which the two phases have approximately the same velocity field. This velocity field is determined by the global incompressibility of the mush and by the displacement/deformation induced by the punch motion. In case of N-1 at 4 s after punch start, the maximum relative velocity at the punch height is around 0.02 m s^{-1}, while in case of N-9, it is about 0.002 m s^{-1} which is the same order of magnitude of punch velocity. Concerning the divergence of solid velocity, its value in case of N-4 is -0.04 s^{-1} and it is -0.007 s^{-1} in case of N-9.

4.3. Macrosegregation analysis

According to the numerical simulation described in the previous section, the remaining liquid in the mushy zone, which is enriched with solutes, is transported from the punching tool height to the ingot top. This is combined with the compression of the solid phase, and the local increase of solid fraction at punch height. From this, a negative macrosegregation is expected to take place at the ingot center, as it is effectively shown by the micrographs (see Fig. 2(a)). Let's analyze the numerical simulation of the formation of

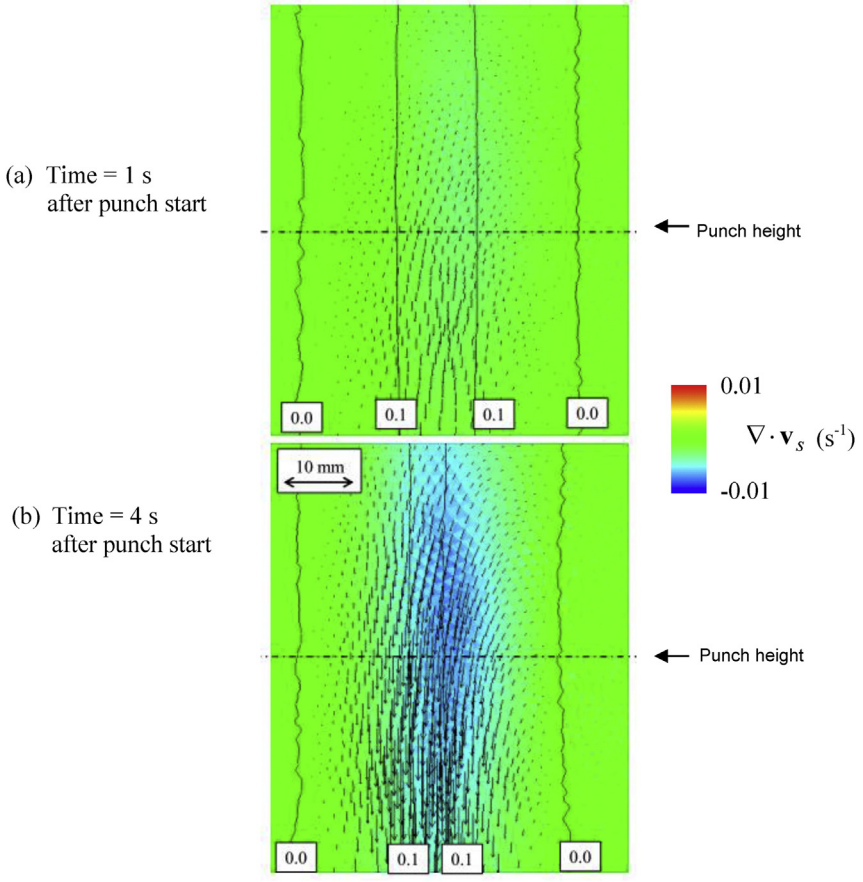

Fig. 13. Simulation of trial N-9. The punching is triggered at a later stage of solidification. Comparison can be done with Fig. 10 for trial N-1. Same caption as for Fig. 10.

macrosegregation in more detail before making quantitative comparisons.

Fig. 14 shows the progression of the macrosegregation of manganese upon punching. To understand this formation, let's come back to the nature of the governing equation (Eq. (5)) and to its numerical treatment. First, in the simulation, the FE nodes are updated according to the velocity of the solid phase, what is expressed by $\mathbf{v}_{msh} = \mathbf{v}_s$ where $\mathbf{v}_{msh}$ is the mesh velocity. Consequently, the time partial derivative of the solute concentration, which is the first term in Eq. (5), can be written as (for the sake of

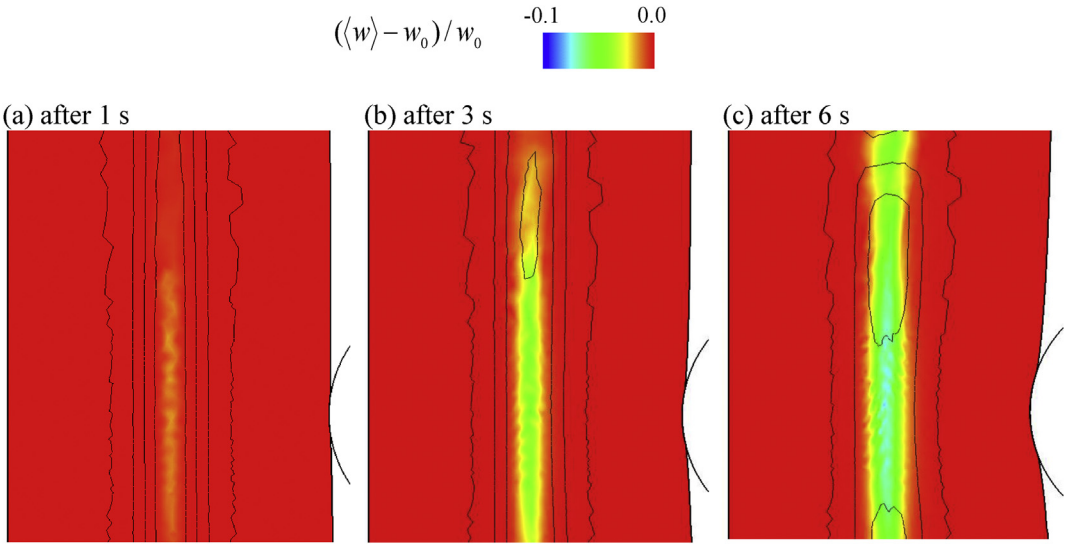

Fig. 14. Formation of a negative macrosegregation zone for Mn at the core of the ingot for trial N-1 (a) 1 s, (b) 3 s and (c) 6 s after punching start. The distribution of the relative difference in mass concentration with respect to the nominal one, $(\langle w \rangle - w_0)/w_0$, is represented, as well as the black isocontours for the liquid fraction.

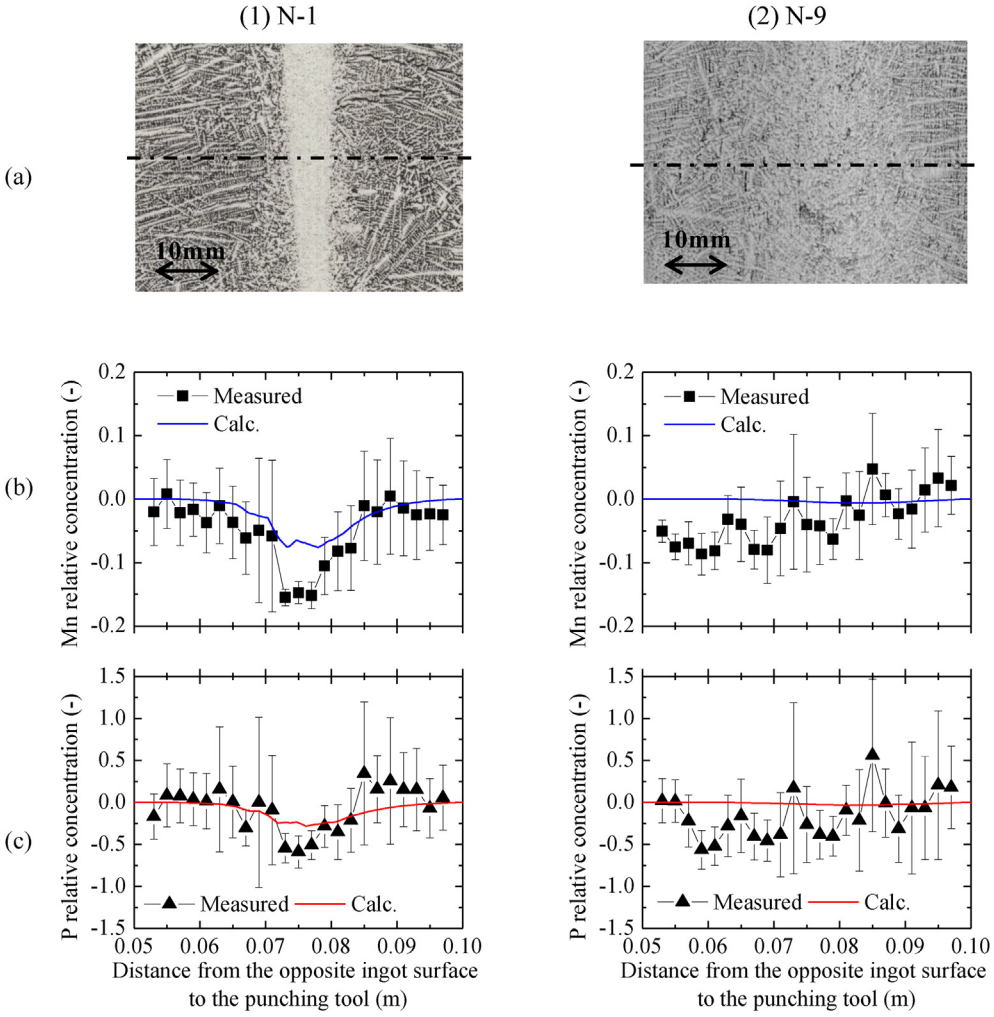

Fig. 15. Comparison of calculated and measured final segregation profiles in case of trial (1) N-1 and (2) N-9 showing (a) micrographs at punch height, and the relative variation in concentration $(\langle w_i \rangle - w_{i0})/w_{i0}$ where w_{i0} stands for the nominal initial composition in solute i for (b) Mn and (c) P. Profiles are plotted through the thickness of the ingot, at punch height, the mid-section after punching being around 75 mm from the ingot surface opposite to the punching side. EPMA measurements are indicated by (b) black squares and (c) triangles, while the continuous curves are extracted from the finite element simulations. Error bars indicate standard deviations.

simplicity, the solute index i is omitted here):

$$\frac{\partial \langle w \rangle}{\partial t} = \frac{\partial_{msh} \langle w \rangle}{\partial t} - \nabla \langle w \rangle \cdot \mathbf{v}_s \tag{18}$$

where $\partial_{msh}/\partial t$ denotes the time derivation with respect to the mesh, that is when following grid nodes (or, equivalently, following the solid phase). After injection in Eq. (5) we get:

$$\frac{\partial_{msh} \langle w \rangle}{\partial t} = \underbrace{\nabla \cdot (g_l D_l \nabla w_l)}_{\text{diffusion}} \underbrace{- \nabla w_l \cdot (g_l (\mathbf{v}_l - \mathbf{v}_s))}_{\text{advection}} \underbrace{- (w_l \nabla \cdot (g_l (\mathbf{v}_l - \mathbf{v}_s)) + \langle w \rangle \nabla \cdot \mathbf{v}_s)}_{\text{compression of solid phase}} \tag{19}$$

The different contributions to the formation of macrosegregation can then be clearly identified: diffusion in the liquid phase, transport (advection) due to the relative velocities of liquid and solid phase, compression of the solid phase. Owing to the very low diffusion coefficient D_l, of the order of 10^{-9} m^2 s^{-1}, the contribution of diffusion is marginal. The second contribution is also quite limited in the present situation because the gradient of

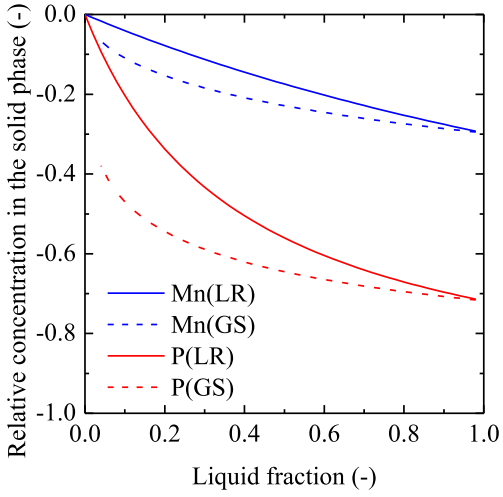

Fig. 16. Relative variation of average solute concentration in the solid phase as a function of the liquid fraction. The dependence is plotted for solutes Mn and P, and for two microsegregation models: (LR) lever rule and (GS) Gulliver-Scheil. The relative variation of the concentration in the solid phase is calculated as $(w_{s,i} - w_{i0})/w_{i0}$ where w_{i0} is the concentration of solute i at the beginning of solidification.

the liquid concentration is essentially horizontal whereas the relative velocity $\mathbf{v}_l - \mathbf{v}_s$ is essentially vertical. Therefore their dot product remains small. Finally the only significant driving force for macrosegregation lies in the last term associated with the compression of the solid phase. Comparing Fig. 14(c) and Fig. 9(a), this is clearly revealed, as macrosegregation principally affects regions where liquid fraction is higher than 0.1 and where the maximum values of $|\nabla\cdot\mathbf{v}_s|$ can be found. That also explains that macrosegregation principally forms in the punching region and has a limited extension apart from this area. This can be seen in Fig. 14 where the time evolution of the vertical extent of the segregated zone is limited.

Fig. 15 illustrates from a qualitative and a quantitative point of view the final macrosegregation in both cases N-1 and N-9. As already commented with Fig. 2, the two micrographs shown in the top line of Fig. 15 indicate a marked segregation in case N-1 and no clear trend of segregation for trial N-9. This is confirmed by the measurement profiles obtained by EPMA, for species Mn and P along horizontal lines on the transverse surface shown in Fig. 2, around the punching height. In the case N-1, a significant depletion in Mn and P is measured in the central region of the ingot: the relative variations in concentration are −15% for Mn and −60% for P. As expected, the segregation is more marked for P, for which the partition coefficient is smaller (cf Table 2). Indeed, a lower partition coefficient leads to a higher ratio of liquid vs solid concentrations within the mush, so that the magnitude of the macrosegregation is increased. In case N-9, EPMA profiles do not show a clear evidence of a central macrosegregation, confirming its absence on the micrograph.

Regarding the profiles issued from the numerical simulation, in case N-1, they show a central depletion with relative variations of −8% for Mn and −28% for P. In case N-9, no significant macrosegregation is calculated. Thus, the numerical simulation results show the same trends as the measurements: more intense central macrosegregation for P than for Mn; no significant macrosegregation in case N-9. One should add that a numerical test was performed with no punching, i.e. leaving the ingot solidifying with no other external mechanical forces than those created by shrinkage. No macrosegreation was found, the profiles of the solute concentration remaining flat, equal to the nominal alloy composition, in front of the punching tool. Despite this good qualitative agreement with measurements, the intensity of the calculated segregation is found much lower than in reality, roughly by a factor 2. There are several possible causes for these differences, which will be discussed in the following section.

4.4. Discussion on the amplitude of macrosegregation

Experimental observation and “two-phase” numerical simulation reveal the phenomena taking place in the mushy zone: a central negative macrosegregation forms under the concurrent effect of compression of the solid phase, and induced flow of the liquid phase from the punch region toward the top of the ingot. The causes that could explain the too weak intensity of the computed central macrosegregation can be classified in two main categories. The first one comprises the causes for a possible too low enrichment of the liquid phase. The second one comprises the causes for inappropriate solid deformation and induced liquid flow. These two error sources are discussed hereunder.

- Enrichment of the liquid phase. Influence of the microsegregation model

The solutes partition between the liquid phase and the solid phase is crucial since both phases are transported in this study. The solutes enrichment of the liquid phase, or equivalently, the solutes impoverishment of the solid phase, is directly linked to the partition coefficients, which are key variables in any microsegregation model.

Besides the lever rule model, which is used in the simulation, we consider here the Gulliver-Scheil (GS) model, in which complete mixing is assumed in the liquid phase but no diffusion is assumed in the solid phase. In this latter case, and assuming a “closed system” approach (in which the average concentration remains constant all along the solidification for a considered material point), we have for any solute i [28]:

$$w_{l,i} = \langle w_i \rangle g_l^{k_i - 1} \quad \text{for GS} \tag{20}$$

In the case of the lever rule (LR), we get, under the same closed system assumption (see also Eq. (16)):

$$w_{l,i} = \frac{\langle w_i \rangle}{g_l + (1 - g_l)k_i} \quad \text{for LR} \tag{21}$$

The evolution of the variation of the average concentration in the solid phase as a function of the liquid fraction can be derived easily from the total mass balance of solute specie i $\langle w_i \rangle = w_{l,i} g_l + (1 - g_l) w_{s,i}$ and Eqs (20) and (21). The respective expressions are as follows:

$$w_{s,i} = \langle w_i \rangle \frac{1 - g_l^{k_i}}{1 - g_l} \quad \text{for GS} \tag{22}$$

$$w_{s,i} = \langle w_i \rangle \frac{k_i}{g_l + (1 - g_l)k_i} \quad \text{for LR} \tag{23}$$

Fig. 16 shows the evolution of the relative variation of the average solute concentration in the solid phase for Mn and P, $(w_{s,i} - w_{i0})/w_{i0}$, according to the two microsegregation models with w_{i0} the nominal alloy composition replacing the average solute content $\langle w_i \rangle$. The effect of the partition coefficient can be seen by comparing the evolutions for Mn and P. Additionally, for each species, the effect of the microsegregation model can also be seen. As expected, the plots for P are found below those for Mn. As regards the liquid fraction effect, the lower the liquid fraction is, the higher the relative concentration in the solid phase, and so the lower the amplitude of the relative variation. In the case N-1, the maximum liquid fraction calculated at punch start is 0.39, as presented in Table 3. From Fig. 16, the relative variation of the concentration in the solid phase for Mn and P is estimated in the case of LR as −0.14 and −0.50, respectively. This leads to a ratio between these variations of about 3.6, at punch start.

Looking now at the simulation results, it is found that the maximum relative variations of concentration, after punching, are −0.076 and −0.282 for Mn and P, respectively (see Fig. 15). Thus, the ratio of these variations is around 3.7, very close to the initial ratio before punching. This is fully consistent, as during the 6 s of the punching stage, the enriched liquid phase is simply transported through the mush: the ratio P/Mn is kept unchanged. Besides, it is worth noting that this ratio is found around 4 for the EPMA measurements (−0.15 and −0.60 for Mn and P, respectively). This good agreement on the ratio between the amplitude of segregation for Mn and P indicates that simulation captures well the relative segregation for each species.

Another issue is the concentration in the solid phase itself. At punch start, according to Table 3, the liquid fraction is $g_{l,start} = 0.39$. The average Mn concentration in the solid phase is $w_{s,start} = 0.86 w_0$. This latter value is computed from Eq. (23) or deduced from Fig. 16 following the LR approximation. Similarly, the average Mn

Table 4
Summary of sensitivity tests. N-1 is the reference simulation while S-1, S-2, and S3 are three sensitivity tests. The underline value for tests S-1, S-2 and S-3 identifies the modified parameter with respect to N-1.

	N-1	S-1	S-2	S-3
Multiplier applied to the viscoplastic consistency K over the solidus temperature	1.0	0.5	1.0	1.0
Multiplier applied to the compressibility coefficient B	1.0	1.0	2.0	1.0
Secondary dendrite arm spacing λ_2 [μm]	300	300	300	1000
Maximum relative variation in concentration for Mn	−0.076	−0.092	−0.090	−0.082
Relative variation with respect to reference	–	+21%	+18%	+8%

concentration in the liquid phase can be deduced using Eq. (21), which yields $w_{l,start} = 1.22w_0$. From the simulation, the liquid fraction after punching was computed: $g_{l,end} = 0.17$. Note that it corresponds to an increase by 36% in solid fraction, i.e. (1−0.17)/(1−0.39) = 1.36. The simulation also shows that this compaction of the solid phase is associated with an almost pure vertical transport of the fluid that can still circulate in the mushy zone. Evaluation of the Mn segregation index after punching with respect to the nominal composition w_0, $(\langle w\rangle - w_0)/w_0$, is then possible considering the total mass balance of solute. Assuming the composition of the two phases unchanged during the short punching time (6.5 s), we have, at the end of punching:

$$\langle w\rangle_{end} = g_{l,end}w_{l,start} + \left(1 - g_{l,end}\right)w_{s,start} \tag{24}$$

This leads to a segregation index after punching equal to −0.08 for Mn. This value is very close to the minimum read for the computed relative Mn concentration profile which is displayed in Fig. 15(b1), showing that the estimations provided by the present simple analysis are found quite close to the more sophisticated numerical simulation. As stated before, this result yet underestimates macrosegregation, the minimum exhibited in Fig. 15(b1) for the measured segregation profiles for Mn being −0.15. It should be noted here that it was checked that numerical simulation shows almost no evolution of the segregation profiles between the end of punching and complete solidification. Actually, after punching the permeability is low enough to prevent any significant fluid flow. Therefore, the simple estimations calculated above after punching can be reasonably compared to the measurements done on fully solidified ingots.

Let's now examine what would be the situation considering GS instead of LR. Assuming the same initial liquid fraction at punch start, $g_{l,start} = 0.39$, and applying Eqs (20) and (22), the Mn concentration in the liquid and solid phases would be $w_{l,start} = 1.32w_0$ and $w_{s,start} = 0.79w_0$, respectively. Further assuming the same increase of solid fraction − through compaction − by 36% in the mushy zone, leading to $g_{l,end} = 0.17$, the average Mn concentration obtained by Eq. (24) yields now $\langle w\rangle_{end} = 0.88w_0$, that is a segregation index after punching equal to −0.12. This value comes closer to observation.

As a conclusion, it can be said that the choice of the microsegregation model has a significant influence on the intensity of the macrosegregation (increasing it by 45% in the case of Mn). Thus, it might be interesting to consider more sophisticated microsegregation models, like those taking into account partial equilibrium with peritectic transformation [29]. In addition, undercooling effect could be taken into account, providing a more accurate solidification path and initial liquid fraction before punching.

- Influence of solid compression and associated liquid flow

The compression of the solid phase and the liquid flow obviously play a prominent role in solutes distribution, as already underlined when commenting Eq. (19) governing the evolution of average solutes concentration. Consequently, a few parameters are expected to have an impact on the amplitude of segregation. A first set of parameters consists of the constitutive parameters of the solid phase, and among them particularly the viscoplastic consistency K and the compressibility parameter B. Indeed a lower value of the consistency, or a greater value of B, would favor the compression of the solid phase and then increase the amplitude of macrosegregation. A second set of parameters consists of those governing the permeability of the solid network and so the distribution of liquid flow through it. Assuming Eq. (6) for the isotropic permeability, the only parameter is in fact the secondary dendrite arm spacing λ_2.

In order to test the influence of those parameters, a sensitivity analysis is considered. It consists of three tests for which, all other things being equal, the value of one of the parameters K, B and λ_2 has been changed. The considered changes for each of the coefficients are indicated in Table 4. They are all expected to induce a more marked negative segregation in the ingot center: viscoplastic consistency divided by two; compressibility coefficient doubled; secondary dendrite arm spacing multiplied by three. The last line of the Table contains the value of the maximum (in absolute value) relative variation of average Mn concentration obtained in each simulation. As expected, the three test simulations show a more severe central negative macrosegregation, which again shows a good qualitative response of the “two-phase” FE calculation. In comparison with the reference simulation N-1, the magnitude of Mn segregation index is increased by 21% in simulation S-1 (influence of K), 18% in simulation S-2 (influence of B) and by 8% in simulation S-3 (influence of λ_2). Considering the large variations tested for those parameters, it appears that their influence is effective, but probably lower than the impact of the choice of the microsegregation model, as discussed above.

5. Conclusions

An ingot punch pressing test has been developed to better understand the phenomena affecting the solid shell and the central mushy zone of steel semi-products when crossing the secondary cooling section during continuous casting. The test consists of the punching of one side of the solid shell of a partially solidified steel ingot by an external tool. The present study is focused on the formation of macrosegregation induced by this punching operation. The deformations of the solid shell and of the central mushy zone are simulated numerically. The mechanics of the mushy zone is addressed by a “two-phase” approach, in which the compressible deformation of the solid phase and the liquid flow are solved concurrently, as they are in close interaction. Coupling with the numerical solution of solute mass transfer induced by liquid flow is achieved, thus simulating the occurrence of macrosegregation. A 2D FE method is used to solve all conservation equations in a single model.

Two experimental tests are selected, consisting of two ingots of the same steel grade, but punched at different instants, corresponding to different progressions of their solidification prior to

punching. Simulations with the "two-phase" FE model demonstrate the ability to capture the essential phenomena that drive macrosegregation in the ingot punch pressing tests: compression by mechanical deformation of the porous solid phase combined with liquid flow through the permeable medium. The compression and its resulting permeability decrease are more marked for the ingot where solidification was less advanced at the onset of punching. It leads to the formation of intense negative central macrosegregation in the upper half part of this ingot. For the second ingot punch pressing test, deformation was also simulated but it did not generate significant macrosegregation as solidification was more advanced at the onset of pressing, thus hindering solute transport by liquid flow in the mushy zone. Quantitative comparisons between simulated and measured composition profiles shows that the "sponge-like" model [9] for the mechanical behavior of the mushy zone and the proposed "two-phase" numerical resolution [10,11] constitute a step forward on modeling deformation-induced macrosegregation during steel casting processes by combining coupled phenomena. This work constitutes the first validation of modeling efforts started in the sixties [1] to describe the role of thermomechanical deformation on the formation of macrosegregation. The various existing models developed for steels [6–9,12–18] lack the effective coupling between solid deformation and fluid flow demonstrated in the present contribution.

However, the intensity of the predicted macrosegregation remains lower than the one measured in reality. Through the discussion of the results and in the light of sensitivity tests, it appears that the observed differences are mainly due to the type of microsegregation model and to the constitutive model and parameters controlling the compression of the solid phase in the mushy zone. Regarding the first point, the sole lever rule has been used in the present study. The use of the Gulliver-Scheil or alternative microsegregation models could increase the intensity of calculated macrosegregation. As for the mechanics of the mushy zone, the identification of compressibility parameters by separate elementary rheological tests appears to be essential as they also influence significantly the intensity of macrosegregation.

Macrosegregation remains the main defect to be controlled during CC. The present contribution reports efforts to reach quantitative prediction. Regarding applicability to steel continuous casting, it was already shown to be effective in 2D and for a binary alloy, allowing the analysis of soft reduction operations carried out on steel slabs at the end of the secondary cooling zone [11]. In addition to the implementation of better microsegregation models, extension to 3D analysis is necessary to address the continuous casting of long products, such as billets or blooms, or to capture with better accuracy edge effects, e.g. close to the two lateral narrow faces in the case of slabs. The achievement of such models is of paramount importance for the understanding and control of the formation of central macrosegregation. It is expected that enhanced modeling capabilities will benefit optimization of current industrial practices by increasing yield through reducing macrosegregation defects. Achieving more quantitative modeling of macrosegregation and other defects (e.g., hot tearing [19]), has also potential for exploring numerically routes to cast high-alloyed steels with various grades and to reduce the time to production of new alloys.

References

[1] M. Flemings, G. Nereo, Macrosegregation: Part I, Trans. Metall. Soc. AIME 239 (1967) 1449–1461.
[2] M. Wu, A. Ludwig, A three-phase model for mixed columnar-equiaxed solidification, Metall. Mater. Trans. A 37 (2006) 1613–1631.
[3] J. Li, M. Wu, A. Ludwig, A. Kharicha, Simulation of macrosegregation in a 2.45-ton steel ingot using a three-phase mixed columnar-equiaxed model, Int. J. Heat Mass Transf. 72 (2014) 668–679.
[4] M. Založnik, H. Combeau, An operator splitting scheme for coupling macroscopic transport and grain growth in a two-phase multiscale solidification model: Part I – model and solution scheme, Comput. Mater. Sci. 48 (2010) 1–10.
[5] T.-T.-M. Nguyen, H. Combeau, M. Založnik, M. Bellet, Ch.-A. Gandin, Multiscale finite element modelling of solidification structures by a splitting method taking into account the transport of equiaxed grains, in: H. Yasuda (Ed.), Proc. MCWASP XIV, 14th Int. Conf. on Modeling of Casting, Welding and Advanced Solidification Processes, Awaji Island, Japan, 21-26 June 2015, IOP Conference Series: Materials Science and Engineering, vol. 84, 2015 article 012007, 10 pages.
[6] K. Miyazawa, K. Schwerdtfeger, Macrosegregation in continuously cast steel slab: preliminary theoretical investigation on the effect of steady state bulging, Arch. Eisenhuttenwes 52 (1981) 415–422.
[7] T. Kajitani, J.M. Drezet, M. Rappaz, Numerical simulation of deformation induced segregation in continuous casting of steel, Metall. Mater. Trans. A 32 (2001) 1479–1491.
[8] J. Domitner, M. Wu, A. Kharicha, A. Ludwig, B. Kaufmann, J. Reiter, T. Schaden, Modeling the effects of strand surface bulging and mechanical soft reduction on the macrosegregation formation in steel continuous casting, Metall. Mater. Trans. A 45 (2014) 1415–1434.
[9] G. Lesoult, Ch.-A. Gandin, N.T. Niane, Segregation during solidification with spongy deformation of the mushy zone, Acta Mater. 51 (2003) 5263–5283.
[10] V.D. Fachinotti, S. Le Corre, N. Triolet, M. Bobadilla, M. Bellet, Two-phase thermo-mechanical and macrosegregation modelling of binary alloys solidification with emphasis on the secondary cooling stage of steel slab continuous casting processes, Int. J. Num. Methods. Eng. 67 (2006) 1341–1384.
[11] M. Bellet, A two-phase 2D finite element model for macrosegregation in steel continuous casting, in: H. Jones (Ed.), Proceedings of the 5th Decennial Int. Conf. on Solidification Processing, The University of Sheffield, Sheffield, United Kingdom, 2007, pp. 424–427.
[12] B. Rivaux, Modélisation multi - échelle des structures de grains et des ségrégations dans les alliages métalliques, Ph.D. Thesis, MINES ParisTech, Paris, France, 2011.
[13] H. Sato, T. Kitagawa, K. Murakami, T. Kawawa, Tetsu Hagane 61 (1975) S471.
[14] K. Miyamura, A. Ochi, K. Kanamaru, N. Kaneko, Tetsu Hagane 62 (1976) S482.
[15] K. Marukawa, M. Kawasaki, T. Kimura, S. Ishimura, Tetsu Hagane 64 (1978) S661.
[16] K. Narita, T. Mori, K. Ayata, J. Miyazaki, M. Fujimaki, Tetsu Hagane 64 (1978) S152.
[17] Y. Sugitani, M. Nakamura, H. Kawashima, M. Kawasaki, Tetsu Hagane 66 (1980) S193.
[18] M. Wintz, M. Bobadilla, M. Jolivet, Hot cracking during solidification of steels - effect of carbon, sulphur and phosphorus, La Rev. Métall. 4 (1994) 105–114.
[19] T. Koshikawa, M. Bellet, Ch.-A. Gandin, H. Yamamura, M. Bobadilla, Metall. Mater. Trans. 47A (2016) 4053–4067.
[20] J. Ni, C. Beckermann, A volume-averaged two-phase model for transport phenomena during solidification, Metall. Mater. Trans. B 22 (1991) 349–361.
[21] M. Bellet, V.D. Fachinotti, ALE method for solidification modelling, Comput. Methods. Appl. Mech. Eng. 193 (2004) 4355–4381.
[22] M. Bellet, O. Jaouen, I. Poitrault, An ALE-FEM approach to the thermo-mechanics of solidification processes with application to the prediction of pipe shrinkage, Int. J. Num. Methods. Heat. Fluid Flow 15 (2005) 120–142.
[23] P. Shi, TCS Steels/Fe-alloys Database V6.0, Thermo-Calc Software AB, Stockholm, Sweden, 2008.
[24] Thermo-Calc, TCCS Manuals, Thermo-Calc software AB, Stockholm, Sweden, 2013.
[25] Iron and Steel Institute of Japan, Mechanical Behavior in Continuous Casting, ISIJ, 1985. NCID: BN03702225 (Citation Information by National institute of informatics: CiNii).
[26] A. Palmaers, A. Etienne, J. Mignon, Calculation of the mechanical and thermal stresses in continuously cast strands, Stahl Eisen 99 (1979) 1039–1050.
[27] British Iron and Steel Research Association, Physical Constants of Some Commercial Steels at Elevated Temperatures (Based on Measurements Made at the National Physical Laboratory, Teddington, United Kingdom), Butterworths Scientific Publications, London, United Kingdom, 1953.
[28] J.A. Dantzig, M. Rappaz, Solidification, EPFL Press, 2009.
[29] T. Koshikawa, C.A. Gandin, M. Bellet, H. Yamamura, M. Bobadilla, Computation of phase transformation paths in steels by a combination of the partial- and para-equilibrium thermodynamic approximations, ISIJ Int. 54 (2014) 1274–1282.

Chapter V
Summary of the main results

1. Summary on microsegregation modelling

As presented in Chapter II, a numerical scheme concerning microsegregation model for a general cooling sequence during solidification has been developed. Several combinations of the above approximations are possible:

- Lever Rule (LR). It obviously corresponds to full thermodynamic equilibrium transformation paths and may be applied from a temperature higher than the liquidus temperature up to room temperature.
- Gulliver Scheil (GS). All interstitial and substitutional elements in all solid phases are "frozen", not permitting the peritectic reaction to take place. Because such approximation is difficult to maintain up to low temperature, a critical fraction of liquid (10^{-6}) is chosen to stop the transformation, below which the average composition of all phases is kept constant.
- Partial Equilibrium (PE). Considered alone, it considers full equilibrium for interstitials while substitutional elements are "frozen". This does change the solidification path compared to GS, yet still not permitting the peritectic reaction to occur.
- Partial Equilibrium plus Lever Rule (PE+LR). It keeps the PE approximation while handling the peritectic reaction by using a simple LR approximation among the δ-BCC and γ-FCC solid phases [Chen 2006]. Note that the γ-FCC to α-BCC solid state transformation is also considered in such situation.
- Partial Equilibrium plus Para Equilibrium (PE+PA). This is the most advanced configuration where the δ-BCC to γ-FCC peritectic transformation and the γ-FCC to α-BCC solid state transformation are both considered.

It is applied to multicomponent steels. Analyses include

- unidirectional solidification experiment conducted for Fe-C-Mn-S-Si-P-Al steels,
- microstructure investigation with image analyses at certain section perpendicular to withdrawal direction in which one can distinguish the remaining liquid quenched into a fine microstructure from the solid phase formed before quenching,
- Electron Probe Micro-Analysis (EPMA) on a steel sample from the centre of a 450 kg ingot casting (0.5 m width, 0.16 m thickness and 0.75 m height),
- a numerical scheme for Lever Rule (LR), Gulliver-Scheil (GS), Partial Equilibrium (PE), Para Equilibrium (PA) and combination of PE+LR and PE+PA with Thermocalc and the database TCFE6,
- Computation of transformation paths for two experiments.

Main findings are as follows:

1- A new combination of the Partial- and Para- Equilibrium (PE+PA) thermodynamic approximations is proposed for the study of phase transformations in steels, from the liquid state to room temperature.

2- Calculated solidification paths for multi-component alloys are discussed with respect to the peritectic transformation. It is found that, in case of PE+PA, the solidification path does not differ significantly from PE+LR approximations.

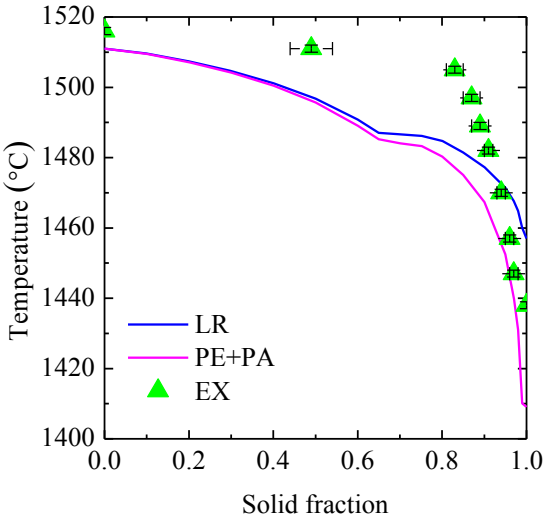

Figure 1 *Three solidification paths for targeted alloy composition, shown in Table 1 corresponding to (blue curve, LR) the Lever Rule approximation, (red curve, PE+PA) a combination of Partial Equilibrium and Para Equilibrium approximations and (green marks with error bars, EX) Experimental investigation.*

3- Differences with experimental results are discussed based on analyses of a sample processed by Bridgman solidification, showing the need for more accurate experimental results and removal of several modeling hypotheses (absence of microstructures kinetics and no treatment of limited diffusion in all phases).
4- Regarding the solid state phase transformations, PE+PA is found to provide the most realistic composition profile of substitutional elements and evolution of the phase fractions. PE+PA is therefore recommended as the standard set of thermodynamic approximations to be used for the study of phase transformations in multicomponent steels.

The obtained solidification path is shown in Figure 1. It shows how the solidification interval is modified by the various thermodynamic approximations. As a consequence, the Brittle Temperature Range (BTR), defined where fraction of solid increases from 0.9 to 0.99, is significantly changed as given in *Table 2*. As the BTR also refers to the solidification interval during which strain accumulates up to form the hot crack criterion, it is used for hot tearing modeling.

Table 1. *Target compositions and experimental conditions.*

Article I.	Composition (mass%)						Displace-ment	Velocity
	C	Si	Mn	P	S	Al	(mm)	(mm s^{-1})
Target	0.21	0.24	1.64	0.032	0.007	0.090	3 to 6	0.25 to 2.0

Table 2. *Extent of the brittleness temperature range (BTR) calculated with (LR) the Lever Rule approximation, (PE+PA) the Partial- plus Para-Equilibrium approximation and (EX) deduced from measurements. The corresponding solidification paths and exact alloy composition are reported in Figure 1.*

	LR	PE+PA	EX
BTR extent (K)	17.2	57.3	44.5

2. Summary on hot tearing prediction

As presented in Chapter III, a hot tearing study is performed during steel solidification with ingot punch pressing test. A schematic of the test is shown in Figure 2. It has been designed to mimic the thermomechanical solicitations taking place during CC processing of steel; for instance, with respect to the evolution of the cooling rate and deformation. The size of the ingot is 0.75 m height, 0.5 m width and 0.16 m thick. Its mass is approximately 450 kg. At a precise time after filling, the upper part of one mold part that define the two largest ingot surfaces (a top right mold part in Figure 2) is moved upward. The lateral surface of the ingot is then in direct contact with the air. Note in Figure 2 that this side of the mold is made of two parts positioned one on top of the other. The bottom part could thus be kept at the same place while the top part is removed. A punching tool is then put into contact with the lateral vertical free surface of the ingot. It consists of a horizontal 0.12 m-diameter 0.3 m-long cylinder with length centered on the main vertical face of the ingot, its longitudinal axis aligned with the Z direction at height 0.45 m from the bottom of the ingot. The tool velocity and displacement are controlled by means of a hydraulic system and recorded during the test. The reaction force is also measured using the time evolution of the hydraulic system pressure. The nominal composition is measured in the ladle before filling and is reported in Table 1.

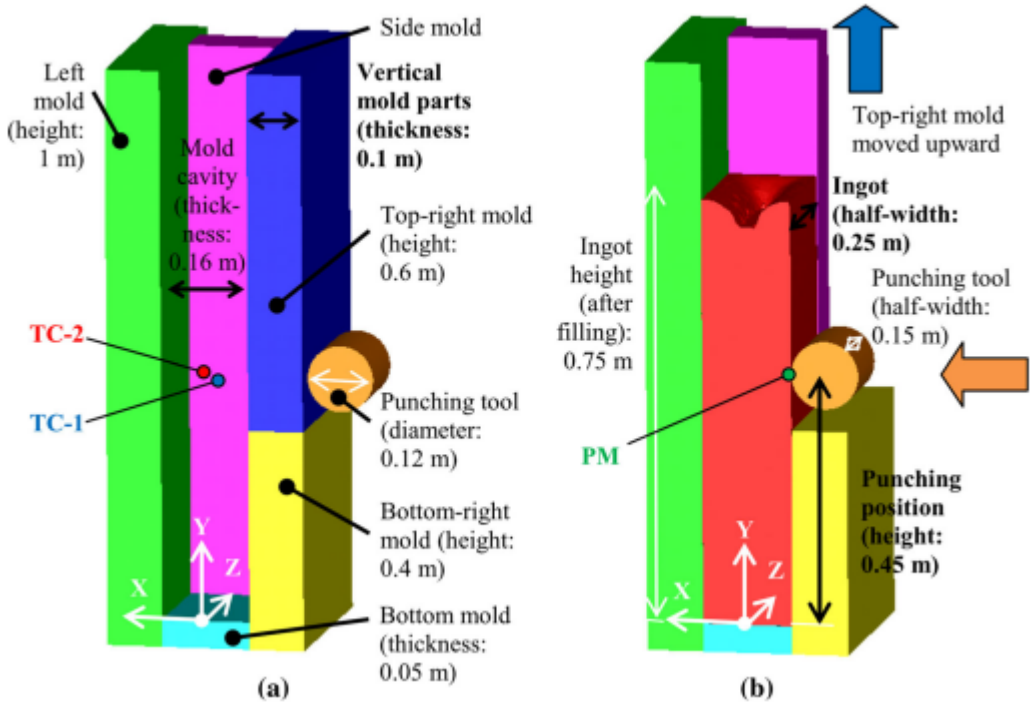

Figure 2. *Schematic of half of the hot tearing experiment setup developed at Nippon Steel & Sumitomo Metal Corporation showing configuration (a) prior to the filling stage and (b) at the onset of the punching stage after filling, partial solidification with the mold configuration shown in (a), removal of the top-right mold and horizontal displacement of the cylindrical punching tool to come into contact with the ingot. The coordinate system is defined in (a). The Y = 0 m plane is defined by the top surface of the bottom mold part, also defining the lowest ingot surface in (b). The Y-axis, opposite to the gravity vector, is directed toward the top of the ingot at mid-width and mid-thickness. The X-axis is directed toward the fixed left-mold surface. Thermocouples, TC-1 and TC-2 are located at (X, Y, Z) positions (0, 0.43, 0.06) m and (0.02, 0.43, 0.16) m, respectively. As schematized, measurement is also performed with a pyrometer (PM) around the punched surface of the ingot, before and after punching.*

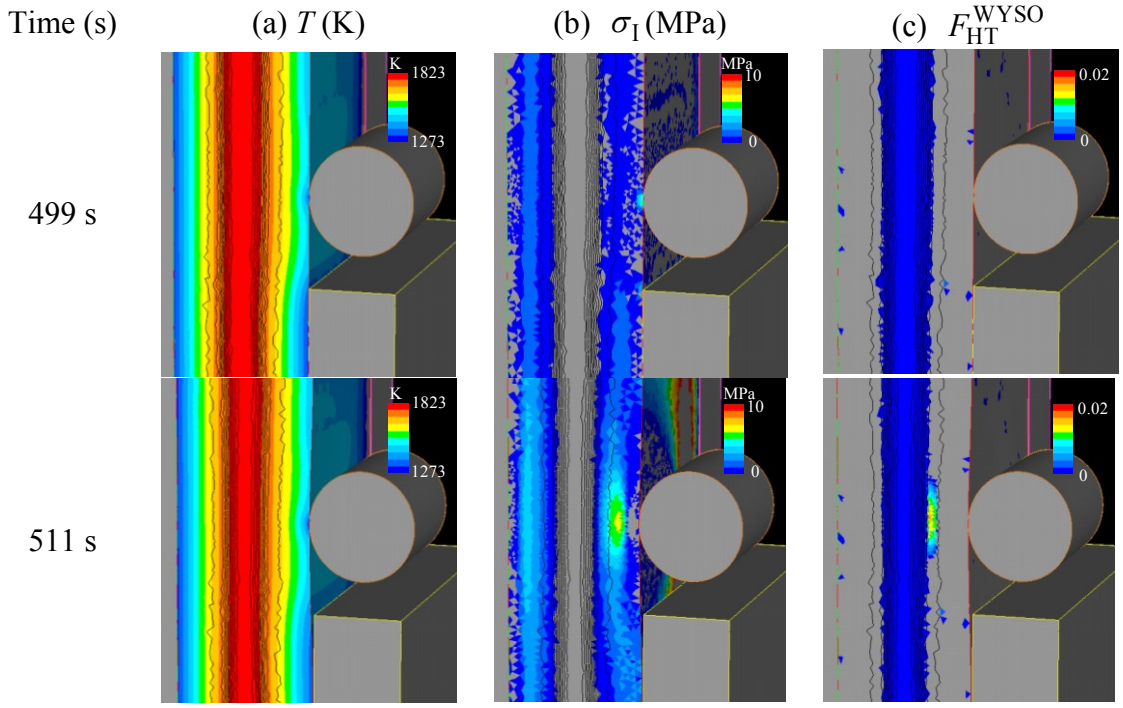

Figure 3. Predicted results for one of the tests with the PE+PA solidification path (Figure 1) showing (a) the temperature field, (b) the regions with positive values of the first principal stress, i.e. under tension, the grey regions within the ingot being under compression, and (c) the hot tearing criterion F_{HT}^{WYSO}*. The top and bottom lines show the different fields just before (499 s) and after (511 s) punching, respectively. Black vertical lines indicate iso-liquid fraction contours from 0 to 1 with 0.1 step.*

Main findings are as follows:

- the HTC is able to predict the risk of crack formation, provided that the brittleness temperature range (BTR) is adequately reproduced,
- excellent correlation is found between measurements and simulations concerning the position shown in Figure 4 which is based on 3D thermomechanical simulation shown in Figure 3,
- the role of the BTR is evidenced when drawing the HTC profile along the ingot thickness shown in Figure 4, thus revealing the critical effect of the selected solidification path,
- predictions in a cumulated strain versus strain rate perpendicular to the temperature gradient, as well as the reaction force, does not evidence large variation with the BTR shown in Figure 5, nor does the thermal history,

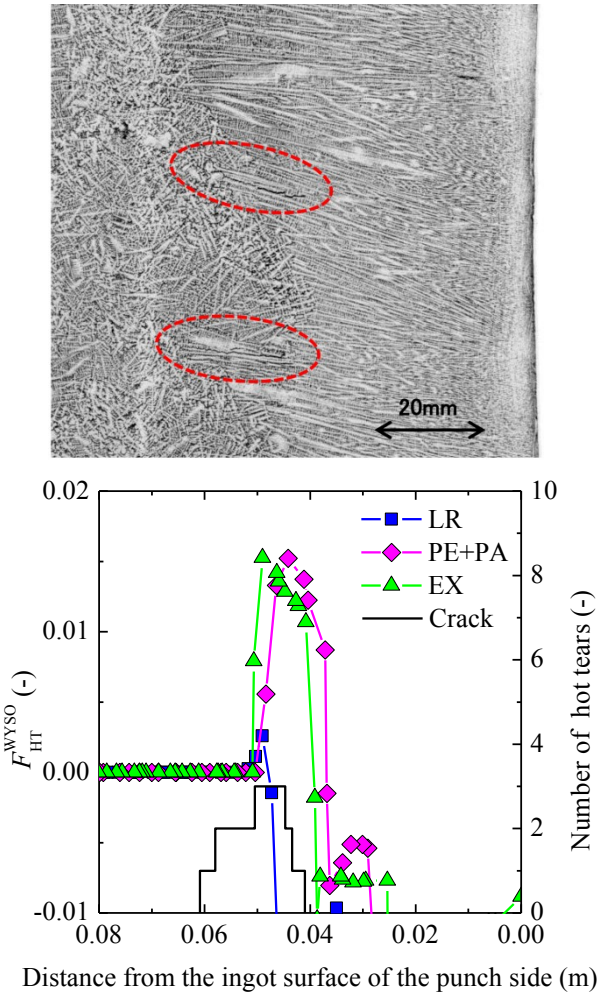

Figure 4. *Magnified micrograph for one of the tests on the top. In all cases, hot tears are observed and circled with dashed red contours. Also, the view being limited, not all cracks found are shown. Profiles along the ingot thickness for (black curve, right-hand-side legend) the number of hot tears and (colored curves, left-hand-side legend) the hot tearing criterion* F_{HT}^{WYSO} *on the bottom. Results are presented as a function of the 3 solidification paths presented in Figure 1.*

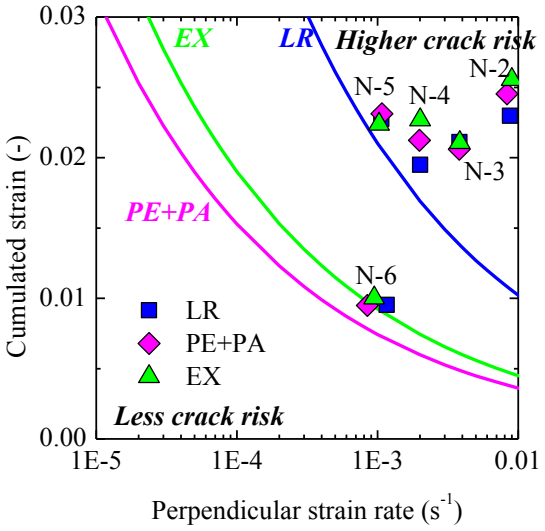

Figure 5 *Computed cumulated strain* $\int_{BTR} \dot{\hat{\varepsilon}}\,dt$ *as a function of the strain rate* $\dot{\hat{\varepsilon}}$ *perpendicular to the temperature gradient calculated when passing through the BTR. Values for the different tests are taken from the* F_{HT}^{WYSO} *profile at the punching height, an example being shown in* ***Figure*** *4. The three continuous curves indicate the strain limit* $\hat{\varepsilon}_c$ *(Chapter III Eq. (13)). BTR effect is clearly seen as the three strain limit curves, whereas the obtained cumulated strain as a function of the strain rate is not so different in each other with the same test case.*

3. Summary on macrosegregation calculation

As presented in Chapter IV, a macrosegregation calculation has been carried out during steel solidification with ingot punch pressing test. The detail of the test is explained in the previous section. The ingot punch pressing test has been developed to better understand the phenomena influencing the solid shell and the central mushy zone of steel semi-products when crossing the secondary cooling section during continuous casting. The test consists of the punching of one side of the solid shell of a partially solidified ingot, by an external tool. The study is now focused on the macrosegregation which is induced by this punching operation. The deformations of the solid shell and of the central mushy zone are simulated numerically, using a 2D finite element method. The mechanics of the mushy zone is addressed by a "two-phase" approach, in which the compressible deformation of the solid phase and the liquid flow are solved concurrently, as they are in close interaction.

The thermo mechanical simulation results (*Figure 6*) show the deformation of the solid phase and the associated liquid flow, as calculated in the "two-phase" approach for the simulation of one of these tests. The deformation of the solid shell by the punch induces a compression of the solid phase in the mushy zone (not visible in *Figure 6*), which in turn induces liquid flow. For evident reasons (global quasi incompressibility of the mushy material, closed mushy pool at the bottom of the ingot), liquid flow is necessarily oriented upward. In this precise test, solidification is less advanced: the alloy is still in the mushy state in its top central region. This makes possible such an upward liquid flow, with liquid expulsion at the top surface into the primary shrinkage cavity: the expelled melt covers the already formed solid shell. The simulated liquid flow can be seen in the central part of *Figure 6*. Experimental evidence of such an expulsion of liquid flow is provided by the micrograph on the right part of the figure, in which a residue of enriched (darker) expelled liquid is present at the bottom of the V-shape shrinkage cavity. The similarity of the shape of the primary shrinkage cavity can be noted between the simulation and the micrograph, expressing the good representativity of the thermo-mechanical simulation.

Figure 7 reveals in more details what happens in the mushy zone at the height of the punch tool. Due to the motion of the punching tool, the solid shell in its vicinity is displaced as shown by the horizontal component of the solid velocity (Figure 7(a)). The resulting compression of the solid phase within the mushy zone is expressed by negative values of the divergence of the solid velocity field, $\nabla \cdot \mathbf{v}_s$, displayed in Figure 7(b). A relative liquid flow is thus created as shown in Figure 7(c). The compression of the solid phase primarily affects the regions of the mush for which the liquid fraction is higher than 0.1. Indeed, when liquid fraction decreases, the compressibility of the solid phase decreases as well, tending towards a fully dense solid material. This hinders the compression of the solid phase at the periphery of the mushy zone, where solidification is more advanced.

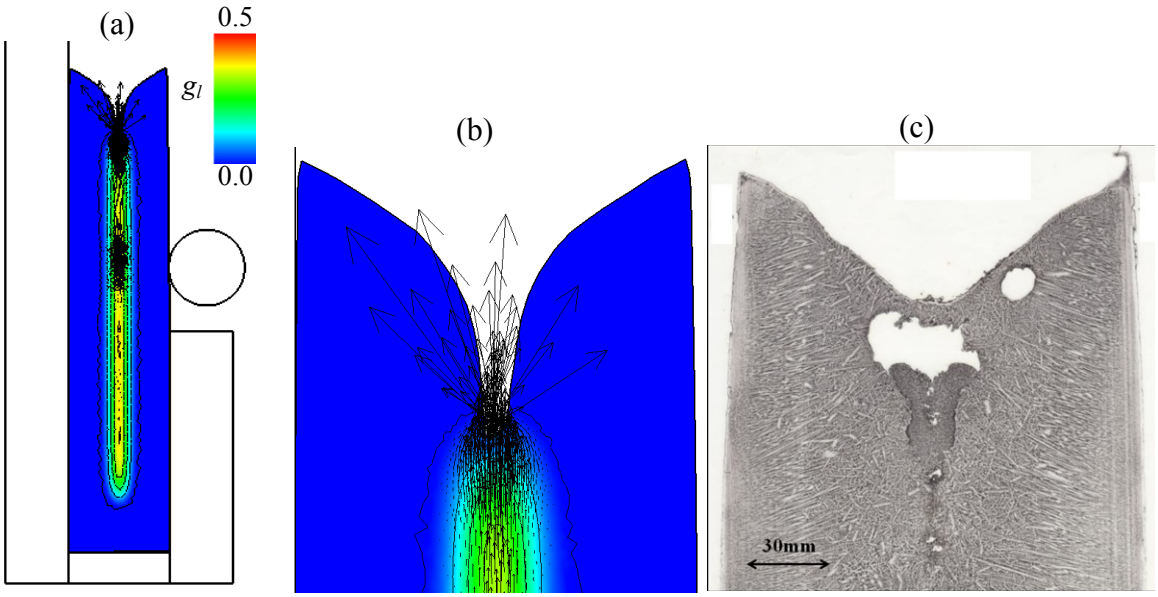

Figure 6. *Simulated and observed ingot shape showing (a) a global view of the deformation and distribution of solidification in the 0.16 m width ingot section at time 792.4 s (0.4 s after punch start) for one of the trials studied and (b) a zoom in the top region with shrinkage pipe to be compared with (c) observation. The simulation also shows (color map) the distribution of the liquid fraction and (black contours) isofractions of liquid, as well as (arrows) the relative velocity of the liquid phase with respect to the solid one,* $\mathbf{v}_l - \mathbf{v}_s$*. The darker region at the center of the micrograph is due to expellation of liquid in the primary shrinkage cavity as a result of punching.*

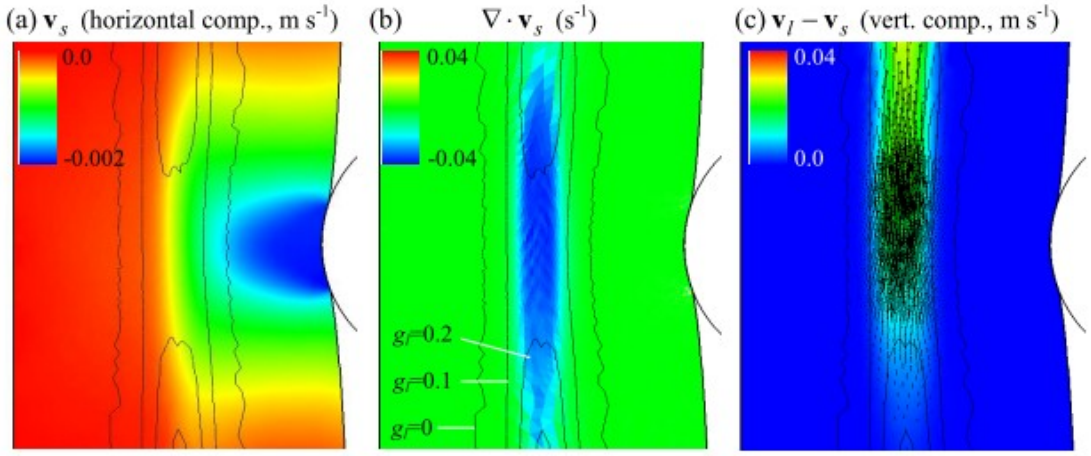

Figure 7. *Central region of ingot, 6 s after punch start, showing (a) the distribution of the horizontal component of the velocity of the solid phase* $\mathbf{v}_s$*, (b)* $\nabla \cdot \mathbf{v}_s$ *with evidence of negative values in the mushy zone at the height of the punch tool and (c) the vertical component of the relative velocity of the liquid phase with respect to the solid one,* $\mathbf{v}_l - \mathbf{v}_s$*. The simulation also shows (black contours) isofractions of liquid, from 0 to 0.3, and (arrows) the vector field* $\mathbf{v}_l - \mathbf{v}_s$*.*

Two experimental tests are considered, consisting of two ingots of the same steel grade, but punched at different instants, that is for two different advancements of their solidification. As shown in *Figure 8*, the "two-phase" finite element simulation is able to account for the essential driving forces for induced macrosegregation. The general trends are reproduced: formation of a negative macrosegregation in one ingot only, which only affects the superior part of the central region of the ingot. This illustrates the

relevance of the "sponge-like" model for the mechanical behavior of the mushy zone and of the proposed "two-phase" numerical resolution.

However, the intensity of the predicted macrosegregation remains significantly lower than the one measured in reality. Through the discussion of the results and in the light of some sensitivity tests, it appears that the observed differences are mainly due to the type of microsegregation model and to the constitutive model and parameters controlling the compression of the solid phase in the mushy zone. Regarding the first point, the sole lever rule has been used in the present study. The use of the Gulliver-Scheil or alternative microsegregation models could increase the intensity of calculated macrosegregation. As for the mechanics of the mushy zone, the identification of compressibility parameters by separate elementary rheological tests appears to be essential as they also influence significantly the intensity of macrosegregation.

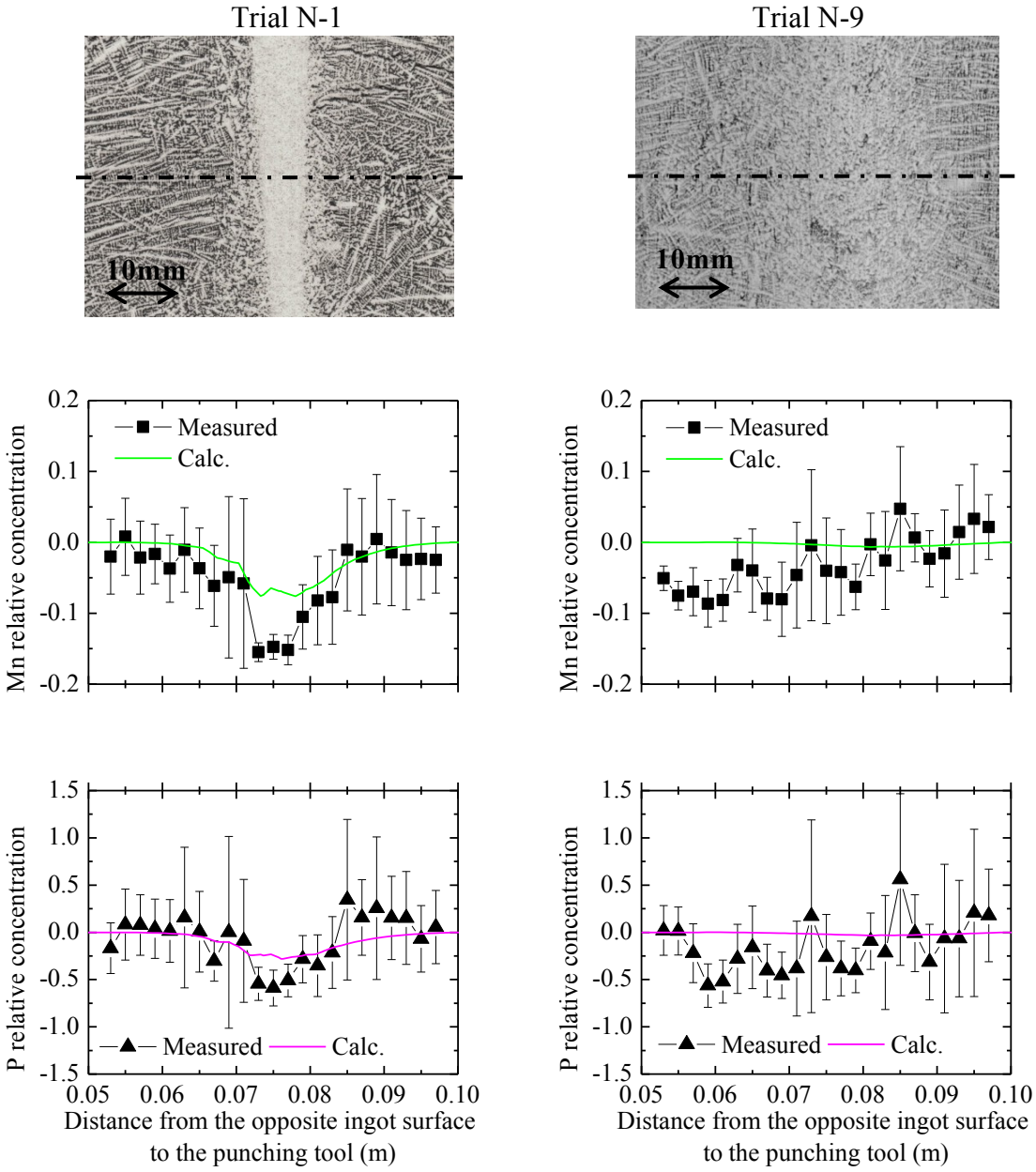

Figure 8 *Comparison of calculated and measured segregation profiles in cases N-1 and N-9 (left and right parts of the figure, respectively). The top line shows two micrographs at punch height. The two bottom lines show the relative variation in concentration for Mn and P, respectively:* $(\langle w_i \rangle - w_{i0})/w_{i0}$, *where* w_{i0} *stands for the nominal initial composition in solute i (Mn or P). Profiles are plotted through the thickness of the ingot, at punch height, the mid-section after punching being around 75 mm from the ingot surface opposite to the punching side. EPMA measurements are indicated by black squares and triangles, while continuous curves are for finite element calculations. Error bars indicate standard deviations.*

Chapter VI
Perspectives and recommendation for future work

1. Perspectives on microsegregation modeling

As discussed in Chapter III and IV, microsegregation modeling is quite important for hot tearing prediction and macrosegregation calculation. Concerning hot tearing prediction, the criterion used in Chapter III is based on the Brittle Temperature Range (BTR) and the strain rate perpendicular to the columnar growth. The BTR is directly linked to the microsegregation modeling and the choice of a microsegregation model has an impact on the hot tearing prediction. In fact, LR is shown to decrease the value of the hot tearing criterion compared to the other microsegregation modeling cases. In addition, hot tearing taking place for solid fractions over 0.9, the accuracy of the final part of the solidification path is then important to predict the position of cracks. Regarding macrosegregation calculation, microsegregation modeling makes difference on segregation intensity in the solid and the liquid phases. Because of the deformation of the mushy solid, the enriched melt is circulated with solute elements so that macrosegregation intensity is increased. Another impact of microsegregation modeling is solidification interval. When solidification interval is larger, the mushy state is maintained over a longer time. In the CC process, this may induce an overestimation of the risk of hot tearing due to longer solidification interval. This is why microsegregation modeling is quite important. This should motivate further investigation with respect to experiments for solidification path, liquidus, solidus and the other phase transformation critical temperatures. With such data, more sophisticated microsegregation models could be developed with consideration to finite solute diffusion and undercooling effect.

2. Perspectives on hot tearing prediction

As discussed in the article in Chapter III, considering the strong sensitivity of the hot tearing prediction to the solidification path, coupling with macrosegregation has to be modelled. Indeed, deformation induced composition variations are expected to generate variations in solidification paths. This is particularly true when considering alloying elements such as C, S or P for which low concentration variations can generate large deviations of the solidus temperature. The numerical modelling of this coupling with macrosegregation requires in turn the calculation in the mushy zone of the concurrent deformation of the solid phase and liquid flow. Some work has been initiated by the authors by use of a two-dimensional "two-phase" thermomechanical model. However, a general 3D framework implementing concurrently macrosegregation *and* hot tearing is still missing in the literature. Further developments in this direction are foreseen.

Another perspective is the application to real CC process with $F_{\mathrm{HT}}^{\mathrm{WYSO}}$. The objective would be to analyze the effect on the hot tearing criterion (and thus on cracking risk) of process parameters such as secondary cooling pattern, casting velocity etc. This could help us understand how to optimize operating parameters for a given steel grade and how to modify CC configuration (roll pitch, bending and unbending radius etc) in order to improve productivity and develop CC-routes for new steel grades in a couple of years.

3. Perspectives on macrosegregation calculation

As discussed in the article in Chapter IV, it will be interesting to address real CC situation in the future. Indeed, the experimental result obtained for the ingot punching test showed negative macrosegregation but the reality is that a positive macrosegregation is mainly observed at the centre of the slab thickness. This would require to model CC in 3D with the two phase approach with a change of steel composition, secondary cooling pattern, casting velocity and an application of soft reduction process with a change of soft reduction ratio. Prior such an application, it is mandatory to develop the microsegregation model to take into account a Gulliver Scheil microsegregation model, or para and partial equilibrium combination model or a more sophisticated model. A general 3D framework is also required since macrosegregation is varied not only in the casting and thickness directions but also in the slab width direction.

In addition, the mechanical behavior of the solid in the solidification interval should be more investigated. As discussed in the article, rheological parameters attached to behavior laws of the solid phase have an impact on the amplitude of negative macrosegregation. In order to investigate the rheological parameters of semi-solid material, in-situ observation using synchrotron X-ray tomography is one of the helpful tools. Recently, In-situ observation on semi-solid deformation is studied by some researchers [Cai 2015, Morita 2015]. It is proposed to develop a combination between observation results and modeling for semi-solid deformation. In the experiment, the semi-solid deformation is recorded and the initial state can be transferred to finite element mesh for a numerical study [Zaragocci 2012]. One can measure the applied force and displacement to deform the semi-solid specimen so that the numerical model can be validated, leading to determination of reliable rheological parameters. It is worth noting that inverse method [Pradille 2011] could help in the determination of the

parameters.

4. Conclusion and future work

It can be foreseen that the next 5 to 10 years could show some significant progress in the modeling of such difficult issues in the context of the industrial steel CC. That would certainly contribute to a more efficient and valuable production of new generation steels (involving new alloying elements, higher compounds) for application in various industrial sectors. We hope our work will have contributed to knowledge building and software development that are absolutely essential in such developments.

References

[Bellet 2004] M. Bellet and V.D. Fachinotti: Comput. Meth. Appl. Mech. Eng., 2004, vol. 193, pp. 4355-4381
[Bellet 2005] M. Bellet, O. Jaouen and I. Poitrault: Int. J. Num. Meth. Heat Fluid Flow, 2005, vol. 15, pp. 120-142
[Bellet 2007] M. Bellet: Proc. SP07, 5th Decennial Int. Conf. on Solidification Processing, Sheffield, 23-25 July 2007, H. Jones (ed.), The University of Sheffield, 2007, pp. 424-427
[Bellet 2009] M. Bellet, O. Cerri, M. Bobadilla and Y. Chastel: *Metall. Mater. Trans. A, 2009, vol. 40, pp. 2705-2717*
[Braccini 2000] M. Braccini: Doctoral Thesis, Institut National Polytechnique de Grenoble, 2000.
[Brimacombe 1977] J. K. Brimacombe and K. Sorimachi, "Crack Formation in the Continuous Casting of Steel", Metall. Trans. B, 1977, vol. 8B, pp. 489-505.
[Cai 2015] B. Cai, S. Karagadde, T.J. Connolley and P.D. Lee : Proc. MCWASP XIV, 14th Int. Conf. on Modelling of Casting, Welding and Advanced Solidification Processes, Hyogo (Japan), June 21-26, 2015, H. Yasuda (eds.), IOP Conference Series 84 (2015) 012079, 8 pages
[Carozzani 2012] T. Carozzani: Ph.D. Thesis, Mines ParisTech, 2012
[Cerri 2007] O. Cerri: Ph.D. Thesis, Mines ParisTech, 2007
[Chen 2002] Q. Chen and B. Sundman: Mater. Trans., **43**(2002), 551.
[Chen 2006] Q. Chen, A. Engstrom, X.-G. Lu and B. Sundman: MCWASP-XI, Ch.-A. Gandin and M. Bellet eds., TMS (2006) 529.
[Clyne 1977] T.W. Clyne and G.J. Davies: Solidification and Casting of Metals, TMS, Warrendale, PA, 1977, pp. 275-278
[Eskin 2004] D. G. Eskin, Suyitno and L. Katgerman: Progress in Material Science, Vol. 49, 2004, pp. 629-711.
[Fachinotti 2006] V.D. Fachinotti, S. Le Corre, N. Triolet, M. Bobadilla and M. Bellet: Int. J. Num. Meth. Eng., 2006, vol. 67, pp. 1341-1384
[FLUENT] http://www.ansys.com/Products/Fluids/ANSYS-Fluent
[Fredriksson 1979] H. Fredriksson and B. Lehtinen: Solidification and Casting of Metals, 1979, pp. 260-267.
[Gerds 1976] A. F. Gerds, E. M. Stein, E. E. Fletcher and A. R. Elsea: Steel Founders' Society of America, 1976.
[Gulliver 1913] GH. Gulliver: J Inst Metals, **9**(1913), 120.
[Hillert 1998] M. Hillert: Phase Equilibria, Phase Diagrams and Phase Transformations, Cambridge University (1998), p.358.

[Kajitani 2001] T. Kajitani, J. M. Drezet and M. Rappaz: Metall. Mater. Trans. A, 2001, vol. 32, pp. 1479-1491
[Katayama 1985] S. Katayama, A. Matsunawa and T. Fujimoto: Transaction of JWRI, Vol. 14, No. 1, 1985.
[Kotecki 1993] D. J. Kotecki: Welding of Stainless Steel, ASM Handbook, Vol.6, 1993, pp. 677-707.
[Lankford 1972] W. T. Lankford, "Some Considerations of Strength and Ductility in the Continuous-Casting Process", *Metall. Trans.*, 1972, vol. 3, pp. 1331-1357.
[Ludwig 2004] O. Ludwig: Doctoral Thesis, Institut National Polytechnique de Grenoble, 2004.
[Marukawa 1978] K. Marukawa, M. Kawasaki, T. Kimura and S. Ishimura: Tetsu to Hagane, 1978, vol. 64 S661
[Mayer 2010] F. Mayer, M. Wu and A. Ludwig: Steel research Int., 2010, vol. 81, No. 8, pp. 660-667
[Miyamura 1976] K. Miyamura, A. Ochi, K. Kanamaru and N. Kaneko: Tetsu to Hagane, 1976, vol. 62, S482
[Miyazawa 1981] K. Miyazawa and K. Schwerdtfeger: Arch. Eisenhuttenwes, 1981, vol. 52, pp. 415-422
[Morita 2015] S. Morita, H. Yasuda, T. Nagira, C.M. Gourlay, K. Morishita, M. Yoshiya and A. Sugiyama : Proc. MCWASP XIV, 14th Int. Conf. on Modelling of Casting, Welding and Advanced Solidification Processes, Hyogo (Japan), June 21-26, 2015, H. Yasuda (eds.), IOP Conference Series 84 (2015) 012011, 8 pages
[Nagata 1990] S. Nagata, T. Matsumiya, K. Ozawa and T. Ohashi: *ISIJ Int, 1990, vol. 76 (2), pp. 214-221*
[Narita 1978] K. Narita, T. Mori, K. Ayata, J. Miyazaki and M. Fujimaki: Tetsu to Hagane, 1978, vol. 64, S152
[Ni 1991] J. Ni, C. Beckermann, A volume-averaged two-phase model for transport phenomena during solidification, Metall. Mater. Trans. B 22 (1991) 349-361.
[Okumura 1994] H. Okumura, "Recent Trends and Future Prospects of Continuous Casting Technology", Nippon Steel Technical Report, 1994, No. 61, pp. 9-14.
[Phillion 2008] A.B. Phillion, S.L. Cockcroft and P.D. Lee: Acta Mater., 2008, vol. 56, pp. 4328-4338
[Pierer 2007] R. Pierer, C. Bernhard and C. Chimani : La Revue de Métallurgie, 2007, vol. 2, pp. 72-83
[Pradille 2011] C. Pradille: Ph.D. Thesis, Mines ParisTech, 2011

[Prokhorov 1962] N.N. Prokhorov: *Russian Castings Production, 1962, vol. 2, pp. 172-175*
[Rappaz 1999] M. Rappaz, J.M. Drezet and M. Gremaud: Metall. Mater. Trans. A, 1999, vol. 30, pp. 449-456
[Rivaux 2011] B. Rivaux: Ph.D. Thesis, Mines ParisTech, 2011
[Rogberg 1983] B. Rogberg: *Scand. J. Metall., 1983, vol. 12, pp. 51-66*
[Saad 2016] A. Saad: Ph.D. Thesis, Mines ParisTech, 2016
[Sato 1975] H. Sato, T. Kitagawa, K. Murakami and T. Kawawa: Tetsu to Hagane, 1975, vol. 61, S471
[Scheil 1942] E. Scheil: Zeitschrift für Metallkunde, **34**(1942), 70.
[Shi 2008] P. Shi: TCS steels/Fe-alloys database V6.0 Thermo-Calc Software AB (Stockholm, SE), (2008).
[Sistaninia 2011] M. Sistaninia, A.B. Phillion, J.M. Drezet and M. Rappaz : Metall. Mater. Trans. A, 2011, vol. 42, pp. 239-248
[Sugitani 1980] Y. Sugitani, M. Nakamura, H. Kawashima and M. Kawasaki: Tetsu to Hagane, 1980, vol. 66, S193
[Thermo-Calc 2013] Thermo-Calc TCCS manuals Thermo-Calc software AB (Stockholm, SE), (2013).
[Thomas 2008] B.G. Thomas and M. Bellet: Modeling of stress, distortions and hot tearing, In ASM Handbook Volume 15: Casting, Division 4: Modeling and Analysis of Casting Processes, American Society of Metals, 2008, pp. 449-461
[Wang 2004] N. Wang, S. Mokadem, M. Rappaz and W. Kurz: Acta Mater., 2004, vol. 52, pp. 3173-3182
[Wintz 1994] M. Wintz, M. Bobadilla and M. Jolivet : La Revue de Métallurgie, 1994, vol. 4, pp. 105-114
[Won 2000] Y.M. Won, T.J. Yeo, D.J. Seol and K.H. Oh: *Metall. Mater. Trans. B, 2000, vol. 31, pp. 779-794*
[World Steel Association] https://www.worldsteel.org/
[Yamaguchi 2012] J. Yamaguchi, T. Nakashima and T. Sawai, “Change and Development of Continuous Casting Technology”, Nippon Steel Technical Report, 2012, No. 394, pp. 12-19.
[Yamanaka 1991] A. Yamanaka, K. Nakajima, K. Yasumoto, H. Kawashima and K. Nakai: *Proc. 5th Int. Conf. on Modeling of Casting, Welding and Advanced Solidification Processes, 1991, M. Rappaz, M.R. Ozgu and K.W. Mahin (eds.), TMS, pp. 279-284*

[Zaragoci 2012] J.F. Zaragoci, L. Silva, M. Bellet and C.A. Gandin : Proc. MCWASP XIII, 13th Int. Conf. on Modelling of Casting, Welding and Advanced Solidification Processes, Schladming (Austria), June 17-22, 2012, A. Ludwig, M. Wu, A. Kharicha (eds.), IOP Conference Series 33 (2012) 012054, 8 pages
[Zhang 2013] H. Zhang, K. Nakajima, C.A. Gandin and J. He: ISIJ Int., **53**(2013), 493.

Résumé

Ces travaux portent sur la déformation des aciers au cours de leur solidification, au moyen d'une expérience instrumentée et de sa simulation numérique. L'étude est focalisée sur deux phénomènes induits par la déformation : la fissuration à chaud et la macroségrégation. L'expérience consiste à poinçonner latéralement un lingot de 450 kg, alors que son cœur est encore partiellement liquide.

L'expérience est instrumentée thermiquement et mécaniquement. Les lingots sont analysés, visuellement en termes de lieu et de fréquence d'apparition de fissures, et par microsonde pour les ségrégations chimiques.

Pour la fissuration à chaud, une simulation numérique 3D par éléments finis est mise en œuvre avec le logiciel Thercast®, dans lequel a été implanté un critère d'amorçage de fissure basé sur la déformation plastique cumulée en fin de solidification, entre deux valeurs critiques de fraction de liquide. La comparaison entre simulations et observations montre le caractère prédictif du critère.

La simulation numérique de la macroségrégation est réalisée avec le logiciel R2sol qui résout simultanément la déformation du solide et l'écoulement du liquide. La simulation montre la redistribution des solutés dans le cœur du lingot sous l'effet de la compression du squelette solide et de l'écoulement du liquide, induits par le poinçonnement. Elle reproduit qualitativement les mesures expérimentales mais sous-estime l'amplitude des hétérogénéités de composition chimique. Une discussion des résultats permet de dégager des pistes permettant d'espérer une prédiction quantitative dans le futur.

Les deux thématiques étudiées ont mis en relief la nécessité d'une bonne modélisation des phénomènes de microségrégation des alliages multiconstitués. Un modèle a été spécifiquement développé à cet effet.

Mots-clés

Fissuration à chaud, macro et microségrégation, éléments finis, aciers, solidification, test de poinçonnement

Abstract

Experimental and numerical studies of hot tearing and macrosegregation formation during steel solidification are reported. On one hand, an ingot punching test is considered. It consists of the application of a deformation at the surface of a solidifying 450 kg steel ingot. On the other hand, finite element thermo-mechanical modelling of the test is used.

For hot tearing analysis, 3D finite element modeling is applied by use of Thercast® software. The time evolution of the strain tensor serves to evaluate the possibility for hot tear formation with a Hot Tearing Criterion (HTC). The HTC compares the local accumulation of strain over a certain solidification interval with the expression of a critical value proposed in the literature. Detailed comparisons reveal an excellent capability of the HTC to predict the formation of hot tears.

For macrosegregation analysis, a two-phase formulation has been implemented (R2sol software), in which the velocities of the liquid and solid phases are concurrently solved for. The simulation shows how solutes are redistributed through the central mushy zone of the ingot under the effect of the compression of the solid phase resulting from the punching of the solid shell. The simulation proves its capability to reproduce the main experimental trends. However the predicted intensity of macrosegregation is lower than measured. Through discussion and analysis of different numerical sensitivity tests, critical material parameters and model improvements are identified in view of achieving better quantitative predictions in the future.

The two topics studied have clearly shown the need for a good modelling of microsegregation phenomena in multicomponent alloys. A numerical model has especially been developed and implemented in the two software packages.

Keywords

Hot tearing, macro- and microsegregation, finite element method, steels, solidification, ingot punching test